INVESTIGATIONS ON THE DIRECT CONVERSION OF NUCLEAR FISSION ENERGY TO ELECTRICAL ENERGY IN A PLASMA DIODE
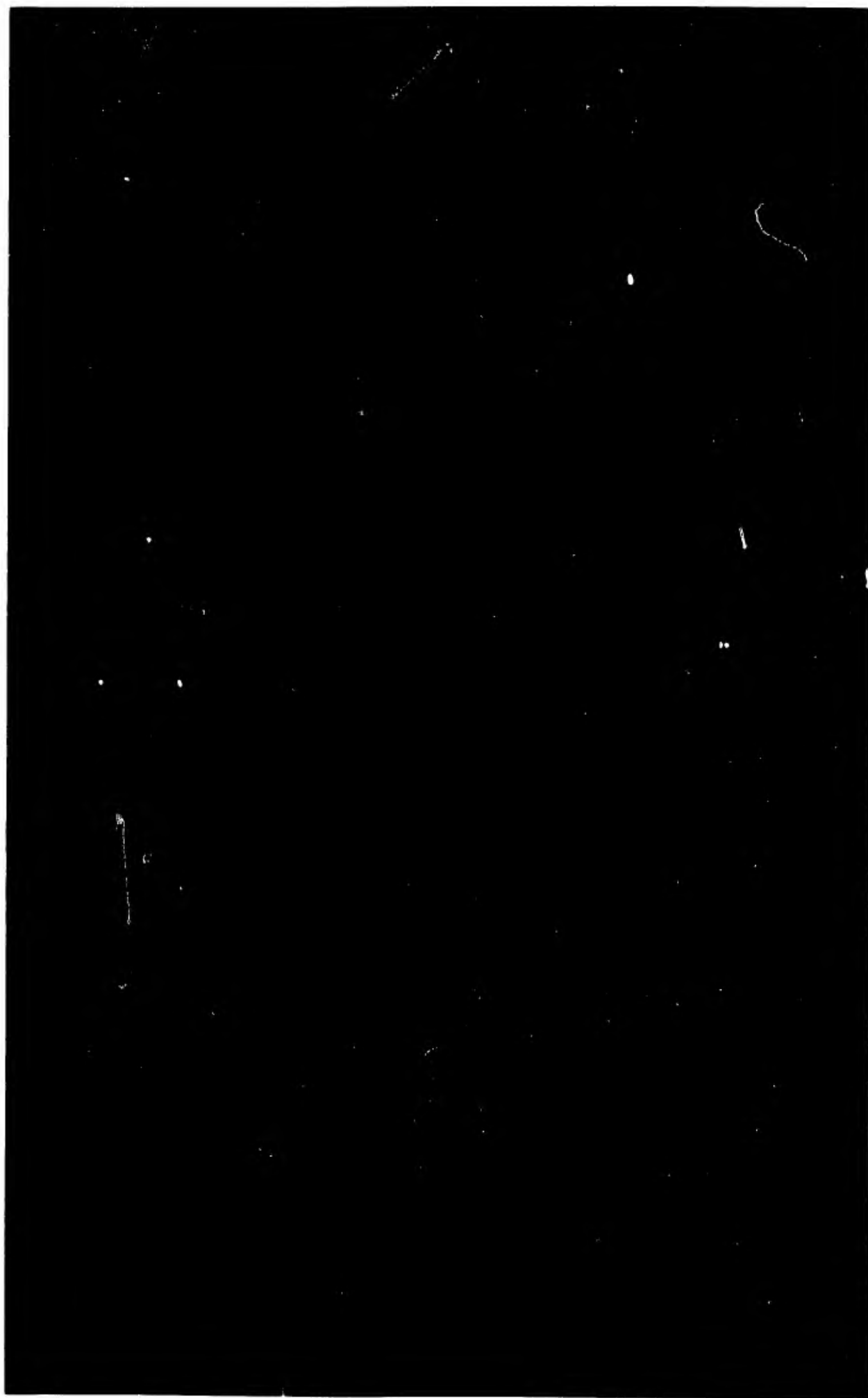
ANNUAL REPORT

for

Nonr-3109(00)

OCTOBER 31, 1964

RESEARCH LABORATORIES

GENERAL MOTORS CORPORATION

WARREN, MICHIGAN

CLEARINGHOUSE FOR FEDERAL SCIENTIFIC AND TECHNICAL INFORMATION CFSTI
DOCUMENT MANAGEMENT BRANCH 410.11

LIMITATIONS IN REPRODUCTION QUALITY

ACCESSION # *AD 609177*

☑ 1. LEGIBILITY OF THIS DOCUMENT IS IN PART UNSATISFACTORY.
REPRODUCTION HAS BEEN MADE FROM THE BEST AVAILABLE COPY.

☐ 2. ORIGINAL DOCUMENT CONTAINS COLOR OTHER THAN BLACK AND WHITE
AND IS AVAILABLE IN LIMITED SUPPLY. AFTER PRESENT STOCK IS EX-
HAUSTED, IT WILL BE AVAILABLE IN BLACK-AND-WHITE ONLY.

☐ 3. THE REPRODUCIBLE QUALITY OF THIS DOCUMENT IS NOT ADEQUATE
FOR PUBLIC SALE. AVAILABLE TO CUSTOMERS OF THE DEFENSE
DOCUMENTATION CENTER ONLY.

☐ 4. DOCUMENT AVAILABLE FROM CLEARINGHOUSE ON LOAN ONLY
(TECHNICAL TRANSLATIONS).

PROCESSOR:

TSL-107-12/64

V. Ritenour

OFFICE OF NAVAL RESEARCH

Contract Nonr-3109(00)

Investigations on the Direct Conversion of Nuclear
Fission Energy to Electrical Energy in a Plasma Diode

Report No. 5

Authors

C. B. Leffert
D. B. Rees
F. E. Jamerson

ABSTRACT

The ionization of pure, mixed and cesium-seeded noble gas systems by fission fragments has been investigated using ceramic-metal tubes operated in a high neutron flux region of a nuclear reactor. An analysis of the production and transport of ions and electrons in the tube has shown that when the charge loss in the plasma is predominantly by volume recombination of molecular ions and electrons, the tube current is proportional to $(voltage)^{1/2}$. Experimental current-voltage data in neon, argon, xenon and a neon-argon mixture with Ar/Ne of 10^{-3} for gas pressures of 240 and 400 torr and a neutron flux $\sim 10^{13}$ cm^{-2} sec^{-1} exhibited the dependence of current on $(voltage)^{1/2}$. Calculation of the magnitude of the current completely from theory, using a detailed model of ion generation rate, showed an agreement with the experimental data within $\pm 10\%$. For a gas pressure of 240 torr, where the ion generation rate was of order 5×10^{16} cm^{-3} sec^{-1}, the average ion density computed for the pure gases was $\sim 2.5 \times 10^{11}$ cm^{-3} but for the Ne-Ar mixture (where the loss rate of argon ions is reduced) the ion density was about four times higher, i.e. $\sim 1.0 \times 10^{12}$ cm^{-3}. Some preliminary studies of reaction kinetics in Ne-Ar mixtures, designed to maximize ion number density, have indicated that with the known ion generation rates at a neutron flux of 10^{13} cm^{-2} sec^{-1}, densities as high as $\sim 4 \times 10^{12}$ cm^{-3} may be obtained for a mixture with Ar/Ne of 10^{-4} at values of $p \sim 100$ torr. Lack of detailed knowledge of some of the relevant conversion processes in an argon-cesium mixture inhibits at present a similar study of reaction kinetics in this system. However, preliminary current-voltage data for Ar/Cs of 10^{-5} at an argon pressure of 240 torr, appears to follow a current-$(voltage)^{1/2}$ relationship and indicates that the ion generation rate is significantly higher than that for Ne-Ar or the pure gases under the same conditions.

TABLE OF CONTENTS

INVESTIGATIONS ON THE DIRECT CONVERSION OF
NUCLEAR FISSION ENERGY TO ELECTRICAL ENERGY IN A PLASMA DIODE

INTRODUCTION

A noble gas plasma generated by fission fragment ionization is being investigated for application in thermionic converters. The program has concentrated on an analysis of the fundamental processes taking place in the plasma generated by this method. This is necessary in order to arrive at the gas parameters that lead to optimum plasma conditions for maximizing electron transport in the diode.

In the previous reporting period,[1] data obtained from ionization tubes were presented for gas fillings of neon, argon, xenon and neon-argon, along with an analysis which described the I-V characteristics obtained. In that report the fit between theory and experiment was made by adjusting one parameter, viz., the average ion generation rate.

The present report describes an analytical method for computing the ion generation rate directly from the fission fragment energy loss. Combined with the ion transport theory developed earlier, this allows the calculation of the I-V characteristic to be made directly without any adjustable parameters. Values of the ion generation rate computed for pure neon and for neon-argon (Ar/Ne of 10^{-3}) are used in a detailed analysis of the reaction kinetics of the neon-argon system. This analysis leads to an evaluation of the electron number density in the neon-argon mixture for varying conditions of Ar/Ne and total pressure. Preliminary data on ion generation rate are also reported for an argon-cesium mixture with Cs/Ar of $\sim 3 \times 10^{-5}$. Finally, and incidental to the main program, a value is given for the secondary electron yield per fission fragment emitted from the uranium surface, since that quantity was readily determined from the present work.

The subsequent sections discuss the program Objectives, Conclusions and Future Plans.

OBJECTIVES

The objectives initially set for the current reporting period were as follows:

1. Experiments were to be continued on the inpile measurement of ion generation rate in noble gas mixtures.

2. Theoretical studies were also to be continued on the ion generation rate and the ion tube I-V characteristic.

3. Electron transport measurements in noble gas plasmas were to be initiated. A tube incorporating a nuclear heater thermionic emitter was to be developed for this study.

During this reporting period considerable time was spent on theoretical analyses. A major endeavor was the development of the ion generation rate and I-V characteristic analysis. Additionally, a reaction kinetics analysis was begun in order to evaluate electron number density from the ion generation rate data for noble gas mixtures. Consequently the progress on the electron transport experiment was limited to the evaluation of a particular diode design and some heat transfer mockup studies. This thermionic diode will be discussed in a future report.

CONCLUSIONS

1. The current-voltage characteristic for the ceramic-metal ionization tube can be calculated directly without the need for adjustable parameters. The agreement between the theoretical and experimental values of current for the pure gases is $\pm 10\%$.

2. The ion generation rate can be computed from the fission fragment energy loss using a linear energy loss model. The use of a quadratic energy loss model influences the resultant I-V characteristic only slightly when compared to that using the linear model. Computer time is reduced by using the linear model.

3. The ion generation rate can be computed accurately provided the value of w (ev/ion pair) is known for the gas. For example, the difference in the I-V characteristic (for $V \lesssim 25$ volts) between neon and a mixture of neon-argon (Ar/Ne of 10^{-3}) was accounted for correctly by the difference

in w for these two gas compositions.

4. Analysis of the I-V data for neon and neon-argon leads to values for the ion generation rates of atomic neon ions and metastable neon atoms.

5. The electron number density for the neon-argon mixture can be computed from the reaction kinetic equations which take account of the various processes of production and loss of ions. The number density is sensitive to gas pressure and the ratio of gas species. Densities greater than 10^{12} cm^{-3} were computed for typical conditions.

6. Using a modified ceramic-metal ion tube the ion generation rate in an argon-cesium mixture (Cs/Ar of 3×10^{-5}) was shown to be higher than for pure Ar and for Ne-Ar.

7. From a reevaluation of data taken with a vacuum diode operated inpile, the secondary electron yield from the uranium-nickel (5.7 wt.% Ni) alloy used in the ion generation rate studies is 207 ± 10 electrons per fission fragment emitted from the foil.

8. The ion generation rates and plasma densities at the midpoint of the ion tube (3 mm gap) for a gas pressure of 240 torr and a neutron flux of 1.0×10^{13} cm^{-2} sec^{-1} are given below.

Gas	Ion Generation Rate (cm^{-3} sec^{-1})	Recombination Loss Process	Ion Density (cm^{-3})
Neon	1.8×10^{16}		2.9×10^{11}
Argon	3.6×10^{16}	$\begin{cases} y^+ + 24 \longrightarrow y_2^+ + y \\ \\ y_2^+ + e^- \longrightarrow 2y \end{cases}$	2.3×10^{11}
Xenon	8.1×10^{16}		2.4×10^{11}
Neon-Argon (0.1% Ar)	2.6×10^{16}	$\begin{cases} Ne^+ \text{ as above} \\ Ar^+ + Ar + Ne \longrightarrow Ar_2^+ + Ne \\ Ar_2^+ + e \longrightarrow 2\,Ar \end{cases}$ 1.0×10^{12}	

The results for S are higher in this case than before[1] and are attributed to a more precise evaluation of the tube geometry in calculating the ion generation rate. The value of number density for neon-argon was computed from the reaction kinetics analysis.

FUTURE PLANS

1. Reaction kinetics studies will be extended to include an analysis of the argon-cesium plasma ion number density.

2. A microwave measurement of ion number density in fission fragment ionized mixed gas systems (Ne-Ar and Ar-Cs) will be made inpile. This experiment will be used to verify the reaction kinetics analysis.

3. A diode using a nuclear thermionic emitter with a mixed gas filling (near optimum conditions) will be operated inpile in order to determine the electron transport through a noble gas plasma.

4. Analysis of electron transport through noble gas plasmas related to the inpile electron transport measurement will be initiated.

REFERENCES

1. Investigations on the Direct Conversion of Nuclear Fission Energy to Electrical Energy in a Plasma Diode, 1963 Annual Report No. 4; C. B. Leffert, F. E. Jamerson, and D. B. Rees.

ACKNOWLEDGMENTS

SECTION A

BLANK PAGE

SECTION A

ION GENERATION RATE THEORY
AND ANALYSIS OF EXPERIMENTAL CURRENT-VOLTAGE DATA

ABSTRACT

The ion generation rate in a noble gas is computed from the energy loss of the fission fragments as they penetrate the gas adjacent to a fissioning uranium plate. A description of the digital computer program is given. The current-voltage characteristic for an ionization tube is then computed using the ion generation rate. A brief description of this computer program is also given. Finally, the inpile experimental current-voltage characteristics obtained on a metal-ceramic ionization tube are compared with the results of the computations. The I-V curves computed with no adjustable parameters agreed well ($\pm 10\%$) with the experimental curves and confirmed both the ion generation rate and ion transport models.

TABLE OF CONTENTS

I. INTRODUCTION

The fission fragment ionization of noble gases has been under study for some time at the General Motors Research Laboratories as a means to create a space charge neutralizing plasma in a thermionic energy converter. Current-voltage characteristics have been obtained on ionization tubes run in the University of Michigan nuclear reactor and from those data it was possible to deduce an average value of the ion generation rate in the fission fragment generated plasma.[1] It was realized early in these studies that it would be very helpful if the ion generation rate at a point in the gas could also be obtained completely from theory starting with the energy loss of the fission fragments and taking into account the actual geometry of the tube. As a first step towards this goal an analytic solution for the ion generation rate was obtained for the ideal case of infinite parallel plane geometry and the solution was discussed previously.[1]

This report describes the computation of the ion generation rate for the two dimensional (R,Z) geometry of the ionization tube and the digital computer code employed in the solution. In order to compare theory with experiment a second program was written to compute the current-voltage characteristic for the ionization tube. This second code employs a generalized treatment of the ion transport model[1] and takes as input the computed ion generation rate from the first code for a matrix of points in the interelectrode gap and then computes the sheath thickness and current for specified voltage points. The program details for the first versions of these codes are presented in another report[2] and only the modifications for the final version are described here.

Finally the fit of the theory to experiment is discussed for the pure noble gases and for the mixture of neon and argon.

II. ION GENERATION RATE FROM FISSION FRAGMENT ENERGY LOSS

The energy loss of fission fragments as they penetrate matter has been treated theoretically by Bethe and Ashkin.[3] The fission fragment loses energy rapidly by electronic collisions at the beginning of its track when its velocity and charge are greatest. As the fragment slows down it loses part of its charge through recombination with electrons and the energy deposition rate decreases. Nuclear collisions become significant near the end of the track; this increases the energy deposition rate but not necessarily the ionization rate.

Ionization of Gases

The ionization of gases by fission fragments has been measured[4,5] and these results have been analyzed in terms of an "ionization defect" Δ ,[6] i.e. $E_o = wI + \Delta$ where E_o is the initial fragment energy, I is the number of ion pairs formed by fragments stopped in the gas and w is the energy loss per ion pair for these high velocity fragments. The ionization defect, Δ , accounts for the non-ionizing energy lost in nuclear recoils and w has been found to be very nearly equal to the value $w_\alpha = E_\alpha / I_\alpha$ obtained for alpha particles of initial energy E_α in the same medium.[4] A similar quantity for the fission fragments is $\bar{w} = E_o / I$ and setting $w = w_\alpha$ we have $\bar{w}/w_\alpha = 1 + \Delta / I w_\alpha$. The fission fragments are divided into two median energy groups (light, $E_{o1} = 98$ Mev and heavy, $E_{o2} = 67$ Mev) and the average energy loss per ion pair $\bar{w}$ relative to w_α is $\bar{w}_1 = 1.06\, w_\alpha$ for the light fragment and $\bar{w}_2 = 1.11\, w_\alpha$ for the heavy fragment.[4]

The ionization rate along the fission fragment track, dI/dx, can be written in terms of the stopping power of the gas $(-dE/dx)$ as $(dI/dx)_j = (-dE/dx)_j \times (dI/dE)_j$ where the subscript j equals 1 and 2 for the light and heavy energy groups of fission fragments, respectively. In this study the quantity $\bar{w}$ is made independent of E over the entire energy range of the fragment, $(dI/dx)_j = (-dE/dx)_j / \bar{w}_j$, and so the ionization rate is expressed in terms of the stopping power and the energy loss per ion pair for α particles in the same gas.

Energy Loss Model for Fission Fragments

The energy of the fragment (E_j) as a function of distance x from birth has been approximated[7] by either a linear dependence on distance, $E_j = E_{oj}(1 - x/R_{ij})$, or a quadratic dependence on distance $E_j = E_{oj}(1 - x/R_{ij})^2$; here R_{ij} is the total range of the fragment j in the medium i. In terms of range units, $u_{ij} = x_i / R_{ij}$, the energy deposition per range unit for the linear model is

$$dE_j / du_{ij} = -E_{oj} \tag{1}$$

and is independent of the previous history of the particle, while the energy deposition per range unit for the quadratic model is

$$dE_j / du_{ij} = -2 E_{oj} \left(1 - \sum_i u_{ij} \right) \tag{2}$$

and depends upon the distance traveled in the fuel $(i=1)$ as well as in the gas

4

(i=2). For the conditions of interest here, that is for fuel thicknesses greater than one fission fragment range in the uranium and for gas film thicknesses considerably less than one fission fragment range in the gas, it is not expected that the final ion generation rate will be very sensitive to the particular energy loss model employed since at any one point in the gap the gas "sees" fragments from nearly all portions of the fission fragment energy spectrum.

Range of Fission Fragments

The fission fragment range is inversely proportional to the density $\rho(gm/cm^3)$ of the stopping medium.[7] For a wide range of materials, the stopping power was found to be proportional to the square root of the average atomic mass A of the stopping medium[8] to give the following relationship[9] for the unknown range R in terms of the known range R_a in air: $R=R_a(\rho_a/\rho)(A/A_a)^{1/2}$cm. For a gas at temperature $T(°K)$ and pressure $p(torr)$, this reduces to $R=20.1 R_a(\sqrt{A}/M)(T/p)$cm, where M is the molecular weight of the gas.
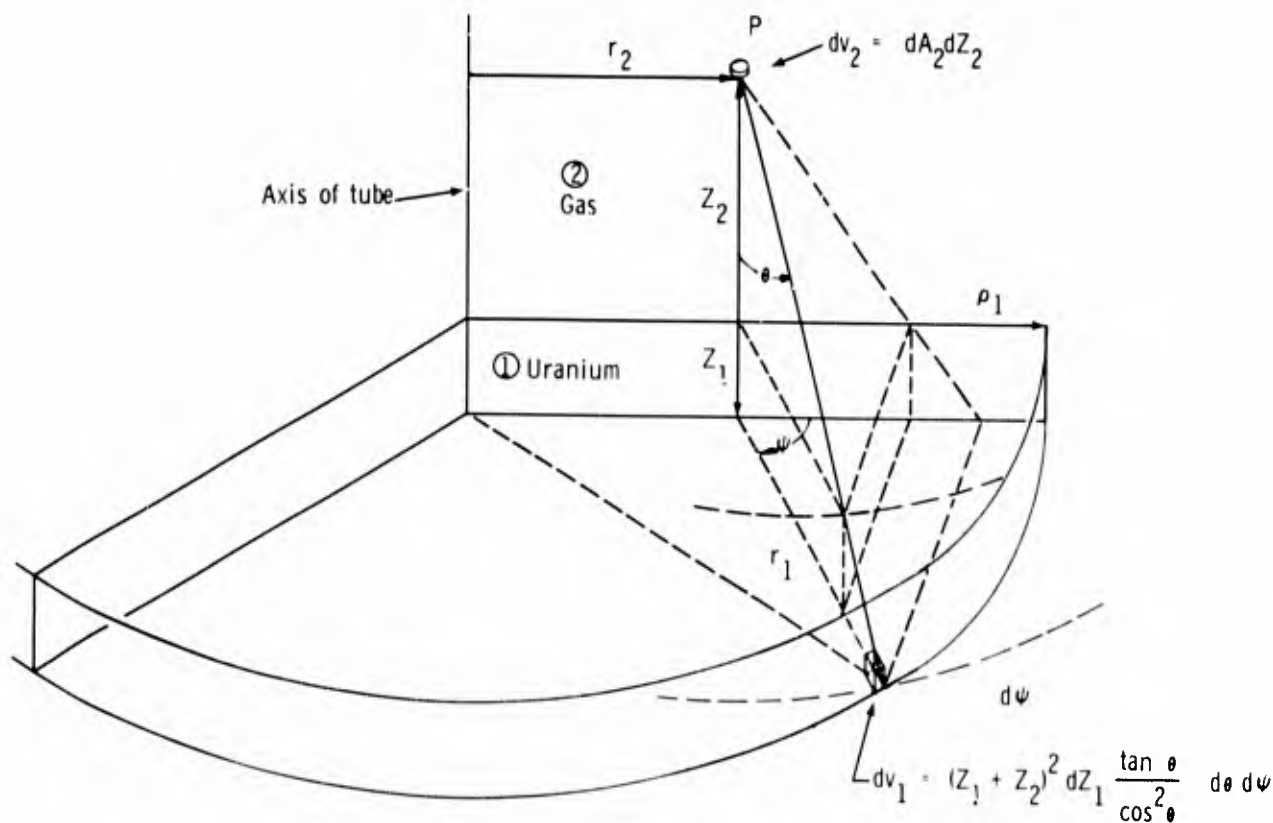
Derivation of Ion Generation Rate Equation

Fig. 1. Geometry for derivation of ion generation equation.

The ion generation rate $S(r_2,z_2)$ at point P in the gas (see Fig. 1) from both fission fragments is obtained from the energy deposition rate $\dot{\varepsilon}_j$ ($eV,cm^{-3}sec^{-1}$ at P and $\bar{w}_j$, the energy to create an ion pair in the gas

$$S(r_2,z_2) = \sum_{j=1}^{2} \dot{\varepsilon}_j / \bar{w}_j \ . \tag{3}$$

Consider the differential energy deposition rate $d\dot{\varepsilon}_j(r_2,z_2)$ at P resulting from those fragments of group j that originate in the volume element dv_1 with coordinates r_1, Ψ, Θ in the uranium. The fission rate in dv_1 is $(Q_f \phi dv_1)$ where Q_f is the fission cross section (cm^{-1}) and ϕ is the thermal neutron flux $(cm^{-2}sec^{-1})$, and the total kinetic energy released in dv_1 to fragments of group j is $(Q_f \phi E_{oj} dv_1)$ where E_{oj} is the initial fragment energy. Assuming isotropic emission of the fragments within the uranium and straight line flight over the entire range, the fraction of fragments that would penetrate dv_2 at P with no absorption is $dA_2 cos^3\Theta/4\pi(z_1+z_2)^2$. The energy deposition per cm of path at P for each fragment from dv_1 is given by Eqs. (1) or (2), depending upon the energy loss model, and the fraction of the initial kinetic energy deposited in dv_2 is $(dE_j/du_{2j})(dz_2/R_{2j}E_{oj}cos\Theta)$.

Combining these factors, the differential ion generation rate at P due to the fission fragments of group j from the volume element dv_1 in the fuel is

$$dS_j(z_1,z_2,\Theta) = \left(\frac{Q_f \phi}{4\pi}\right)\left(\frac{E_{oj} R_{1j}}{\bar{w}_j R_{2j}}\right) du_{1j} d\psi \, F_j(\Theta,u_{1j},u_{2j})d\Theta \tag{4}$$

where for the linear energy loss model

$$F_j(\Theta,u_{1j},u_{2j}) = tan \, \Theta \tag{5}$$

and for the quadratic energy loss model

$$F_j(\Theta,u_{1j},u_{2j}) = 2\left(1 - \frac{u_{1j}+u_{2j}}{cos\Theta}\right)tan \, \Theta \ . \tag{6}$$

For an infinite slab of uranium of thickness $t \geq R_{11}$ the integrations over the coordinates z, Ψ and Θ are readily performed analytically to give solutions to Eq. (4):

Linear Energy Loss[1]

$$S(z_2) = \sum_{j=1}^{2} \left(\frac{Q_f \phi E_{oj} R_{1j}}{\overline{W}_j R_{2j}} \right) \left[\frac{1}{2} \left(1 - u_{2j} + u_{2j} \ln u_{2j} \right) \right] ; \qquad (7)$$

Quadratic Energy Loss

$$S(z_2) = \sum_{j=1}^{2} \left(\frac{Q_f \phi E_{oj} R_{1j}}{\overline{W}_j R_{2j}} \right) \left[\frac{1}{2} \left(1 - u_{2j}^2 + 2 u_{2j} \ln u_{2j} \right) \right]. \qquad (8)$$

A comparison of the two energy loss models for this ideal geometry is given in Fig. 2. Since the constant is the same in Eqs. (7) and (8) only the factors in brackets (=f in Fig.2) are plotted as well as their ratio for a gas pressure of 240 torr. Various dimensions in the tube are shown on the abscissa for various gases. If an average dimension is the interelectrode spacing, d, there is less than 20% difference in ion generation rate predicted between the two models.

For a point P in the gas off-axis and above a finite uranium disc $(\rho_1 < R_{11})$, the integrations over the coordinates z, ψ and θ become quite complex. The complexity arises from the geometry and finite range of the fission fragments and appears in the limits of integration. The solution to Eq.(4) takes the form

$$S(r_2, z_2) = \left(\frac{Q_f \phi}{4\pi} \right) \sum_{j=1}^{2} \left(\frac{E_{oj} R_{1j}}{W_j R_{2j}} \right) \sum_{k=1}^{4} 2 \int_{u_{ijk}^{min}}^{u_{ijk}^{max}} du_{ij} \int_{\psi_{jk}^{min}}^{\psi_{jk}^{max}} d\psi \int_{\theta_{jk}^{min}}^{\theta_{jk}^{max}} F_j(\theta, u_{ij}, u_{2j}) d\theta \qquad (9)$$

where some of the limits of integration change depending on whether $0 \le r_2 \le \rho_1$ or $\rho_1 \le r_2 \le \rho_2$. $F_j(\theta, u_{ij}, u_{2j})$ is defined by Eqs.(5) or (6) depending upon the energy loss model. The subscript k designates a range of integration over the variables u_{ij} and ψ and this is discussed in the next section. The expression to be used for the above limits of integration for each value of k are listed in Table 1.

TABLE 1

Expressions for Limits of Integration of Eq.(9)

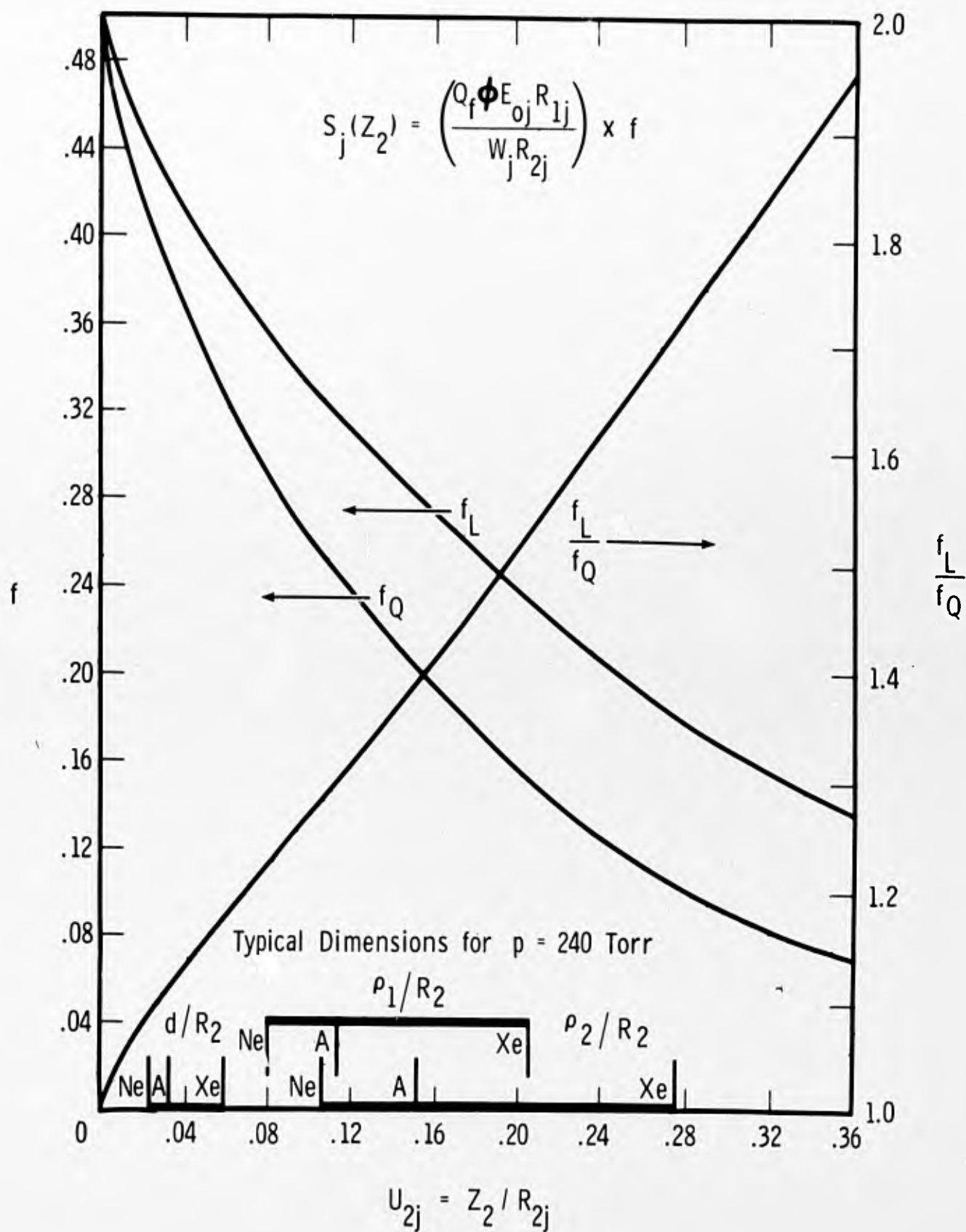| Limit	k = 1 Value	Eq.	k = 2 Value	Eq.	k = 3 Value	Eq.	k = 4 Value	Eq.
Case for $0 \leq r_2 \leq \rho_1$								
$u_{1jk}^{min} =$	0		u_{1j}^{m1}	(12)	u_{1j}^{m1}	(12)	u_{1j}^{m2}	(14)
$u_{1jk}^{max} =$	u_{1j}^{m1}	(12)	u_{1j}^{m2}	(14)	u_{1j}^{m2}	(14)	u_{1j}^{m3}	(15)
$\psi_{jk}^{min} =$	0		0		ψ_j^{max}	(13)	0	
$\psi_{jk}^{max} =$	π		ψ_j^{max}	(13)	π		π	
$\theta_{jk}^{min} =$	0		0		0		0	
$\theta_{jk}^{max} =$	$\theta_{\rho_1}^{max}$	(11)	$\theta_{\rho_1}^{max}$	(11)	θ_j^{max}	(10)	θ_j^{max}	(10)
Case for $\rho_1 < r_2 \leq \rho_2$								
$u_{1jk}^{min} =$	0		u_{1j}^{m1}	(12)	u_{1j}^{m1}	(12)	u_{1j}^{m4}	(18)
$u_{1jk}^{max} =$	u_{1j}^{m1}	(12)	u_{1j}^{m4}	(18)	u_{1j}^{m4}	(18)	u_{1j}^{m2}	(14)
$\psi_{jk}^{min} =$	ψ_j^{min}	(17)	ψ_j^{min}	(17)	ψ_j^{max}	(13)	ψ_j^{min}	(17)
$\psi_{jk}^{max} =$	π		ψ_j^{max}	(13)	π		π	
$\theta_{jk}^{min} =$	$\theta_{\rho_1}^{min}$	(16)	$\theta_{\rho_1}^{min}$	(16)	$\theta_{\rho_1}^{min}$	(16)	$\theta_{\rho_1}^{min}$	(16)
$\theta_{jk}^{max} =$	$\theta_{\rho_1}^{max}$	(11)	$\theta_{\rho_1}^{max}$	(11)	θ_j^{max}	(10)	θ_j^{max}	(10)

Fig. 2. Ion source rate for infinite plane geometry.

Limits of Integration

The detailed derivation of the limits of integration will not be given here but only an outline of the derivation together with the final expressions. The limits of integration are fixed by the finite range of the fission fragments. This range together with the geometry defines the volume of integration in the uranium that can contribute to the ionization at P. (Fig. 1) For a given value of z_1 and ψ the integration over Θ is performed first followed by the integration over ψ and finally by the integration over z_1. Because of symmetry the upper limit on ψ is taken as π and the result is multiplied by 2.

It is helpful to consider first the upper limit on Θ which prevails when Θ is not limited by the finite size of the uranium disc. For any particular point in the gas a distance z_2 above the uranium, fission fragments passing through this point could originate from a depth z_1 in the uranium out to an angle Θ_j^{max} given by

$$\Theta_j^{max} = \cos^{-1}\left(\frac{z_1}{R_{1j}} + \frac{z_2}{R_{2j}}\right). \tag{10}$$

Equation (10) describes a circle on a plane at depth z_1 in this uranium of large extent and many of the limits of integration are defined by the interaction of this circle and the edge of the actual uranium disc.
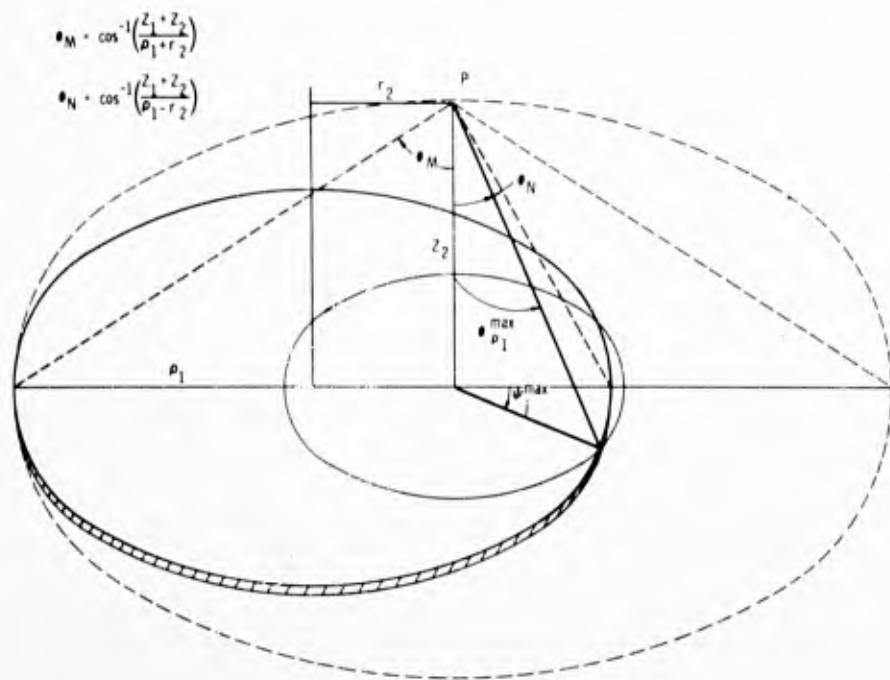
Case for $\Theta \leq r_2 \leq \rho_1$

Fig. 3. Geometry for limits of integration; case for $0 \leq r_2 \leq \rho_1$.

Referring to Fig. 3, consider the point P in the gas a distance r_2 from the axis of the tube but still over the uranium disc, i.e. $r_2 < \rho_1$, and at a height z_2 above the uranium where $z_2 < R_{2j}$. For the first region of the uranium $0 \leq u_1 \leq u_{1j}^{m1}$ near the surface (k=1 in Eq.(9)), $\theta_j^{max} > \theta_M$ in Fig. 3 and the upper limit on θ is fixed by the edge of the uranium disc and is given by $\theta_{\rho_1}^{max}$ (see Fig. 3) where

$$\theta_{\rho_1}^{max} = \cos^{-1}\left\{\frac{(z_1+z_2)}{\left[(z_1+z_2)^2 + (-r_2\cos\psi + (r_2^2\cos^2\psi - (r_2^2-\rho_1^2))^{1/2})^2\right]^{1/2}}\right\}. \quad (11)$$

The range of integration on ψ is $0 \leq \psi \leq \pi$ and the limit u_{1j}^{m1} is fixed by the condition that $\theta_j^{max} = \theta_M$ which yields

$$u_{1j}^{m1} \simeq u_{2j}\left\{\frac{1}{\left[u_{2j}^2 + \left(\frac{\rho_1}{R_{2j}} + \frac{r_2}{R_{2j}}\right)^2\right]^{1/2}} - 1\right\}. \quad (12)$$

For the second region of the uranium ($u_{1j}^{m1} < u_{1j} \leq u_{1j}^{m2}$) the circle described by Eq. (10) intersects the uranium disc and two regions of integration over ψ must be considered. For the first ψ region (k=2 in Eq.(9)), i.e. $0 \leq \psi \leq \psi_j^{max}$, the range of integration for θ is $0 \leq \theta \leq \theta_{\rho_1}^{max}$ while for the second ψ region (k=3 in Eq.(9)), i.e. $\psi_j^{max} < \psi \leq \pi$, the range of integration for θ is $0 \leq \theta \leq \theta_j^{max}$. To obtain ψ_j^{max}, $\theta_{\rho_1}^{max}$ (Eq. (11)) is set equal to θ_j^{max} (Eq.(10)) and solved for ψ to give

$$\psi_j^{max} = \cos^{-1}\left\{\frac{\rho_1^2 - r_2^2 - (z_1+z_2)^2\left[(u_{1j}+u_{2j})^{-2} - 1\right]}{2\,r_2(z_1+z_2)\left[(u_{1j}+u_{2j})^{-2} - 1\right]^{1/2}}\right\}. \quad (13)$$

The upper limit on u_{1j} for this range is found by setting $\theta_j^{max} = \theta_N$ in Fig. 3 which yields

$$u_{1j}^{m2} \simeq u_{2j}\left\{\frac{1}{\left[u_{2j}^2 + \left(\frac{\rho_1}{R_{2j}} - \frac{r_2}{R_{2j}}\right)^2\right]^{1/2}} - 1\right\}. \quad (14)$$

11

For the third region of the uranium $(u_{1j}^{m2} < u_{1j} \leq u_{1j}^{m3})$, $k=4$ in Eq.(9) and the circle defined by Eq.(10) lies within the uranium disc. For this region the range of integration on θ is $0 \leq \theta \leq \theta_j^{max}$ and the range of integration on ψ is $0 \leq \psi \leq \pi$. The upper limit u_{1j}^{m3} is the difference between 1 range and the distance to P in range units, i.e.

$$u_{1j}^{m3} = 1 - u_{2j}.\tag{15}$$

Case for $\rho_1 < r_2 \leq \rho_2$
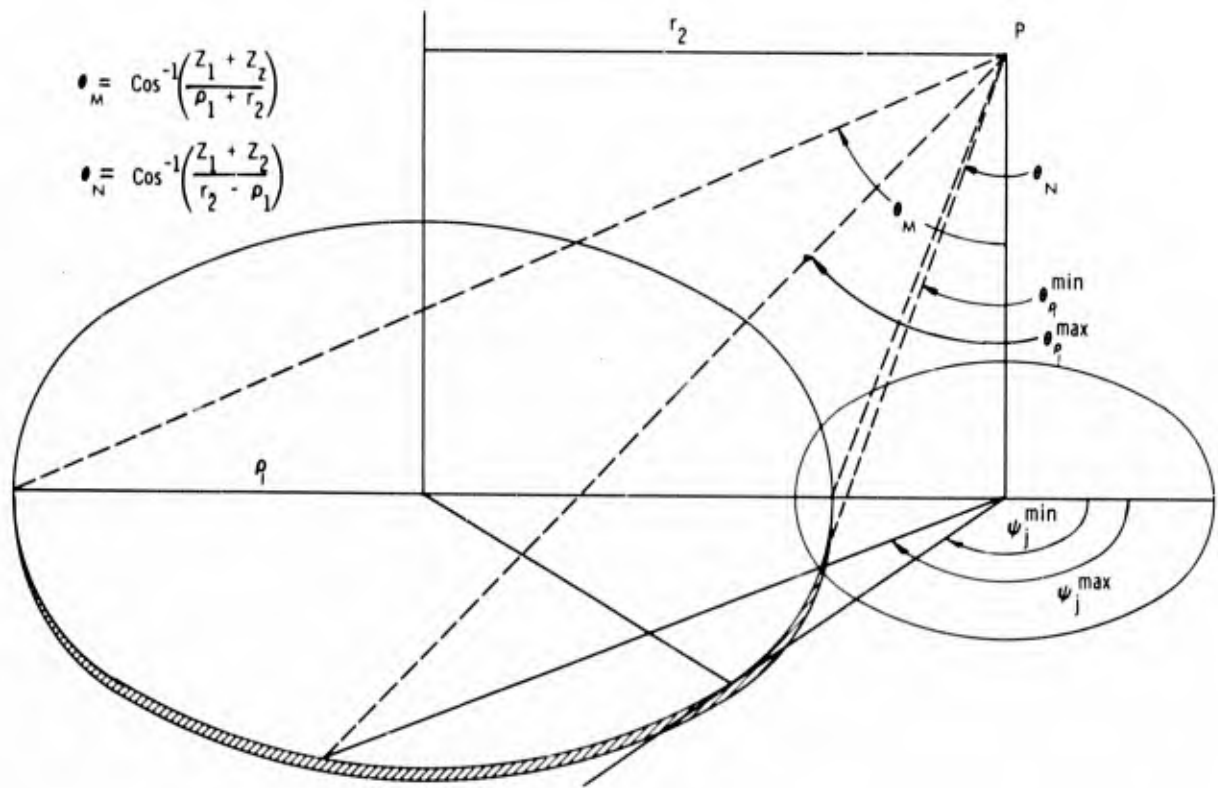
Fig. 4. Geometry for limits of integration; case for $\rho_1 < r_2 \leq \rho_2$.

Referring to Fig. 4 for $r_2 > \rho_1$ it is seen that the lower limits for θ and ψ are greater than zero. For the first region of the uranium $0 \leq u_{1j} \leq u_{1j}^{m1}$, when $\theta_j^{max} > \theta_m$ and $k=1$ in Eq.(9), the range of integration on θ is $\theta_{\rho1}^{min} \leq \theta \leq \theta_{\rho1}^{max}$. Equation (11) still defines $\theta_{\rho1}^{max}$ at the far side of the uranium disc for angle ψ and $\theta_{\rho1}^{min}$ is set by the near side of the uranium disc for angle ψ, i.e.

$$\theta_{\rho1}^{min} = \cos^{-1}\left\{ \frac{(z_1 + z_2)}{[(z_1+z_2)^2 + (-r_2\cos\psi - (r_2^2\cos^2\psi - (r_2^2 - \rho_1^2))^{1/2})^2]^{1/2}} \right\}.\tag{16}$$

12

The range of integration on ψ is $\psi_j^{min} \leq \psi \leq \pi$ where ψ_j^{min} is fixed by the tangent to the edge of the disc from the projected point P, i.e.

$$\psi_j^{min} = \pi - \cos^{-1}\left[1 - (\rho_1/r_2)^2\right]^{1/2}. \tag{17}$$

The upper limit u_{1j}^{m1} is given by Eq. (12).

The second region of the uranium, $u_{1j}^{m1} < u_{1j} \leq u_{1j}^{m4}$, is now bounded by a different upper limit. Again the circle described by Eq. (10) intersects the disc and gives two regions of integration over ψ. For the first ψ region (k=2 in Eq. (9)), i.e. $\psi_j^{min} \leq \psi \leq \psi_j^{max}$, the range of integration for θ is $\theta_{\rho 1}^{min} \leq \theta \leq \theta_{\rho 1}^{max}$ where $\theta_{\rho 1}^{min}$ and $\theta_{\rho 1}^{max}$ are given by Eqs. (16) and (11), respectively. For the second ψ region (k=3 in Eq. (9)), i.e. $\psi_j^{max} < \psi \leq \pi$, the range of integration for θ is $\theta_{\rho 1}^{min} \leq \theta \leq \theta_j^{max}$ where θ_j^{max} is given by Eq. (10). The limits ψ_j^{min} and ψ_j^{max} are given by Eqs. (16) and (13), respectively. The limit u_{1j}^{m1} is given by Eq. (12). The limit u_{1j}^{m4} is obtained by setting $\theta_j^{max} = \theta_{\rho 1}^{max}$ for $\psi = \psi_j^{min}$ and solving for u_{1j} to give

$$u_{1j}^{m4} \simeq u_{2j}\left\{ \frac{1}{\left[u_{2j}^2 + \left(\frac{r_2}{R_{2j}}\right)^2 - \left(\frac{\rho_1}{R_{2j}}\right)^2\right]^{1/2}} - 1 \right\}. \tag{18}$$

For the third region of the uranium (k=4 in Eq. (9)), $u_{1j}^{m4} < u_{1j} \leq u_{1j}^{m2}$, the range of integration on ψ is $\psi_j^{min} \leq \psi \leq \pi$ and the range of integration on θ is $\theta_{\rho 1}^{min} \leq \theta \leq \theta_j^{max}$ where all of these limits have been defined previously. A summary of the limits of integration for Eq. (9) is given in Table 1.

Computer Programs and Solutions for $S(r_2, z_2)$

The solution of Eq. (9) for $S(r_2, z_2)$ requires numerical techniques. Two programs were written for solution on the IBM 7094 computer. The first program for the linear energy loss model is described in detail in another report.[2] The second was a more general program and was used for the quadratic energy loss model. Both versions are described briefly together with some representative output.

All numerical integrations were performed by Simpson's rule, using a fixed number of steps (input) for each variable. Since the limits of integration were variable, the increment size changed from integration to

integration. One subroutine was written which performed integrations for both analytic and tabular functions having been given the name of a one argument Fortran function as part of its argument list. When the function was tabular, two different Fortran functions could be used. The first function was used when the range (and thus, the increment) for the integration was known in advance. The second function used an interpolation routine and the vectors for the independent variable X and dependent variable F(X) were specified in the control array. A call to the function with argument A caused the inter-polation routine to interpolate the argument A into the sequence X and return the interpolated value F(A).

Linear Energy Loss Model For the linear energy loss model, $F_j = \tan \theta$ (see Eq. (5)), and Eq. (9) can be simplified by some analytical integrations. Equation (9) can be written as

$$S(r_2, z_2) = K_1 \sum_{j=1}^{2} K_{2j} \, f_{2j} \, (r_2, z_2, R_{1j}, R_{2j}, \rho_1) \tag{19}$$

where $K_1 = (Q_f \phi / 4\pi)$, $K_{2j} = E_{oj} R_{1j} / \bar{w}_j R_{2j}$ and

$$f_{2j}(r_2, z_2, R_{1j}, R_{2j}, \rho_1) = \sum_{k=1}^{4} 2 \int_{u_{1jk}^{min}}^{u_{1jk}^{max}} du_{1j} \int_{\psi_{jk}^{min}}^{\psi_{jk}^{max}} d\psi \int_{\theta_{jk}^{min}}^{\theta_{jk}^{max}} F_j(\theta, u_{1j}, u_{2j}) d\theta . \tag{20}$$

The quantities on the right hand side of Eq. (20) have already been defined.

After some analytical integrations Eq. (20) reduced to the following expressions for f_{2j}:

For case $0 \le r_2 \le \rho_1$

$$f_{2j}(r_2, z_2, R_{1j}, R_{2j}, \rho_1) = -\frac{2}{R_{1j}} \int_{z_1=0}^{R_{1j} u_{1j}^{m1}} dz_1 \int_{\psi=0}^{\pi} \ln B(z_1, z_2, r_2, \psi) d\psi$$

$$+ \frac{2}{R_{1j}} \int_{z_1 = R_{1j} u_{1j}^{m1}}^{R_{1j} u_{1j}^{m2}} \left[\psi_j^{max} \ln(u_{1j} + u_{2j}) - \int_{\psi=0}^{\psi_j^{max}} \ln B(z_1, z_2, r_2, \psi) d\psi \right] dz_1$$

$$+ 2\pi \left[1 - (u_{2j} + u_{1j}^{m1})(1 - \ln(u_{2j} + u_{1j}^{m1})) \right] \tag{21}$$

where $B(z_1, z_2, r_2, \psi) = \cos \Theta_{\rho_1}^{max}$ and $\tag{22}$

for case $\rho_1 \le r_2 \le \rho_2$

$$f_{2j}(r_2, z_2, R_{1j}, R_{2j}, \rho_1) = \frac{2}{R_{1j}} \int_{z_1=0}^{R_{1j} u_{1j}^{m1}} dz_1 \int_{\psi = \psi_j^{min}}^{\pi} \ln C(z_1, z_2, r_2, \psi) d\psi$$

$$+ \frac{2}{R_{1j}} \int_{z_1 = R_{1j} u_{1j}^{m1}}^{R_{1j} u_{1j}^{m4}} \left[\int_{\psi = \psi_j^{min}}^{\psi_j^{max}} \ln C(z_1, z_2, r_2, \psi) d\psi + \int_{\psi = \psi_j^{max}}^{\pi} \ln \left(\frac{A(z_1, z_2, r_2, \psi)}{u_{1j} + u_{2j}} \right) d\psi \right] dz_1$$

$$+ \frac{2}{R_{1j}} \int_{z_1 = R_{1j} u_{1j}^{m4}}^{R_{1j} u_{1j}^{m2}} dz_1 \int_{\psi = \psi_j^{min}}^{\pi} \ln \left(\frac{A(z_1, z_2, r_2, \psi)}{u_{1j} + u_{2j}} \right) d\psi \tag{23}$$

where $A(z_1, z_2, r_2, \psi) = \cos \Theta_{\rho_1}^{min}$ and $\tag{24}$

15

$$C(z_1, z_2, r_2, \psi) = \left[\frac{(z_1 + z_2)^2 + \left[-r_2 \cos\psi + (r_2^2 \cos^2\psi - (r_2^2 - \rho_1^2))^{1/2} \right]^2}{(z_1 + z_2)^2 + \left[-r_2 \cos\psi - (r_2^2 \cos^2\psi - (r_2^2 - \rho_1^2))^{1/2} \right]^2} \right]^{1/2} . \tag{25}$$

These equations were solved numerically with the Fortran code and the input, output and flow diagrams are discussed elsewhere.[2]

Examples of the output of this code are shown in Figs. 5 and 6. A linear plot of the variation of S with the distance z_2 from the uranium plate is shown in Fig. 5 at various distances r_2 from the center of the uranium disc. Typical values of the tube parameters were used, i.e. xenon gas at 240 torr pressure and $\phi = 1.29 \times 10^{13} \text{cm}^{-2} \text{sec}^{-1}$. Solutions out to one full range of the fission fragment in the gas are shown in the log-log plot in Fig. 6. In both figures the code solutions are the solid curves and the points were obtained from analytic expressions presented earlier in Section C of reference (1). The analytic solution along the axis of the tube indicated by full circles was used to verify the accuracy of the code solution. The analytic solution for the edge of the uranium disc ($r_2 = \rho_1 = .952$) involved an approximation[1] and the agreement with the code is considered satisfactory.

The variation of the ion generation rate for the experimental tube geometry (described later) is shown in Fig. 7 for the case of neon gas at a pressure of 240 torr and a neutron flux of $1.0 \times 10^{13} \text{cm}^{-2} \text{sec}^{-1}$. Here $S(r_2, z_2)$ is plotted versus r_2 for three values of z_2, i.e. $z_2 = 0$, $d/2$ and d. This plot shows that near the electrode surface ($z_2 = 0$) but past the edge of the uranium disc ($r_2 > \rho_1$), the ion generation rate drops very rapidly because fission fragments emitted at $\theta = \pi/2$ are absorbed. The ion generation rate along the opposite electrode is reduced because of absorption of the fission fragments in the gas but S is somewhat more uniform since the fragments can now reach to the outer edges of the tube. Values for the constants used in these computations are listed in Table 2 in Section IV.
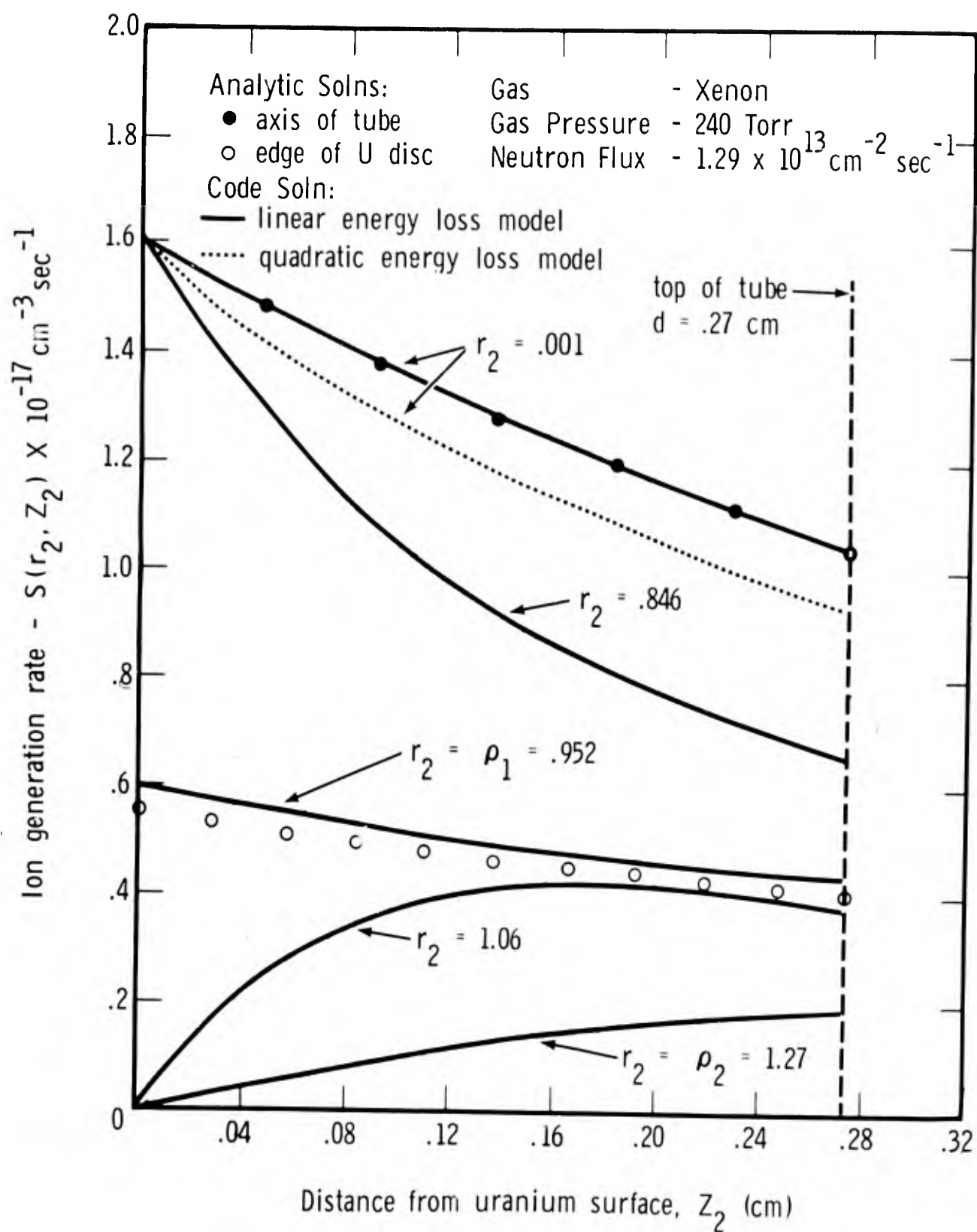
Fig. 5. Spatial variation of ion generation rate for typical tube parameters: linear plot.
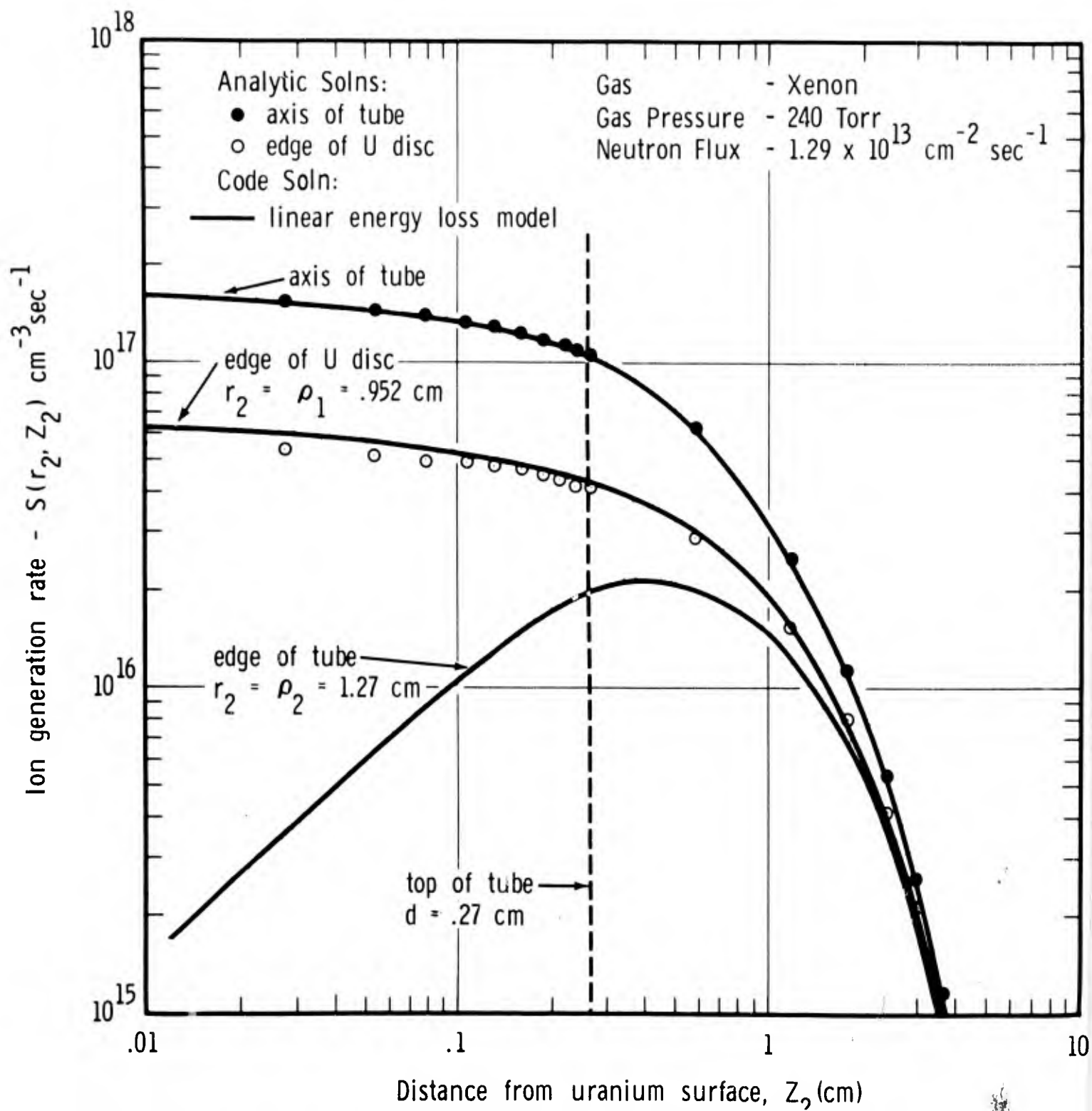
Fig. 6. Spatial variation of ion generation rate for typical
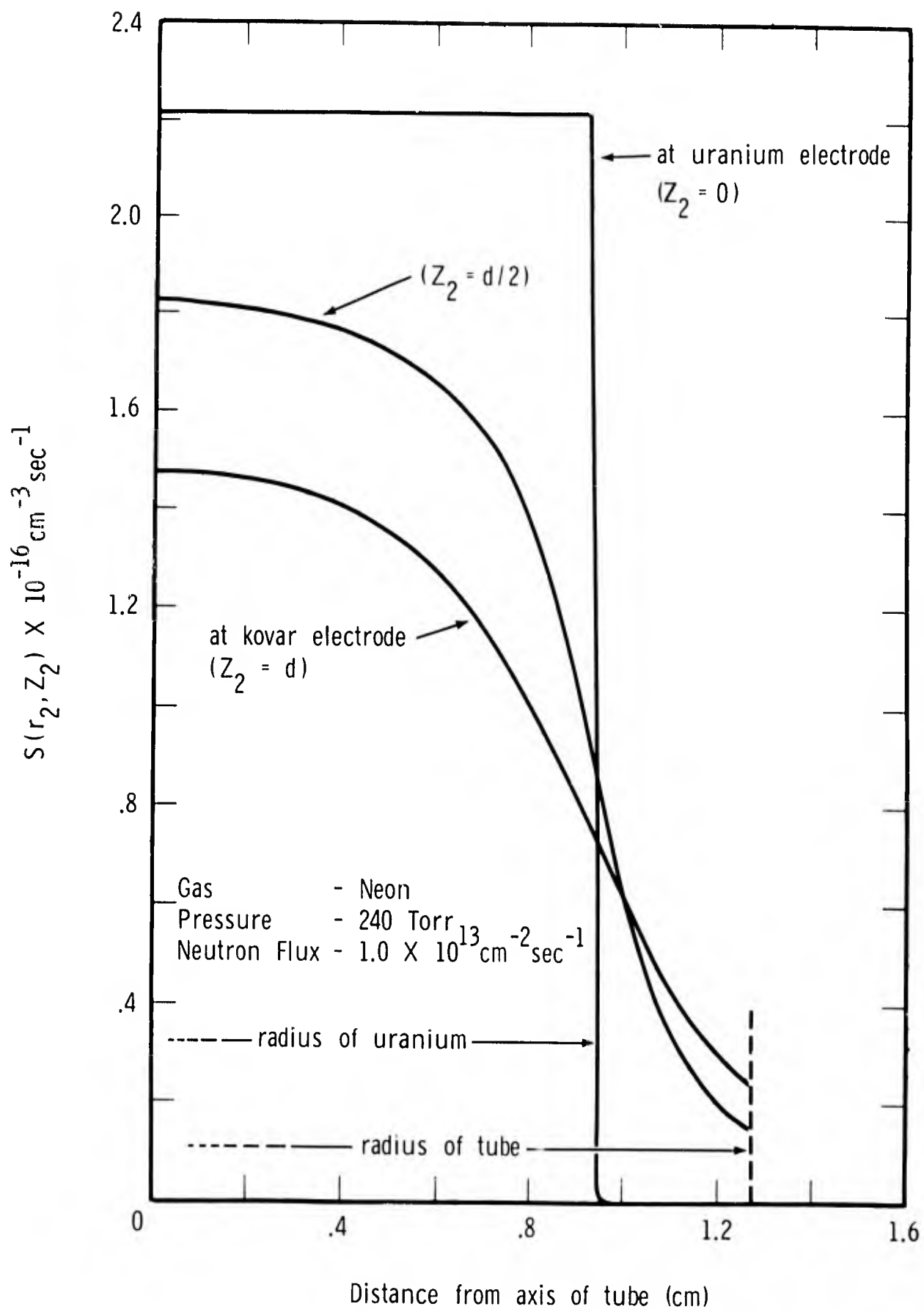tube parameters: log-log plot.

Fig. 7. Variation of ion generation rate for experimental tube geometry.

19

<u>Generalized Energy Loss Model</u>   The solution of Eq. (9) using Eq. (6) for the quadratic energy loss model required a triple integration using numerical techniques. A new program for the function $S(r_2, z_2)$ was coded as a subroutine and substituted into the main control program for the linear energy loss subroutine for $S(r_2, z_2)$. The new subroutine for $S(r_2, z_2)$ was written for a generalized energy loss model by making $F_j(\theta, u_{1j}, u_{2j})$ a Fortran II function statement.

A solution for $S(r_2, z_2)$ using this code and the quadratic energy loss model from Eq. (6) is shown in Fig. 5 as the dashed curve for S along the axis of the tube. The ion generation rate is seen to be the same at the uranium surface (see Eqs. (7) and (8) in limit $u_{2j}=0$) and down only about 10% at the far electrode $(z_2=d)$. As a check on the accuracy of the triple integration subroutine, Eq. (5) was substituted for the Fortran function statement $F_j(\theta, u_{1j}, u_{2j})$ and a curve was obtained identical to the solid curve labeled $r_2=.001$ for the first linear energy loss model code.

Some trouble was experienced with the numerical solution of the integral in Eq. (9) for positions in the gas very close to the uranium surface $(z_2 \longrightarrow 0)$. This condition involves the integration of the function $\tan \theta$ over the angle θ to an upper limit approaching $\pi/2$ where $\tan \theta \longrightarrow \infty$. The Simpson's rule formulation is a poor approximation for this condition and the problem was partially circumvented by introducing a cut-off to the upper limit of θ. This problem did not arise in the single integral solution for the linear energy loss model because the integration over θ was done analytically.

It will be shown later in Section III that the experimental verification of these computations of the ion generation rate involves the measurement of an ion current drawn from either of two sheaths separating the plasma from the two bounding metal electrodes. When the sheath is at the electrode opposite the uranium this problem of the numerical integration over $\tan \theta$ does not occur and verification of the theory can be obtained. The running time on the computer was much greater for the triple integral solution than for the single integral solution for the linear energy loss model and since the difference in answers was less than 10% no further effort was made to correct the triple integral solution for $z_2 \longrightarrow 0$.

III. ION TRANSPORT CURRENT-VOLTAGE CHARACTERISTIC

In the previous section it was shown that the ion generation rate in a gas film adjacent to a fissioning uranium plate could be computed from known parameters such as the range of the fission fragments and the energy to create one ion pair in the gas. It was of interest to verify this theory with an experimental measurement. The usual practice to measure ion production in typical ionization tubes is to apply a strong electric field between two electrodes and collect the ions on one plate and the electrons on the other as rapidly as they are made. The plasmas of interest in these studies are much too dense to bring about such complete charge separation so it was necessary to develop a theory for ion transport in the sheath bounding a dense plasma.

Ion Transport Model for Uniform Ion Generation Rate

The ion transport model for the case of a uniform ion generation rate $(\bar{S})$ in the interelectrode volume has been described previously.[1]
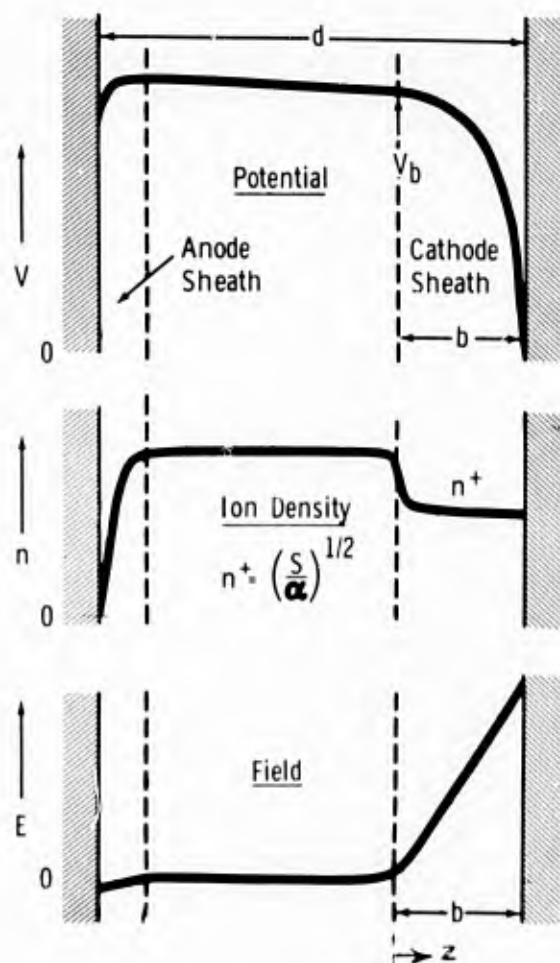

Fig. 8. Potential, ion density and field distribution for the plasma model.

Briefly, the predominant ion loss process in the bulk of the plasma (see Fig. 8) was considered to be dissociative volume recombination so that for the pure gases the ion density was given by

$$n^- = n^+ = \left(\bar{S}/\alpha_r\right)^{1/2} \tag{26}$$

where α_r is the dissociative recombination coefficient. The applied voltage was assumed to appear across the cathode sheath in order to drag the positive ions out of this sheath and onto the negative electrode. It was assumed that volume recombination could be neglected in the sheath as well as diffusion and the basic particle transport equations in the region reduced to

$$\Gamma^- = -\mu^- E n^- \tag{27}$$

and

$$\Gamma^+ = \mu^+ E n^+ \tag{28}$$

where Γ is the current density of particles and μ the mobility coefficient. Using Poisson's equation and the continuity equations the total current I was derived in terms of the applied voltage V as

$$I = A\left(4\mu^+\epsilon_0 e^3\right)^{1/4} \bar{S}^{3/4} V^{1/2} \tag{29}$$

where A is the area of the negative electrode, ϵ_0 is the permittivity of vacuum and e is the electron charge. Of particular importance was the dependence of the current on the uniform ion generation rate to the 3/4 power and the dependence on the voltage to the 1/2 power.

Ion Transport Model for Non-Uniform Ion Generation Rate

For this ion transport model the ion generation rate $S(r_2, z_2)$ is used. It is expected that the sheath thickness will be relatively uniform over the electrode surface so that radial diffusion of the ions can be neglected. In this case the ion transport equations can be solved as a one dimensional problem and the distribution of potential, ion density and field between the two electrodes of the ion tube can be assumed to be similar to the sketches of Fig. 8.

The basic particle transport equations are Eqs. (27) and (28) and the continuity equations are

$$\frac{d\Gamma^-}{dz}\bigg)_{r_2} = \frac{d\Gamma^+}{dz}\bigg)_{r_2} = S(r_2, z_2).$$ (30)

Equations (28) and (30) when integrated yield

$$n^+(z) = \frac{1}{\mu^+ E} \int_0^z S(z'')\, dz'' \qquad (z > 0),$$ (31)

which evidently can satisfy the approximate boundary conditions $E \rightarrow E_p \simeq 0$ when $z \rightarrow 0$ for finite n^+. For $b < z < d$, $n^+ = [S(z)/\alpha_r]^{1/2}$.

Since $n^+ \gg n^-$ in the sheath Poisson's equation becomes

$$\frac{dE}{dz} = \frac{e}{\epsilon_0}(n^+ - n^-) \simeq \frac{e}{\epsilon_0} n^+ \; ;$$ (32)

combining Eqs. (31) and (32) with the boundary conditions $E=0$ when $z=b$, we find the electric field distribution in the sheath

$$E(z) = \left[\int_0^z dz' \int_0^{z'} S(z'')\, dz'' \right]^{1/2} \left(\frac{2e}{\epsilon_0 \mu^+}\right)^{1/2}.$$ (33)

The potential drop $V_{b(r_2)}$ across the cathode sheath is found by integrating once more, to give

$$V_{b(r_2)} = \left\{ \int_0^{b(r_2)} dz \left[\int_0^z dz' \int_0^{z'} S(z'')\, dz'' \right]^{1/2} \right\} \left(\frac{2e}{\epsilon_0 \mu^+}\right)^{1/2}$$ (34)

which is very nearly equal to the potential drop V across the ionization tube for $b(r_2) \leq d$. Substituting V for $V_{b(r_2)}$ and using the ion generation rate $S(r_2, z_2)$ from Eq. (9), we solve the integral Eq. (34) to obtain $b(r_2)$.

The total ion current (I) collected on the negative electrode of radius ρ_2 is equal to all of those ions generated in the cathode sheath, or

$$I = 2\pi e \int_0^{\rho_2} r_2\, dr_2 \int_0^{b(r_2)} S(r_2, z_2)\, dz_2 .$$ (35)

Since $b(r_2) \leq d$, the electrode separation, the current in Eq. (35) is seen to saturate when $b(r_2)=d$ for all r_2.

If the ion generation rate is uniform over the sheath, i.e. $S(r_2,z_2)=\bar{S}$, then from Eq. (34) $V \simeq V_b = (e\bar{S}/\mu^+ \epsilon_o)(b^2/z)$, $b = \Gamma'/\bar{S} = I/Ae\bar{S}$ and $V = \left[4\bar{S}^3\mu^{+2}\epsilon_o e^3\right]^{-1/2}(I/A)^2$ which is identical to Eq.(29).

The dependence of current on voltage given by Eqs. (34) and (35)(or by Eq. (29)) will break down when diffusion terms become significant. In addition, for large values of $E(z)/p$ in the sheath, the electrons can acquire sufficient energy to cause appreciable multiplication of the current by electron-atom collisions and this effect is likely to be of particular importance in a gas mixture such as neon-argon.

Computer Programs for Ion Transport Model

The solutions of Eqs. (34) and (35) to obtain the current-voltage characteristic requires numerical as well as iterative techniques. Two programs were written for solution on the IBM 7094 computer. The first program was written for a simplified single integral expression for $b(r_2)$ and the program details are described in another report.[2] The second program was written for the complete Eqs. (34) and (35) and solved the triple integral expression Eq. (34) for $b(r_2)$. Both of these versions are described briefly and a comparison of the computed I-V curves is given.

Simplified Single Integral Version In Section C of Reference (1) an integral equation for $b(r_2)$ for the cathode sheath thickness was written by analogy with the uniform ion generation rate model. For a circular parallel plate ionization tube of radius ρ_2,cm and gap d,cm in which one of the electrodes contains a uranium disc of radius ρ_1,cm, the integral equation in Reference (1) for $b(r_2)$ reduces to two expressions depending upon whether the cathode sheath is at the uranium or bare electrode. Those expressions are

$$b^+(r_2) = \frac{\left(4\mu^+\epsilon_o/e\right)^{1/3}}{\left[\int_{z_2=0}^{b(r_2)} S(r_2,z_2)dz_2\right]^{1/3}} V^{2/3}, \quad \left(b^+(r_2) \leq d\right) \tag{36a}$$

and

$$b^-(r_2) = \frac{\left(4\mu^+\epsilon_o/e\right)^{1/3}}{\left[\int_{z_2=d-b^-(r_2)}^{d} S(r_2,z_2)dz_2\right]^{1/3}} V^{2/3}, \quad \left(b^-(r_2) \leq d\right). \tag{36b}$$

24

The tube current is obtained from Eq. (35) using $b(r_2)$ from Eq. (36), i.e.

$$I^+ = 2\pi e \int_{r_2=0}^{P_2} r_2 \, dr_2 \int_{z_2=0}^{b^+(r_2)} S(r_2, z_2) \, dz_2 \qquad (37a)$$

and

$$I^- = 2\pi e \int_{r_2=0}^{P_2} r_2 \, dr_2 \int_{z_2=d-b^-(r_2)}^{d} S(r_2, z_2) \, dz_2 \quad , \qquad (37b)$$

where $b^+(r_2)$ gives the sheath thickness and I^+ the tube current when the uranium electrode is negative (cathode sheath at the uranium electrode) and $b^-(r_2)$ gives the sheath thickness and I^- the tube current when the bare electrode is negative (cathode sheath at the bare electrode). Equations (36) and (37) were coded in Fortran II for solution on the IBM 7094 computer. All numerical integrations were performed by Simpson's rule, using a fixed number of steps (input) for each variable. The solution of the integral Eq. (36) for $b(r_2)$ required iterative techniques and this was done with an existing iterative Fortran subroutine. The input for $S(r_2, z_2)$ was provided as a tabular function from the ion generation rate code. Values of the current I^+ and I^- were computed for a given voltage range at the voltage points fixed by the input values of the upper and lower bounds and the increment size. The computed values of the current were printed out in tabular form for each voltage point and these data could also be punched out in card form. Also a General Motors Research Laboratories multiplotting subroutine (which uses a CRT) was programmed into the code so that the complete I-V curve could be obtained in graphical form by itself or together with the experimental I-V curve if that data had also been provided as card input.

Triple Integral Version   The single integral expression Eq. (36) for $b(r_2)$ gave only an approximate solution to Eq. (34). The complete solution of Eq. (34) for $b(r_2)$ was accomplished numerically by a combination of triple integration and numerical techniques. This program was written as a subroutine and then substituted into the main control program.

Discussion of Solutions for Current-Voltage Characteristics

Examples of the code solutions for the current-voltage characteristics will be given in the next section on the analysis of the inpile data. The discussion here will be limited to a comparison of the output from the single and triple integral versions for the ion transport model and to a comparison of the I-V characteristics using the linear and quadratic energy loss models.

Comparison of Ion Transport Solutions   Code solutions for the I-V characteristics were obtained using both the single and triple integral solutions to Eq. (34) for the case of 240 torr xenon in a neutron flux of 1.4×10^{13} $cm^{-2} sec^{-1}$. The maximum deviation over the entire voltage range (-100 to 100v) was less than 2%. For this case the sheath thickness is very small ($\sim .03$ cm) and therefore the variation in S across the sheath is very small. In order to make the comparison with a large sheath thickness $(b(r_2) \approx .3$ cm) runs were made on each version of the code for the case of 240 torr neon at a neutron flux of $1.2 \times 10^{10} cm^{-2} sec^{-1}$. The maximum deviation in this case was less than $\sim 5\%$. These data showed that the single integral equation was a good approximation for the sheath thickness $b(r_2)$. The triple integral solution did not have an excessive running time and so it has been used throughout the data analysis.

Comparison of Energy Loss Models   Code solutions for the I-V characteristics were obtained using both the linear and quadratic energy loss models for the case of 240 torr xenon in a neutron flux of $1.2 \times 10^{13} cm^{-2} sec^{-1}$. The curves are shown in Fig. 9. As pointed out in Section II some trouble was experienced with the numerical solution for the triple integral solution for $S(r_2, z_2)$ from Eq. (9) when $z_2 \longrightarrow 0$. The curves in Fig. 9, therefore, are for a negative applied voltage where the sheath is at the electrode opposite the uranium $(z_2 \approx d)$ and the quadratic energy loss solution can be obtained without the integration problem. The current values for the quadratic energy loss model were about 9% lower than the values for the linear model and this is consistent with reduced ion generation rate found for the quadratic energy loss model in Section II.

Since this difference in current values for the two energy loss models is within the accuracy by which some of the other variables are known, such as neutron flux, the simpler and more rapid single integral solution for the linear energy loss model was used in all further computations.

26

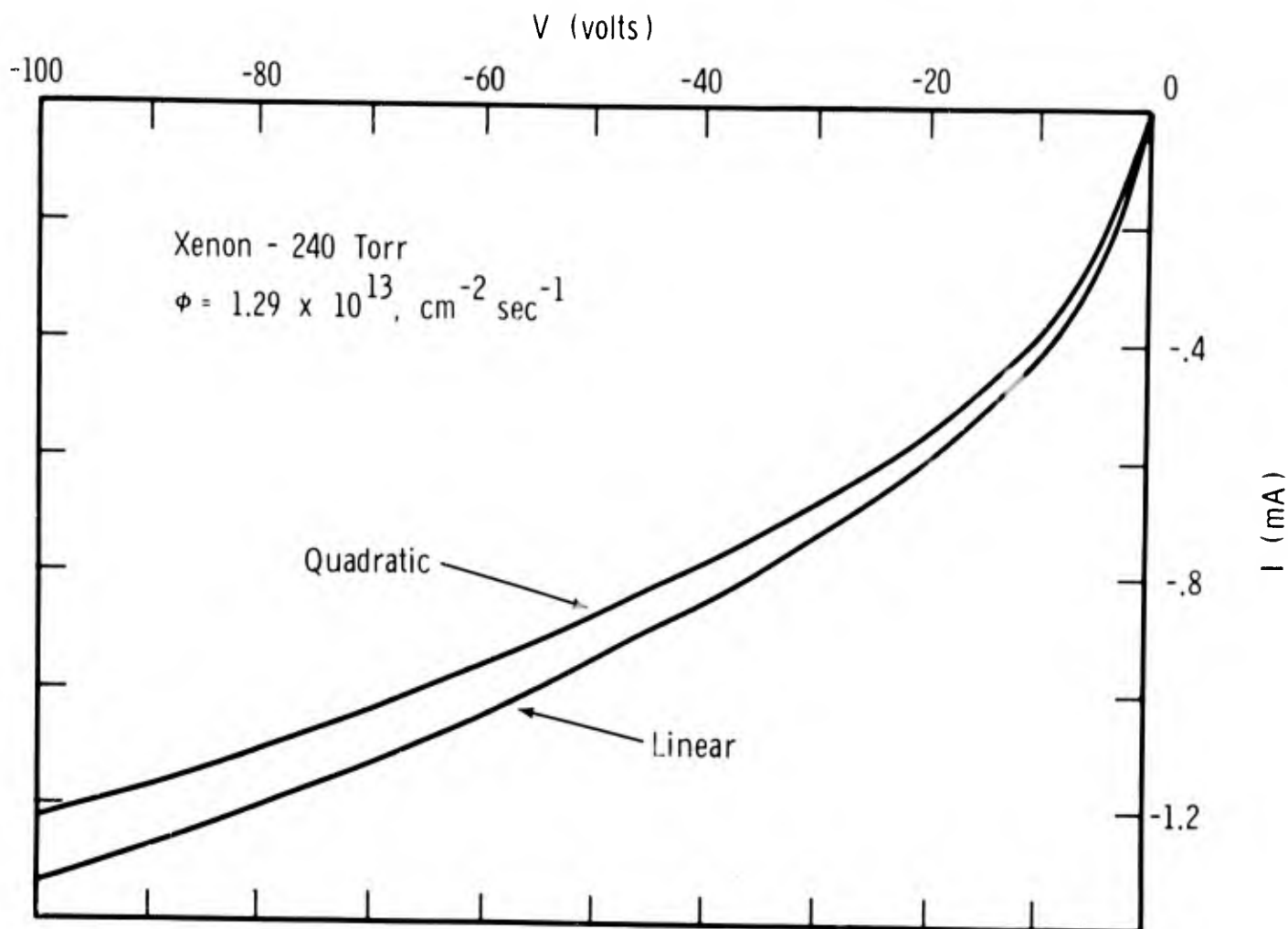Fig. 9. Comparison of the I-V characteristics for the linear and
quadratic energy loss models for the fission fragments.

IV. ANALYSIS OF INPILE DATA ON IONIZATION TUBE

The inpile data obtained with the ionization tube on pure and mixed noble gases were described in detail in a previous report.[1] A sketch of the ionization tube is reproduced in Fig. 10.
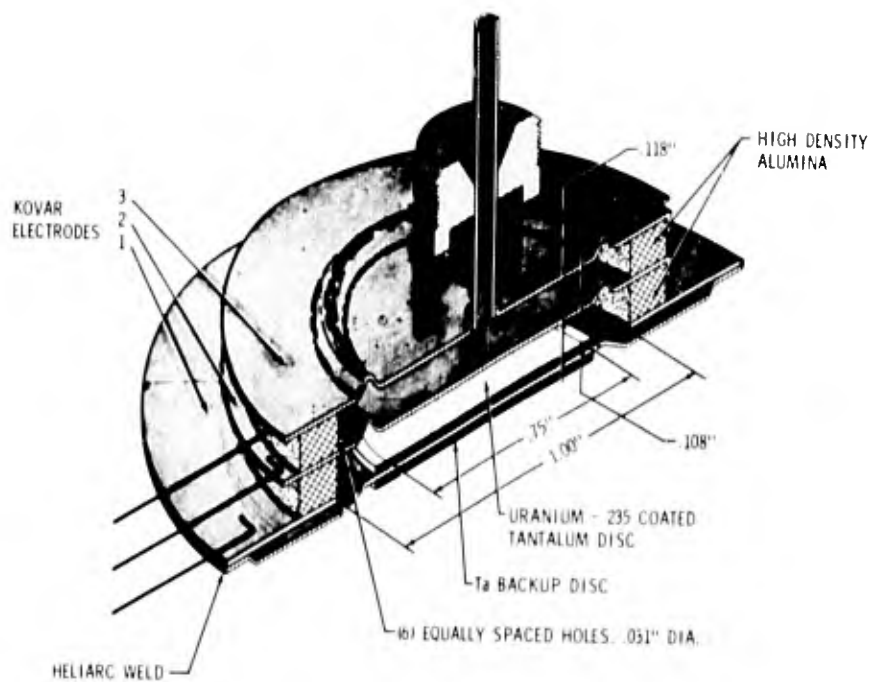

Fig. 10. Ceramic-metal ionization tube

The tube had 3 Kovar electrodes, essentially planar, which were brazed to ceramic rings to form two ionization chambers each of gap 0.3 cm. In the ionization experiments described here only the fission fragment ionization process was of interest so thermionic electron emission was suppressed by using a thin uranium foil which minimized heat generation. The upper chamber did not contain uranium and ionization was due to γ irradiation only, whereas the ionization produced in the lower chamber was due to both fission fragments and γ radiation. By making current-voltage measurements with both diodes it was possible to establish that the ion generation rate due to γ radiation was only 1% of that due to fission fragments.

Current-voltage characteristics for various gas pressures of neon, argon, xenon and neon-argon $(Ar/Ne=10^{-3})$ were obtained at reactor power levels of 10, 100, 1000 and 2000 kilowatts. These data have been analyzed with the ion generation rate code using the linear energy loss model and the current-voltage characteristic code using the triple integral solution for the sheath thickness. The values of the constants used in the equations are listed in Table 2. The fit of theory to experiment is discussed for the pure gases first and then for the neon-argon mixture.

TABLE 2

Constants

	Light Fragment (j=1)	Heavy Fragment (j=2)
Average Group Properties of the Fission Fragments		
Initial kinetic energy, E_o, Mev[17]	98	67
Mass, Amu[17]	95	139
Initial charge, Z_o, eu[17]	20	22
Range in air, R_a, cm[18]	2.5	1.9
Range in U-Ni, R_1, cm	6.65×10^{-4}	5.05×10^{-4}
Energy to create an ion pair, $\bar{w}$, ev		
$\bar{w}/w_\alpha$ where $\bar{w}=(\bar{w}/w_\alpha)w_\alpha$ [4]	1.06	1.11
$\bar{w}$(Ne) (w_α=36.8 ev[10])	39.0	40.8
$\bar{w}$(Ar) (w_α=26.4 ev[10])	28.0	29.3
$\bar{w}$(Xe) (w_α=21.9 ev[10])	23.2	24.3
$\bar{w}$(Ne-Ar,0.1% Ar) (w_α=26.1[11])	27.7	29.0

Fission Cross Section, Q_f, cm^{-1} : 21.7

Properties of the Gases

Ion mobility at 760 torr and 273°K, μ_o, $cm^2 volt^{-1} sec^{-1}$

$\mu_o(Ne^+)$ in Neon[12]	4.1
$\mu_o(Ne_2^+)$ in Neon[12]	6.5
$\mu_o(Ar^+)$ in Argon[12]	1.6
$\mu_o(Ar_2^+)$ in Argon[12]	1.9
$\mu_o(Xe^+)$ in Xenon[13]	.58
$\mu_o(Xe_2^+)$ in Xenon[13]	.79
$\mu_o(Ar^+)$ in Neon[14,15]	7.5
$\mu_o(Ar_2^+)$ in Neon[14,15]	6.8

Recombination Coefficient (Dissociative)

$\alpha_r(Ne_2^+)$, $cm^3 sec^{-1}$[16]	2.2×10^{-7}
$\alpha_r(Ar_2^+)$, $cm^3 sec^{-1}$[16]	6.7×10^{-7}
$\alpha_r(Xe_2^+)$, $cm^3 sec^{-1}$[16]	1.4×10^{-6}

Pure Gases

The experimental data for the pure gases neon, argon and xenon at 240 torr pressure and a neutron flux of $1 \times 10^{13} cm^{-2} sec^{-1}$ are shown in Fig. 11. For clarity these data are shown as points although each I-V characteristic was swept out with an x-y recorder. The experimental characteristics generally all followed a $V^{1/2}$ dependence on voltage and $\phi^{3/4}$ dependence on neutron flux as predicted by Eq. (29).

The computed I-V characteristics for neon, argon and xenon at 240 torr pressure and a neutron flux of $1 \times 10^{13} cm^{-2} sec^{-1}$ are shown as the solid curves in Fig. 11. The fit of the theory to the experimental data is good. For the negative quadrant the entire area of the Kovar electrode was used for the ion collecting area while for the positive quadrant the ion collecting area was limited to just the uranium area. This was justified by the following arguments.

When the applied voltage is negative (Kovar electrode negative with respect to the uranium) the cathode sheath is at the Kovar electrode and the ion generation rate is more uniform (see Fig. 7). For this condition the fit is good and the theoretical curves for neon, argon and xenon are about 10% higher than the experimental values.

For a positive applied voltage the cathode sheath is at the uranium electrode. The ion generation rate drops sharply with distance past the edge of the uranium disc (see Fig. 7) and the contribution to the total current for $r_2 > \rho_1$ is therefore small. More importantly, however, for $r_2 > \rho_1$ the Kovar supporting the uranium bends away from the uranium and the ions must be transported to the electrode across a region where the ion generation rate is zero (see Fig. 10). It can be shown that most of the applied voltage occurs across this region of zero ion generation rate and the current contribution is further reduced. The code was not programmed to take into account this detail of the tube geometry so that for the theoretical curves for $V > 0$, the ion collecting electrode radius ρ_2 was set equal to ρ_1. Even with the reduced collecting area for $V > 0$ the current was higher with the cathode sheath at the uranium electrode. This results from the decrease of the ion generation rate with distance from the uranium surface (see Fig. 5).

The shape of all of the experimental I-V curves for the pure gases followed very closely the $V^{1/2}$ dependence predicted in Eq. (29). The increasing current values (at constant voltage) for the gases in the order neon, argon

and xenon reflect the increase of fission fragment energy loss and the increase of the ion generation rate with higher atomic mass of the gas atom. The computed ion generation rates at the midpoint of the tube are listed at the bottom of Fig. 11. For neon, argon and xenon they are $(1.8, 3.6$ and $8.1) \times 10^{16} cm^{-3} sec^{-1}$, respectively.

Neon-Argon Mixture with Ar/Ne=1 x 10^{-3}

The experimental I-V data for the neon-argon mixture at 240 torr and $1.0 \times 10^{13} cm^{-2} sec^{-1}$ neutron flux are plotted as the points in Fig. 12. For $|V| < 25$ volts the current is roughly proportional to $V^{1/2}$ (see dashed curve) and is about twice that for pure neon (Fig. 11). At about 25 volts the electric field becomes sufficiently great to cause electron impact ionization in the sheath and the current then increases rapidly with voltage.

The theoretical curve was obtained with the code using $w_\alpha = 26.1$ ev/ion pair[11] for the neon-argon mixture with Ar/Ne=10^{-3} and the range of the fission fragments used was the same as for pure neon. The experimental current was higher than the theoretical current for $(-25$ volts $< V < +25$ volts) and this was attributed to the diffusion of Ar^+ ions from the bulk of the plasma into the sheath. This conclusion is supported by the fact that good agreement was obtained at 400 torr pressure (as shown in Fig. 13 for the negative quadrant when the cathode sheath is at the Kovar electrode) and as the pressure decreased down to 30 torr the observed current became progressively greater than that computed. The ion generation rate for the neon-argon mixture at 240 torr $(2.6 \times 10^{16} cm^{-3} sec^{-1})$ is 40% greater than that for pure neon and this is attributed to the Penning effect which results from the ionization of argon by the metastable states of neon.

The good agreement between theory and experiment for pressures of 240 and 400 torr is taken to indicate that the computation of the ion generation rate, including the geometrical effects, is valid. Table 3 gives values of S computed for the midpoint along the tube axis for the gases studied. These values of S are higher than the average values previously reported[1] from a one parameter fit of the ion transport model to the experimental data. The present calculations for S using the computer code can now be utilized to determine the spatial distribution of S for a wide range of parameters.

Also shown in Table 3 are values of electron density corresponding to the ion generation rates. The electron densities for the pure gases were calculated from the ion generation rate and the dissociative recombination coefficient,[1] i.e. $N_e = (S/\alpha_r)^{1/2}$. The determination of the electron density for the Ne-Ar mixture is discussed in Section C of this report.

TABLE 3

Ion Generation Rate and Plasma Density at Midpoint of Gap

$$\text{Gas pressure} = 240 \text{ torr}$$
$$\text{Neutron flux} = 1.0 \times 10^{13} \text{cm}^{-2}\text{sec}^{-1}$$

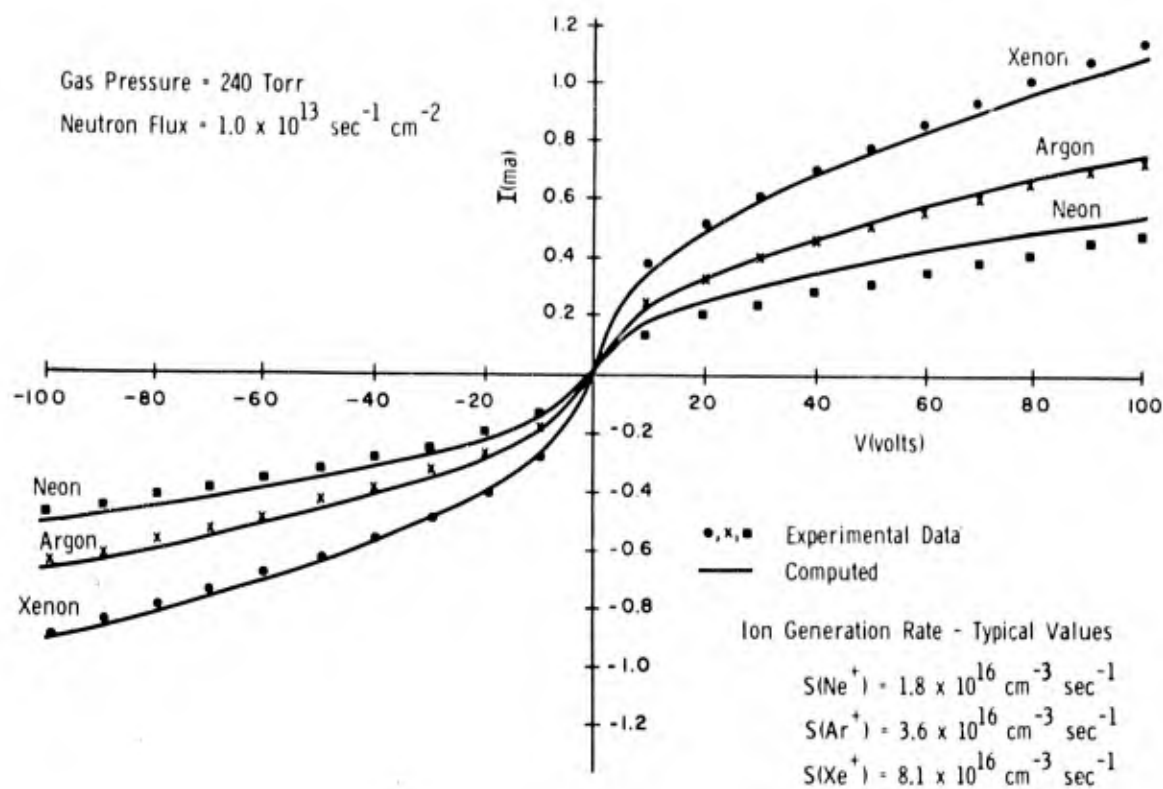| Gas	Ion Generation Rate $(\text{cm}^{-3}\text{sec}^{-1})$	Recombination Loss Process	Electron Density (cm^{-3})
Neon	1.8×10^{16}		2.9×10^{11}
Argon	3.6×10^{16}	$y^+ + 2y \longrightarrow y_2^+ + y$ $y_2^+ + e^- \longrightarrow 2y$	2.3×10^{11}
Xenon	8.1×10^{16}		2.4×10^{11}
Neon-Argon (0.1% Ar)	2.6×10^{16}	Ne^+ as above $Ar^+ + Ar + Ne \longrightarrow Ar_2^+ + Ne$ $Ar_2^+ + e \longrightarrow 2\,Ar$	1.0×10^{12}

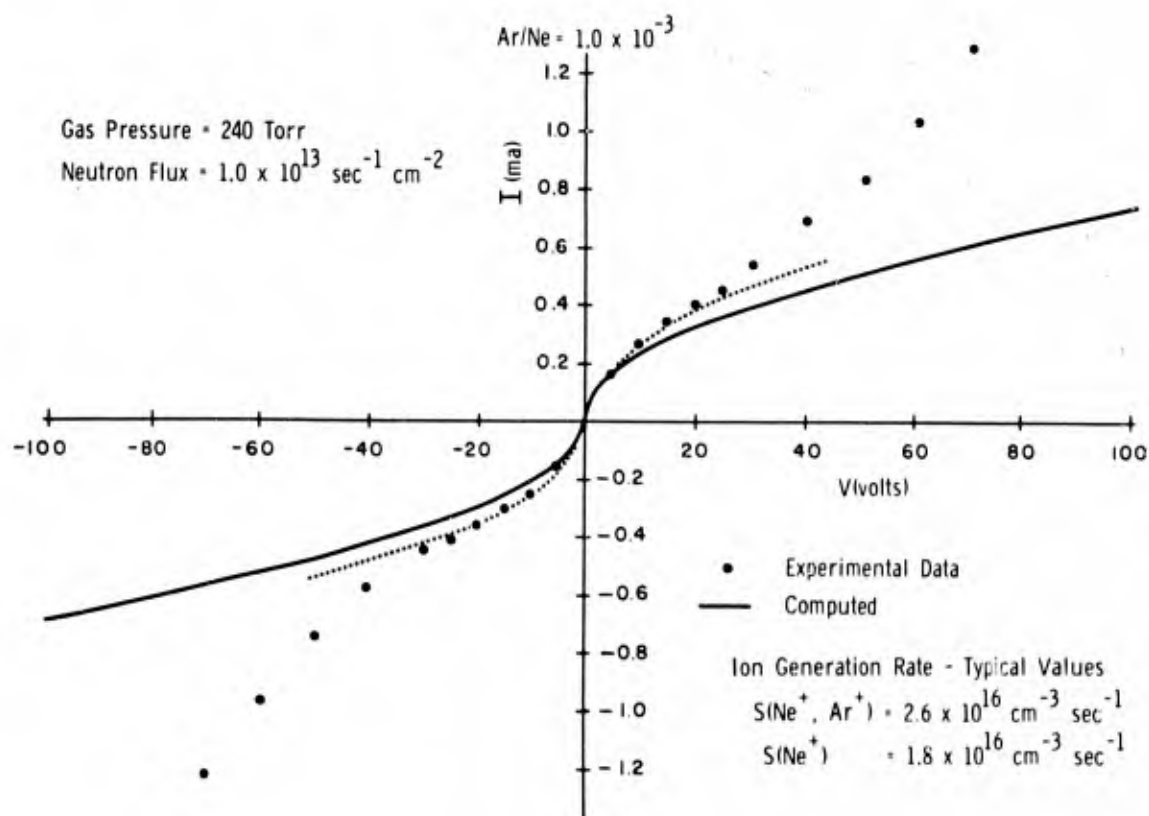Fig. 11. Current-voltage data in neon, argon and xenon.

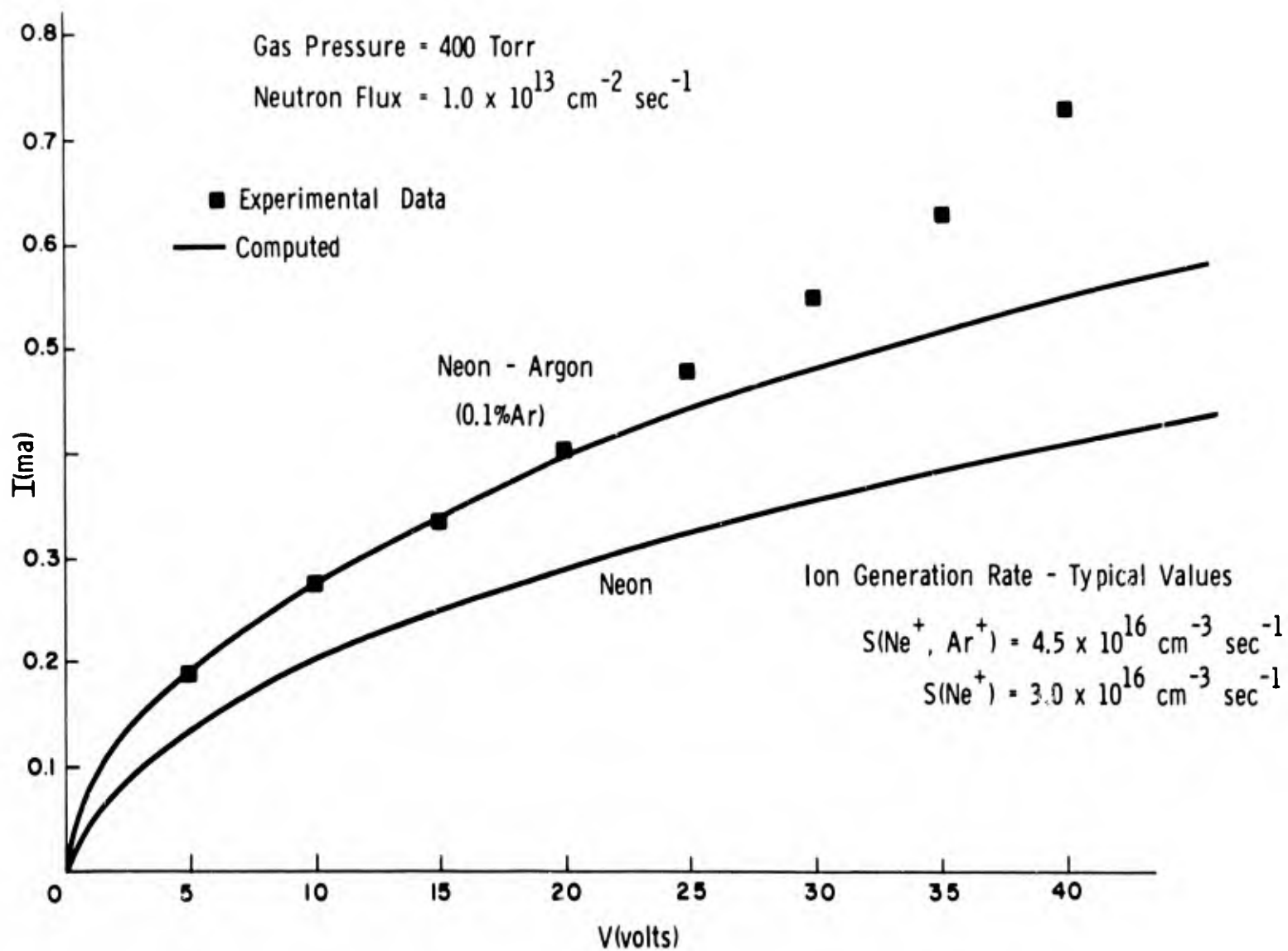Fig. 12. Current-voltage data in the neon-argon mixture.

Fig. 13. Current-voltage data in Ne-Ar(0.1% Ar) at 400 torr pressure.
The applied voltage is negative and the cathode sheath is at
the Kovar electrode.

34

V. REFERENCES

1. C. B. Leffert, D. B. Rees and F. E. Jamerson, ONR Annual Report No. 5, Contract Nonr-3109(00), Oct. 1964.

2. W. Butterfield, General Motors Research Laboratories Internal Report, in press.

3. H. A. Bethe and J. Ashkin, Experimental Nuclear Physics, E. Segré(ed.), (New York: John Wiley and Sons, Inc., 1953), 1: Part II, p. 166.

4. H. W. Schmitt and R. B. Leachman, Phys. Rev. 102, 183 (1956).

5. L. O. Herwig and G. H. Miller, Phys Rev. 95, 417 (1954).

6. J. K. Knipp and R. C. Ling, Phys. Rev. 82, 30 (1951).

7. M. Steinberg, Nucleonics 21, 151 (1963).

8. W. H. Bragg and R. Kleeman, Phil. Mag. 10, 318 (1905).

9. R. D. Evans, The Atomic Nucleus, p. 652 (McGraw-Hill, New York, 1955).

10. W. P. Jesse and J. Sadauskis, Phys. Rev. 90, 1120 (1953).

11. W. P. Jesse and J. Sadauskis, Phys. Rev. 88, 417 (1952).

12. H. J. Oskam and V. R. Mittelstadt, Phys. Rev. 132, 1435 (1963).

13. M. A. Biondi and L. M. Chanin, Phys. Rev. 94, 910 (1954).

14. L. M. Chanin and M. A. Biondi, Phys. Rev. 107, 1219 (1957).

15. S. C. Brown, Basic Data of Plasma Physics, (Wiley), (1959).

16. H. J. Oskam and V. R. Mittelstadt, Phys. Rev. 132, 1445 (1963).

17. J. N. Anno, J. Appl. Phys. 5, 1678 (1962).

18. R. D. Evans, The Science and Engineering of Nuclear Power, C. Goodman (ed.), pp. 1 - 74, (Addison-Wesley Press, 1949).

SECTION B

SECTION B

REACTION KINETICS OF THE FISSION FRAGMENT PLASMA[*]

ABSTRACT

The atomic and ionic reactions in a plasma formed by fission fragments in Penning gas mixtures are analyzed. Seven equations are written for atomic and molecular ions of both major and minor species, metastable atoms of the major species, excited states other than metastable of the major species, plus charge neutrality. Approximate solutions are obtained for the major and minor gas constituent density, to give maximum electron density. The classical Penning effect - increase in ion source rate because of conversion of major species metastable atoms to minor species ions - is a relatively small advantage. Much more important is the decrease in minor species atomic ion loss rate. This rate can be drastically reduced by operating in the regime of parameters where atomic ions of the minor species must form molecular ions via 3-body collisions. This process can be made very slow. Examples are given for neon-argon gas.

CONTENTS

BLANK PAGE

1. The Problem

We consider a tube such as that discussed in Section A, filled with either a single gas species or a Penning mixture and containing a uranium fission source such that when operated in a reactor a copious flux of fission fragments is passed through the gas. The fragments may ionize or excite neutral atoms; metastable atoms may be formed. These particles interact among themselves and with each other, can diffuse to the tube walls and the ions can recombine with electrons (there are no negative ions). Despite the appreciable variation in the fission-fragment ionization rate across the tube discussed in Section A, the effect of such variations is small in the present study of the number densities of various species in the plasma. The particle density distributions in the plasma are dominated by the influence of such loss processes as diffusion or recombination and the ion generation rate can be considered effectively uniform throughout the tube volume without much error.

The problem is: first, to create equations governing the processes; second, to find coefficients for the rate processes; third, to find solutions for the interacting particle densities.

2. The Equations

Specifically, we assume a majority gas of fixed neutral density N_o, which is ionized to an ion density N_+. There can also be metastable atoms with density N_m, excited states N_x that are not metastable, and even molecular ions N_{2+}. There may be a minor Penning constituent with neutral density A_o, atomic ion density A_+, molecular ion density A_{2+}. We ignore the presence of all excited states A_x and A_m, because these cannot yield ions via any linear process.

The first equation is charge neutrality

$$N_e - N_+ - N_{2+} - A_+ - A_{2+} = 0 \tag{1}$$

The six equations for N_+, N_x, N_m, N_{2+}, A_+ and A_{2+} are shown on the next page in semi-tabular form. The steady state solution with all derivatives zero is desired. We now discuss these equations one at a time.

Equations for Particle Density Time Derivatives

Time Der.	From Direct Flux	Diff.	Recombination	3-Body Mol.Ion Formation	2-Body Ch. Exch.	Meta-Meta Coll.	Radiation	Mol.Ion Formation via N_x	Meta Destruct via N_o	Penning	Eq. No.
$\dfrac{\partial N_+}{\partial t} =$	$S_o N_o$	$-D_1 \nabla^2 N_+$	$-\left[C_1 + C_2 N_o + C_3 N_e\right] N_+ N_e$	$-C_4 N_+ N_o^2$ $-C_5 N_+ N_o A_o$	$-C_6 N_+ A_o$	$+C_7 N_m^2$		$-C_9 N_x N_o$			(2)
$\dfrac{\partial N_x}{\partial t} =$	$S_1 N_o$		$+C_8\left[C_1 + C_2 N_o\right] N_+ N_e$				$-N_x/\tau_x$	$-C_9 N_x N_o$			(3)
$\dfrac{\partial N_m}{\partial t} =$	$S_2 N_o$	$-D_m \nabla^2 N_m$	$+C_{10}\left[C_1 + C_2 N_o\right] N_+ N_e$ $+C_{11}C_{16}N_{2+}N_e$			$-C_{12}N_m^2$			$-C_{13}N_o N_m$ $-C_{14}N_o^2 N_m$	$-C_{15}N_m A_o$	(4)
$\dfrac{\partial N_{2+}}{\partial t} =$		$-D_2 \nabla^2 N_{2+}$	$-C_{16}N_{2+}N_e$	$+C_4 N_+ N_o^2$	$-C_{17}N_{2+}A_o$			$+C_9 N_x N_o$			(5)
$\dfrac{\partial A_+}{\partial t} =$		$-D_3 \nabla^2 A_+$	$-(C_{18}+C_{19}N_o)N_e A_+$	$-C_{20}A_o A_o N_c$	$+C_6 N_+ A_o$ $+C_{17}N_{2+}A_o$					$+C_{15}N_m A_o$	(6)
$\dfrac{\partial A_{2+}}{\partial t} =$		$-D_4 \nabla^2 A_{2+}$	$-C_{21}A_{2+}N_e$	$+C_{20}A_o A_o N_o$							(7)

(a) N_+

N_+ is made by a volume source route $S_o N_o$; note that S_o is the source rate density per neutral atom, and has the dimension (sec^{-1}). These ions diffuse (coefficient D_1) and can recombine with electrons (2-body radiative C_1, 3-body with a neutral C_2, 3-body with extra electron C_3). We shall neglect C_3 because $N_o \gg N_e$, hence $C_2 N_o \gg C_3 N_e$. Note that the various coefficients C have various dimensions suitable to each occasion.

N_+ is also produced by collision of two metastables (C_7), and are converted via 3-body molecular ion formation (C_4) to N_{2+}. They are also converted to A_+ via 2-body charge transfer with $A_o (C_6)$. We shall ignore the 3-body collisions $C_5 N_+ A_o N_o$ compared with $C_4 N_+ N_o^2$.

(b) N_x

N_x is created by primary radiation (S_1) and from a fraction $C_8 \lesssim 1$ of the N_+ recombinations. It is lost via radiation (τ_x), and by the molecular ion conversion process C_9 (the excited atom strikes a neutral to form a molecular ion, before radiating).

(c) N_m

N_m is created by primary radiation, by a fraction $C_{10} < 1$ of the N_+ recombinations, and by a fraction $C_{11} < 1$ of the N_{2+} recombinations. It is lost via diffusion D_m, and via metastable-metastable collisions C_{12}; we must have $C_{12} \gtrsim C_7$. It is also lost via 2-body destruction with neutrals (C_{13}) and 3-body destruction C_{14}. Very importantly, N_m is converted to A_+ via the Penning process C_{15}.

(d) N_{2+}

N_{2+} (and A_+ and A_{2+}) is not created in appreciable amount via the primary radiation. Thus N_{2+} is created by the 3-body conversion of N_+ and conversion of N_x, already described. It is lost via diffusion (D_2), dissociative recombination C_{16} and charge transfer with A_o to form A_+.

(e) A_+

A_+ is formed most importantly via the Penning process C_{15}, and also via C_6 and C_{17} already described. It is lost via diffusion D_3, radiative recombination with electrons (C_{18}), 3-body recombination using neutral N_o (C_{19}), and 3-body collisions to form A_{2+} (C_{20}). Note that this last process reads

$$A_+ \; + \; A_o \; + \; N_o \; \longrightarrow \; A_{2+} \; + \; N_o \; ;$$

the collisions

$$A_+ \; + \; N_o \; + \; N_o \; \longrightarrow \; ?$$
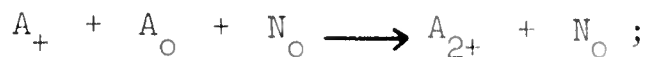
occur much more frequently, but we deny the existence of $(AN)_+$.

(f) A_{2+}

A_{2+} is formed via C_{20} just described, and is lost by diffusion (D_4) or dissociative recombination C_{21}.

3

3. A Pure Gas (Argon)

The preceding equations are too numerous for comfort, so we seek preliminary insight from a simple case. We assume only one gas, thus eliminating Eqs. 6 and 7. The principal effect of N_m was to make A_+, which now can no longer happen. The only remaining contribution could be N_+ via $C_{12}N_m^2$, and this is non-linear and (if $S_2 \lesssim S_o$) cannot lead to any large change in N_+. Thus we ignore N_m also. Finally, we shall ignore N_x on the following more subtle basis: If N_o is high enough to make C_9 an important process, then N_o is probably also high enough to make C_4 a very important process too. Thus virtually all the ions are molecular; but surely $S_o > S_1$, and many states radiate in spite of this process. Hence the contribution of C_9 is not expected to be large.

Finally, we replace ∇^2 by $1/\Lambda^2$, where Λ is the diffusion length. This approximation is valid in the regime where diffusion dominates, i.e., where the term is important. It is incorrect only in the regime where it is small compared to some other loss term. The resulting steady state equations are:

$$0 = S_o N_o - \frac{D_1 N_+}{\Lambda^2} - C_4 N_+ N_o^2 \quad , \tag{8}$$

$$0 = C_4 N_+ N_o^2 - \frac{D_2 N_{2+}}{\Lambda^2} - C_{16} N_{2+} N_e \quad , \tag{9}$$

$$0 = N_e - N_+ - N_{2+} \quad . \tag{10}$$

We are interested in the density N_e, and the effect of varying the parameters. Particularly, we are interested in the effect of varying N_o. Now $D \propto 1/N_o$, hence we write

$$\left.\begin{array}{l} D_1 = K_1/N_o \\[2em] D_2 = K_2/N_o \end{array}\right\} \tag{11}$$

and N_o appears explicitly.

There are two simple limits for these equations. At low pressure $N_o \longrightarrow 0$, diffusion is large, 3-body conversion is negligible, and all ions are N_+. The solution is

$$N_e = \frac{S_o N_o^2 \Lambda^2}{K_1} \quad . \tag{12}$$

The other limit obtains at very high pressure - no diffusion, instant conversion to N_{2+}, and a density limit given by recombination:

$$N_e = \left[\frac{S_o N_o}{C_{16}}\right]^{1/2} \tag{13}$$

4

Under some circumstances, there is an interesting anomaly in the mid-range describable physically as follows. If the recombination C_{16} is large (circumstances can always be arranged so that it is "large"), we wish to prevent ions from recombining. But if the N_e is large, this can only be done by preventing formation of N_{2+} in the first place. Thus we can set $N_e = N_+$, and

$$N_e \approx \frac{S_o N_o}{\dfrac{K_1}{\Lambda^2 N_o} + C_4 N_o^2} \tag{14}$$

This quantity is a maximum at the neutral density

$$N_o = (2 K_1 / \Lambda^2 C_4)^{1/3} , \tag{15}$$

where

$$N_e = S_o (4 \Lambda^2 / 27 K_1 C_4^2)^{1/3} . \tag{16}$$

It is instructive to compare Eqs. 13 and 16. Since $N_e \propto N_o^{1/2}$ at high density, we can in principle make N_e arbitrarily large just by increasing N_o. But this is unattractive, because of plasma resistance, and so forth. If N_o is limited by practical considerations, then Eqs. 15 and 16 may in fact predict a more interesting regime of operation at relatively low density N_o.

Of course, there is nothing wrong with solving Eqs. 8 - 10 directly. We have

$$N_e^2 + N_e \left\{ \frac{K_2}{N_o \Lambda^2 C_{16}} - \frac{S_o N_o}{\left(\dfrac{K_1}{N_o \Lambda^2} + C_4 N_o^2 \right)} \right\}$$

$$- \frac{S_o N_o}{C_{16}} \frac{\left(\dfrac{K_2}{N_o \Lambda^2} + C_4 N_o^2 \right)}{\left(\dfrac{K_1}{N_o \Lambda^2} + C_4 N_o^2 \right)} = 0 , \tag{17}$$

but the behavior of the solution is not so readily apparent without the physical argument.

We illustrate the situation, using argon, and take the following coefficients:

$$S_o N_o = (1.65) 10^{16} \ (cm^{-3} \ sec^{-1}) \ \text{at 240 Torr,}$$

so that

$$S_o = 1.96 \times 10^{-3} \ sec^{-1}$$

$$C_{16} = 6.5 \times 10^{-7} \ cm^3 \ sec^{-1}.$$

For the coefficients K, we note a mobility 1.6 for the atomic ion (here called N_+). We use

$$D_1 = D_a = 2D_+ = \left(\frac{2 \, k \, T_+}{e}\right) \mu_+ = \left(\frac{2 \, k \, T_+}{e}\right) \left(\frac{\mu_+ \, N_o}{N_o}\right)$$

and set $kT_+/e = 0.08$ ev. Since $\mu_+ N_o =$ constant and $\mu_+ = 1.6$ at $N_o = 2.79 \times 10^{19}$ cm^{-3}, we find

$$K_1 = 0.71 \times 10^{19}$$

Similarly $K_2 = 1.15 \times 10^{19}$ for the molecular ion, using $\mu = 2.6$ cm^2/volt-sec.

Finally, we must guess about C_4. It is reported that the frequency for $He^+ + 2He \longrightarrow He_2^+$ is ≈ 70 p^2, where p = Torr. We shall take 100 p^2, whence we find

$$C_4 = 8 \times 10^{-32}.$$

Note that if C_4 is smaller, the anomalous electron density will be higher.

Figure 1 shows the result of solving Eq. 17, for three flux. One is $S_o = 1.96 \times 10^{-3}$ sec^{-1}, corresponding roughly to 10^{13} neutrons/cm^{2}sec, and the other two are flux of 0.1 and 10.0 times that flux. The previous popular operating density was $\approx 8.5 \times 10^{18}$ cm^{-3}, - 240 Torr. The region around 2.8×10^{-7} cm^{-3}, 8 Torr, looks interesting. In particular, the anomaly is large at high flux. It appears that the simple eqs. 15 and 16 are valuable, because they predict the maxima shown by crosses in the three cases. The approximation is good when a maximum exists, as we would expect.

4. Simplified Description of the Penning Mixture Physics

Figure 2 shows all the reactions given in Eqs. 2-7. The electron population is not shown specifically, but the appearance of electrons or atoms with any reaction is shown by an appropriate input arrow. Note that the only feedback loop is C_7 (metastable-metastable collisions leading to ionization). These equations can easily be programmed for a computer but here we desire a little preliminary insight.

Figure 3 shows in bold outline two parts of the reaction paths. The upper part is the pure gas problem described in the previous section. We turn our attention now to the whole diagram; then in a few moments to the lower emphasized part.

The object of having a Penning mixture is to increase the charge density in the plasma. We can do this by increasing the ion production or decreasing the ion loss. The Penning mixture increases the ion production by converting metastables of the majority gas to ions (of the minority gas). Thus in Fig.2 (or 3), we add the source S_2 to the source S_o. But $S_2 \lesssim S_o$; while we increase the ion production, we do so only modestly.

Note that the huge increase in ionization normally thought to be associated with a Penning mixture is here absent. The reason is simple: the classic benefits of a Penning mixture come about from having an electron energy
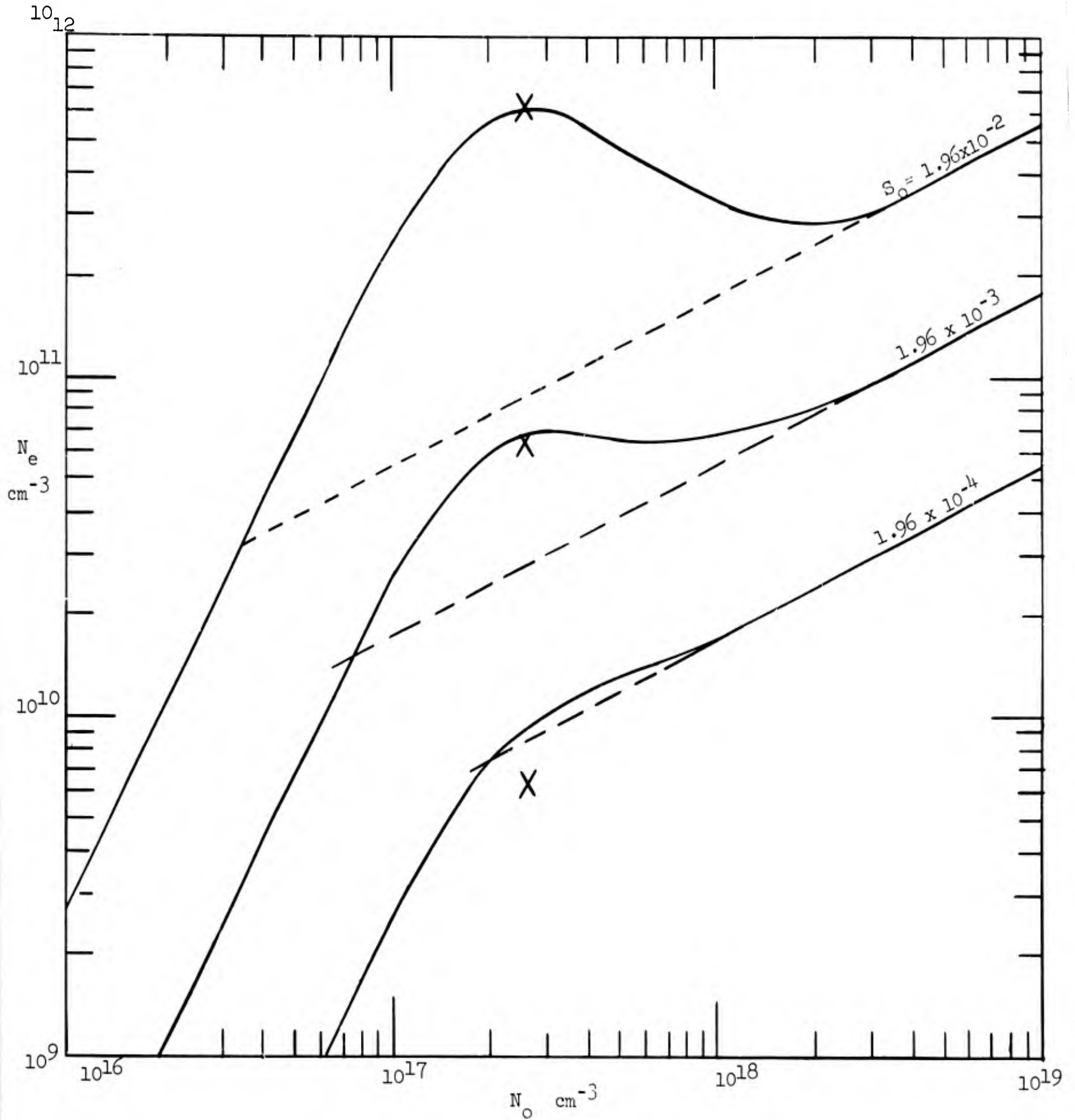
Figure 1 - Electron density vs neutral density in an argon-filled tube, various flux. See text for parameters.
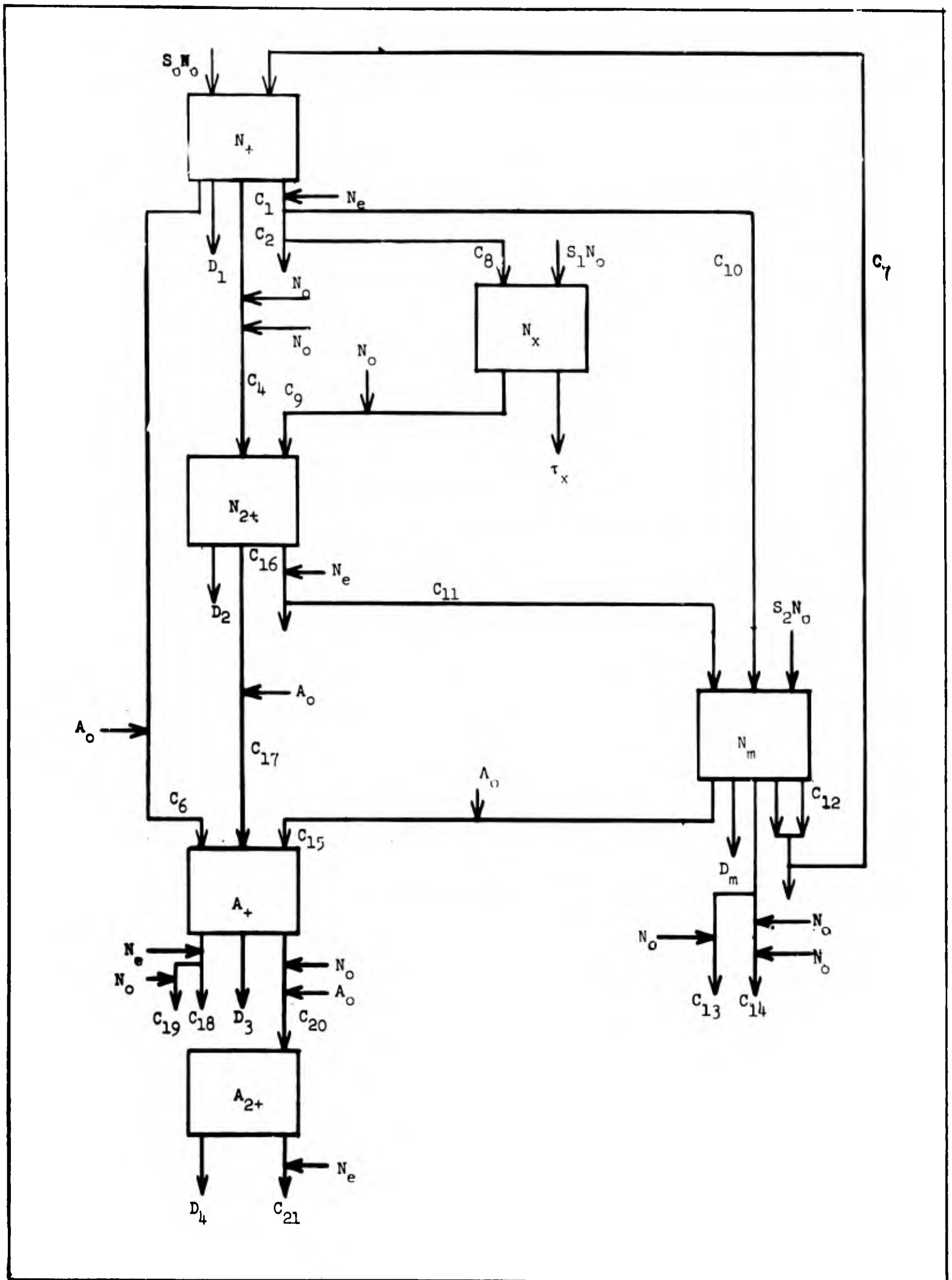
7

Figure 2 - Reaction diagram corresponding to Eqs. 2 - 7, for production and loss of ions N_+, N_{2+}, A_+, and A_{2+}.
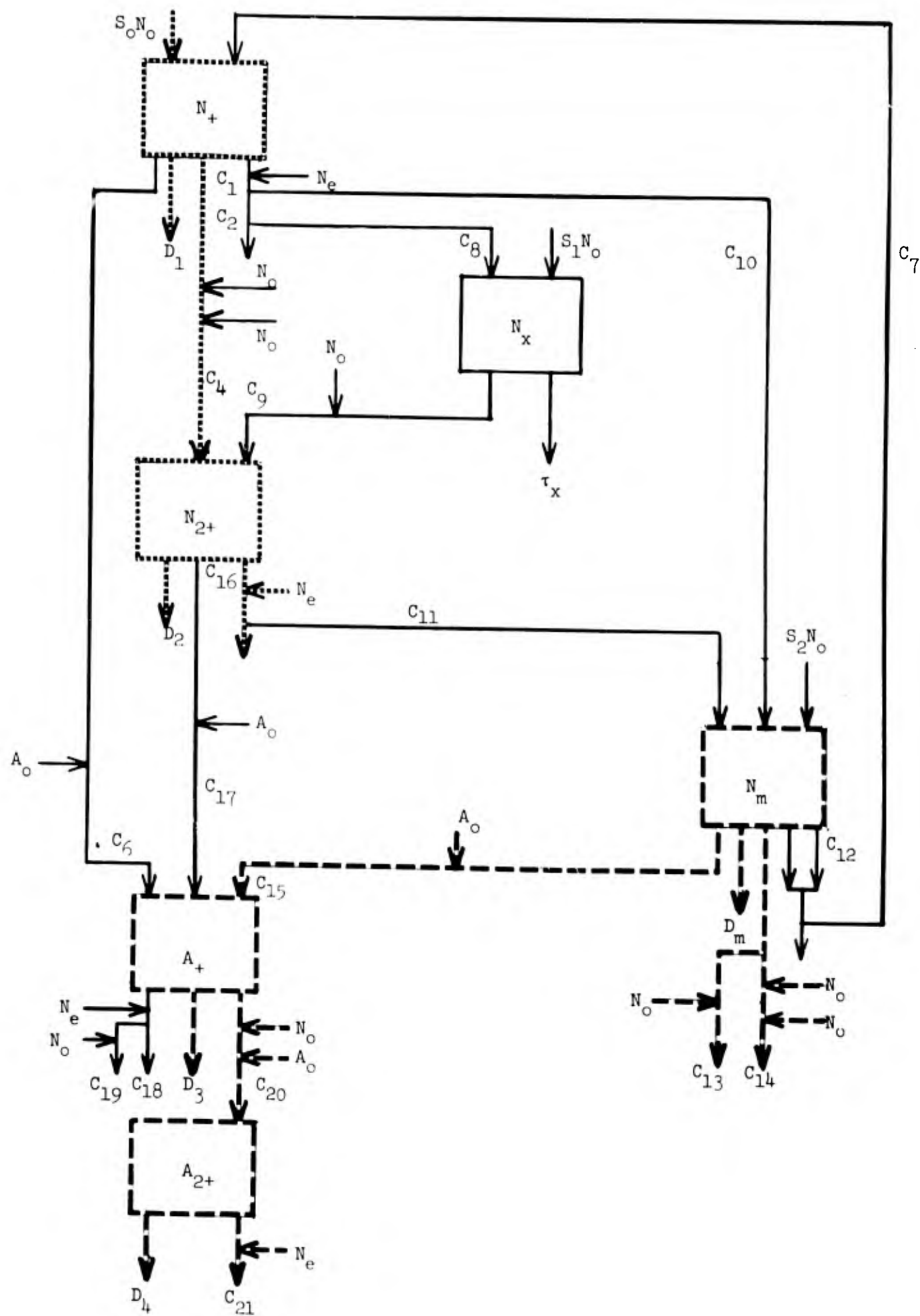
Figure 3 - Principal reaction sub-diagrams for N_+ ions (bold dotted) and for A_+ ions (bold dashed).

distribution f(u) of the shape shown by curve 1 of Fig. 4, maintained by an applied electric field. Because of "elastic collision" energy loss at low
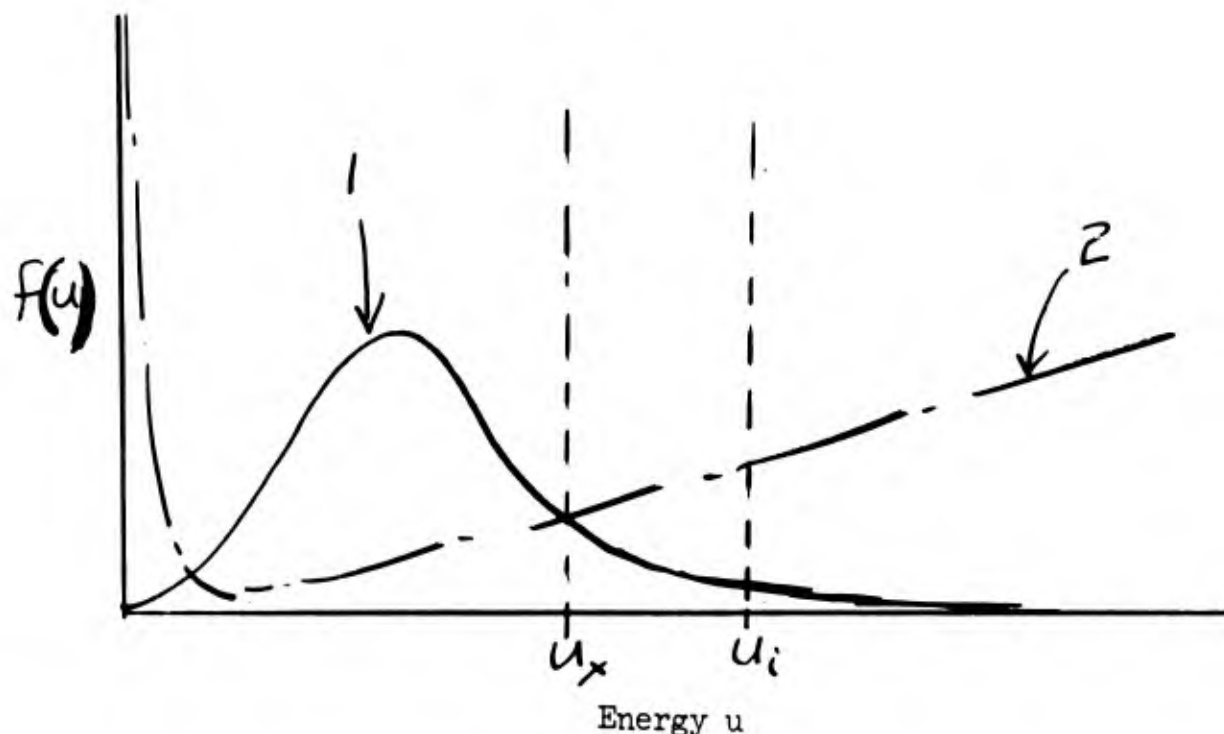

Figure 4 - Artist's conception of electron distribution functions
(1) in which electrons are heated from low energy, and
(2) in which electrons slow down from high energy.

energy, some electrons have energy above u_x and make metastables. These convert to ions of the minor species, and thus we have a good supply of ions where there were formerly very few. The electron distribution here is shown in curve 2: all the thermal electrons near u = 0, plus the slowing down distribution at higher energy. Here ionization proceeds with vigor, and the excitation of metastables is a modest correction. In summary, the classic Penning effect is important when the (energy/ion) is very high. In our cases, the (ev/ion) is purposely made low, and only moderate improvements are to be expected.

To be sure, these moderate source improvements are desirable, but much more important is the reduction in loss rate, a quite different phenomenon. In Figs. 2 or 3, we wish to block the paths by which any one of the ion species disappears, without unduly hindering its production. Indeed, this is what happened in the previous section: the loss rate of N_+ was minimized to obtain the anomalously high electron density.

Now look at the lower emphasized part of Fig. 3. The production terms are different, involving the metastable N_m; but here we see that the loss rate of A_+ is $C_{20}A_+A_oN_o$. Here is the chance to reduce the ion loss rate drastically. Because $A_o \ll N_o$, an effect not possible in a pure gas is at hand.

We see that some N_+ and N_{2+} ions can contribute to A_+, but for the moment we ignore all but the lower emphasized reactions. In justification, we point out that both the production via metastables and the loss of A_+ will be

10

sensitive to the ratio A_o/N_o, but all the rest of the variations are insensitive to this ratio. Thus our plan is to explore this critical production loss chain critically. If the A_+ density is desirably high, we can add the effects of N_+ and N_{2+} later, because they will be relatively small. If the A_+ density is disappointingly low, we dismiss the whole sequence.

5. Simplified Penning Mixture Equations

The discussion of Section 4 is now turned into arithmetic. Equations 4, 6, 7 and 1 become respectively

$$0 = S_2 N_o - \frac{K_m N_m}{N_o \Lambda^2} - C_{15} N_m A_o - C_{13} N_m N_o - C_{14} N_m N_o^2, \tag{18}$$

$$0 = C_{15} N_m A_o - \frac{K_3 A_+}{N_o \Lambda^2} - C_{20} A_+ A_o N_o, \tag{19}$$

$$0 = C_{20} A_+ A_o N_o - C_{21} A_{2+} N_e - \frac{K_4 A_{2+}}{N_o \Lambda^2}, \tag{20}$$

$$0 = N_e - A_+ - A_{2+}. \tag{21}$$

Here we have neglected the atomic ion recombination C_{18} and C_{19}; and we have set $D = K/N_o$ for each species, as described in the sentences just before Eq.1. Equation 18 yields

$$N_m = \frac{S_2 N_o}{\frac{K_m}{N_o \Lambda^2} + C_{15} A_o + C_{13} N_o + C_{14} N_o^2} \tag{22}$$

trivially, hence from Eq. 19

$$A_+ = \frac{C_{15} S_2 (A_o N_o) N_o}{\left[\frac{K_3}{N_o \Lambda^2} + C_{20}(A_o N_o) \right] \left[\frac{K_m}{\Lambda^2} + C_{15}(A_o N_o) + C_{13} N_o^2 + C_{14} N_o^3 \right]}. \tag{23}$$

In obtaining Eq. 23, we have multiplied above and below by N_o, in order to express A_o only as part of terms $A_o N_o$. The purpose of this stratagem will be clear in a moment.

The remaining equations can in fact now be solved, yielding a quadratic form for N_e. It is

$$N_e^2 + N_e \left\{ \frac{K_4}{C_{21} N_o \Lambda^2} - A_+ \right\} - \frac{A_+}{C_{21}} \left\{ \frac{K_4}{N_o \Lambda^2} + C_{20} A_o N_o \right\} = 0, \tag{24}$$

where we must insert A_+ from Eq. 23.

11

While suitable for an elementary computer, Eq. 24 will not be very tractable analytically when we consider maximizing N_e with respect to both N_o and A_o. Thus we use the stratagem that led to Eqs. 14 - 16: if atomic ions are effectively blocked from converting to molecular ions, then Eq. 23 will represent N_e to a good approximation.

Our plan is to maximize Eq. 23 with respect to N_o and A_o as well as possible. To start the process, suppose for a moment that C_{13} and C_{14} were zero - that is, there is no metastable destruction by 2-body or 3-body processes; i.e., all N_m diffuse or convert to A_+. Equation 23 could then be written as

$$N_e = \frac{C_{15}S_2 x^2}{\left[\frac{K_3}{\Lambda^2} + C_{20}x\right] y \left[\frac{K_m}{\Lambda^2} + C_{15}y\right]} \tag{25}$$

where

$$x = A_o N_o^2$$
$$y = A_o N_o \tag{26}$$

The variables x and y are just as suitable for maximizing N_e as were A_o and N_o. Now we see from the form of Eq. 25 that there is no maximum. In fact, $N_e \longrightarrow \infty$, as $x \longrightarrow \infty$, $y \longrightarrow 0$, or as $N_o \longrightarrow \infty$, and $A_o \longrightarrow 0$ in a suitable manner. Note, however, that the physics prevents our setting A_o identically zero. This result is very different from the pure gas results of Section 3; the reason for this difference is important to us. Here, the ionic conversion rate is proportional to $A_o N_o$, not N_o^2 in this approximation. Thus we are at liberty to adjust N_o anyway we please, keeping $A_o N_o$ constant. In particular, we can increase N_o indefinitely, thus producing additional ionization $S_2 N_o$, and reducing diffusion to a negligible value.

It is evident that metastable destruction at high pressure upsets this picture, and we must reintroduce either C_{13} or C_{14}, or both, in order to recover reasonable physics. This single insertion causes formidable complications, because no separation into two separate maximizations can be found (as was done in Eq. 25). The best method of treating Eq. 23 exactly seems to be to maximize with respect to $A_o N_o$, and N_o. Setting $\partial A_+ / \partial (A_o N_o) = 0$ yields

$$(A_o N_o)^2 = \left[\frac{K_3}{N_o \Lambda^2 C_{15} C_{20}}\right] \left[\frac{K_m}{\Lambda^2} + C_{13}N_o^2 + C_{14}N_o^3\right]. \tag{27}$$

Note that Eq. 27, which gives the mixture ratio, predicts that this ratio will be a strong function of the density itself. Setting $\partial A_+ / \partial N_o = 0$ is reported to yield

$$A_o N_o = \frac{\frac{3 K_3 K_m}{\Lambda^2} + K_3 C_{13}N_o^2 + K_3 C_{14}N_o^3}{C_{13}C_{20}\Lambda^2 N_o^3 + 2C_{14}C_{20}\Lambda^2 N_o^4 - 2K_3 C_{15} - K_m C_{20}N_o} \tag{28}$$

Equation 28 does not seem useful to us, and has not even been checked. In

principle, the ideal N_o is determined by solving Eqs. 27 and 28, but the equation will be 11th order (if we have $C_{14} = 0$, it is 8th order).

We must use more physical reasoning to simplify the maximization problem. It will turn out that the metastable diffusion rate is small compared to metastable destruction. The reason is that in Eq. 23 we will end up by being close to a balance of A_+ diffusion and A_+ 3-body conversion (K_3 vs C_{20}). But the 3-body conversion is very unlikely compared to any 2-body collision process. Then on the supposition that K_3 and K_m are commensurate, and C_{15} or C_{13} are reasonable 2-body numbers, we must conclude that metastable diffusion will be small compared to other metastable disappearance terms.

One more fortuitous circumstance allows us to complete the calculation: $C_{14} \approx 0$ for the neon metastables in neon (see Section D). With these simplifications, Eq. 27 yields

$$N_o = \frac{K_3 \, C_{13}}{C_{15} C_{20} \Lambda^2 A_o^2} \qquad , \qquad (29)$$

In addition, Eq. 23 becomes remarkably simplified by inserting Eq. 29:

$$A_+ = \frac{S_2 \, K_3 \, C_{13}^2 \, A_o^2}{\Lambda^2 C_{15}^2 C_{20}^2 \left[A_o^3 + \dfrac{K_3 \, C_{13}^2}{\Lambda^2 C_{15}^2 C_{20}} \right]^2} \qquad . \qquad (30)$$

This is easily maximized to yield

$$A_o = \left[\frac{K_3 \, C_{13}^2}{2 \Lambda^2 C_{15}^2 C_{20}} \right]^{1/3} \qquad . \qquad (31)$$

Thus finally

$$N_o = \left[\frac{4 \, K_3 \, C_{15}}{\Lambda^2 C_{13} C_{20}} \right]^{1/3} \qquad , \qquad (32)$$

$$\frac{A_o}{N_o} = \frac{C_{13}}{2 C_{15}} \qquad , \qquad (33)$$

and

$$A_+(\approx N_e) = \frac{4 \, S_2}{9} \left[\frac{C_{15}^2 \, \Lambda^2}{4 K_3 C_{13}^2 C_{20}^2} \right]^{1/3} \qquad . \qquad (34)$$

As an example, let us take the following values. (See Section D for a full discussion of the appropriate values to use.)

$$K_3 \approx 7.2 \times 10^{18} \text{ cm}^{-1} \text{ sec}^{-1}$$
$$C_{13} = 3.6 \times 10^{-15} \text{ cm}^3 \text{ sec}^{-1}$$
$$C_{15} = 1.8 \times 10^{-11} \text{ cm}^3 \text{ sec}^{-1}$$
$$C_{20} = 25 \times 10^{-32} \text{ cm}^6 \text{ sec}^{-1}$$
$$S_2 = 1.35 \times 10^{-3} \text{ sec}^{-1}$$

We take $\Lambda = 0.1$ cm, and find

$$\frac{A_o}{N_o} = 1 \times 10^{-4}$$

$$N_o = 3.9 \times 10^{18} \text{ cm}^{-3} \; (\approx 110 \text{ Torr})$$

$$N_e = 3.1 \times 10^{12} \text{ cm}^{-3}$$

6. Effect of Other Processes

The heavy dashed sequence in Fig. 3 represents only part of the story. We now put in the remainder of the important effects.

(a) N_+ production and density.

For N_+, we shall use

$$S_o = 2.6 \times 10^{-3}$$
$$C_4 = 8 \times 10^{-32}$$
$$K_1 = 5.52 \times 10^{18} \text{ cm}^{-1} \text{ sec}^{-1}$$

To first order, Eq. 14 should apply, whence at $N_o = 3.9 \times 10^{18} \text{ cm}^{-3}$, we find $N_+ \approx 8 \times 10^9 \text{ cm}^{-3}$. This is a small perturbation to the various densities. Nearly all the N_+ ions disappear by converting to N_{2+} via process C_4.

(b) $N_+ \longrightarrow A_+$ charge transfer (C_6)

We might have significant additional source of A_+ via process C_6. We wish to compute the ratio

$$\frac{C_6 N_+ A_o}{C_{15} N_m A_o} = \frac{C_6 N_+}{C_{15} N_m}$$

For these approximate conditions, we have

$$C_6 N_+ / C_{15} N_m = \left(\frac{C_6 S_o N_o}{C_4 N_o^2} \right) \Big/ \frac{C_{15} S_2 N_o}{2 C_{13} N_o}$$

$$= \frac{2 C_6 S_o C_{13}}{C_4 S_2 C_{15} N_o}$$

14

Using $C_6 = 3.9 \times 10^{-13}$ cm^3 sec^{-1}, we find this ratio to be $\approx 10^{-3}$. Thus 2-body charge transfer $N_+ \longrightarrow A_+$ is not important in this instance. Note, however, that the calculation is made here for specific conditions and the factor 10^{-3} will not always apply. At lower pressure, fewer N_+ ions disappear by process C_4; hence more will disappear by charge transfer C_6 (if diffusion does not take over meanwhile). On the other hand, the actual ratio is so small (10^{-3}) that we will believe pro tem that process C_6 will never be important in neon-argon.

(c) N_{2+} density.

Here we can compute N_{2+} as a balance between production $S_o N_o \approx C_4 N_c{}^2 N_+$ and recombination $C_{16} N_{2+} N_e$. For neon molecular ion dissociative recombination, $C_{16} = 2.2 \times 10^{-7}$ cm^3 sec^{-1}, and we take $N_e = 3.1 \times 10^{12}$ from the previous calculation of A_+. Therefore

$$N_{2+} \approx \frac{S_o N_o}{C_{16} N_e} \approx 10^{10} \text{ cm}^{-3}$$

for the density $N_o = 3.9 \times 10^{18}$ cm^{-3}, and this is negligible.

(d) A_{2+} density.

We need not even calculate. The rate of formation of A_{2+} and N_{2+} are comparable, and $C_{21} > C_{16}$. Thus A_{2+} is negligible.

(e) Recombination of A_+.

We take the following numbers for C_{18} and C_{19}, (see Section D).

$$C_{18} \approx 4 \times 10^{-12} \text{ cm}^3 \text{ sec}^{-1}$$

$$C_{19} = 2.7 \times 10^{-30}$$

We wish to find the ratio

$$\frac{(C_{18} + C_{19} N_o) N_+ N_e}{C_{20} N_+ N_o A_o}$$

Note that at $N_o = 3.9 \times 10^{18}$, the 2-body radiative and 3-body Thompson recombination rates are about equal. Thus by chance we are in a reasonable pressure regime for non-excessive recombination loss. For a density $N_+ = N_e = 3.1 \times 10^{12}$, we find this ratio ≈ 0.1. Thus this process is small also.

(f) N_x effects.

Since N_x contributes only to N_{2+}, an already negligible density, we neglect all effects of N_x.

(g) $N_m{}^2$ destruction.

We find $N_m \approx 10^{10} - 10^{11}$ cm^{-3}. For a metastable atom to find another metastable before finding an argon atom would require the cross section corresponding to C_{12} to be $\approx 10^{-12}$ cm^{-2}. We have no sure data on this number at the moment, but believe that it cannot be that large. Thus we dismiss the process indicated by C_{12}.

7. CONCLUSION

Physically, we have maximized the electron density N_e in a Penning gas. At these conditions on majority gas density N_o and minority gas density A_o that give maximum N_e, we find:

(a) Metastables N_m are destroyed by conversion to A^+ and by non-profitable destruction in the gas, in about equal proportions.

(b) The ions are almost entirely A_+, which are lost via diffusion and 3-body conversion to A_{2+} (which disappear forthwith); these two processes occur with roughly comparable frequency.

(c) The ratio (N_m conversion to A_+)/(N_m useless destruction) is exactly equal to the ratio (A_+ diffusion loss)/(A_+ 3-body conversion loss) at the optimum conditions. This fact can be seen by inserting Eqs. 31 and 32 into Eq. 23.

Note that the recombination terms C_{18} and C_{19} are presently negligible (≈ 0.1) compared with other A_+ loss terms, and N_e is proportional to S_2. This will not continue indefinitely. At a flux about 10 times higher ($\approx 10^{14}$ neutrons/cm^2sec) the recombination terms will be important, and N_e will tend toward a $S^{1/2}$ dependence. The corresponding density will substantially exceed 10^{13} cm^{-3} however.

SECTION C

BLANK PAGE

SECTION C

COMPUTER SOLUTIONS TO THE REACTOR KINETICS EQUATIONS

ABSTRACT

The seven simultaneous equations which describe the reaction kinetics in a plasma generated by fission fragment ionization of a Penning-type gas mixture were solved on the IBM digital computer. The results of the first parametric studies on the effects of pressure, concentration of the minority gas species and the electrode spacing are discussed. The first runs confirmed the approximate solutions obtained analytically in the previous Section B. Using the full set of equations in the code it was found that in the recombination of the molecular neon ions if an appreciable fraction ($\sim$ .5) produces the metastable states of neon, these in turn increase the production rate of argon ions and significantly increase the electron number density ($\sim$ x 2). Reducing the electrode spacing from .33 to .051 cm increased the diffusion losses and greatly decreased the electron number density. This result showed that further theoretical work must be done before this tool can be used to optimize the performance of a thermionic energy converter.

CONTENTS

BLANK PAGE

INTRODUCTION

The equations governing the reaction kinetics of the fission fragment generated plasma have been discussed in detail by Professor D. J. Rose in the previous Section B. The equations are summarized in Table 1 and the reaction diagram is reproduced in Fig. 1. In that study a solution was found analytically for the case of pure argon at the intermediate pressure where a maximum occurs in the electron number density versus pressure (~ 8 torr). A second solution was found analytically for the Penning mixture of neon-argon again for the case where a maximum occurs for the electron number density versus pressure (~ 110 torr) and also at the optimum mixture of neon-argon ($A_o/N_o = 10^{-4}$). In both of these solutions a number of simplifying assumptions were made to make the equations tractable. To obtain the second solution only the production of argon ions from the neon metastables which were produced directly from the fission fragments ($S_2 N_o$) were considered. The presence of the neon ions (N_+, N_{2+}) was neglected as well as the production of neon metastable states from the recombination of those neon ions ($C_{11} C_{16} N_{2+} N_e$). The effect of including this latter term was not discussed but it would increase the source of A_+ ions and could significantly increase the electron number density for $0.1 \gtrsim C_{11} \gtrsim 1.0$. This possibility and the future use for the A-Cs system pointed up the need for a solution to the complete set of equations which could only be done economically on the IBM computer. Consequently, a computer code was written and this report summarizes the results of the initial studies with this code.

TABLE 1

Equations for Particle Density Time Derivatives *

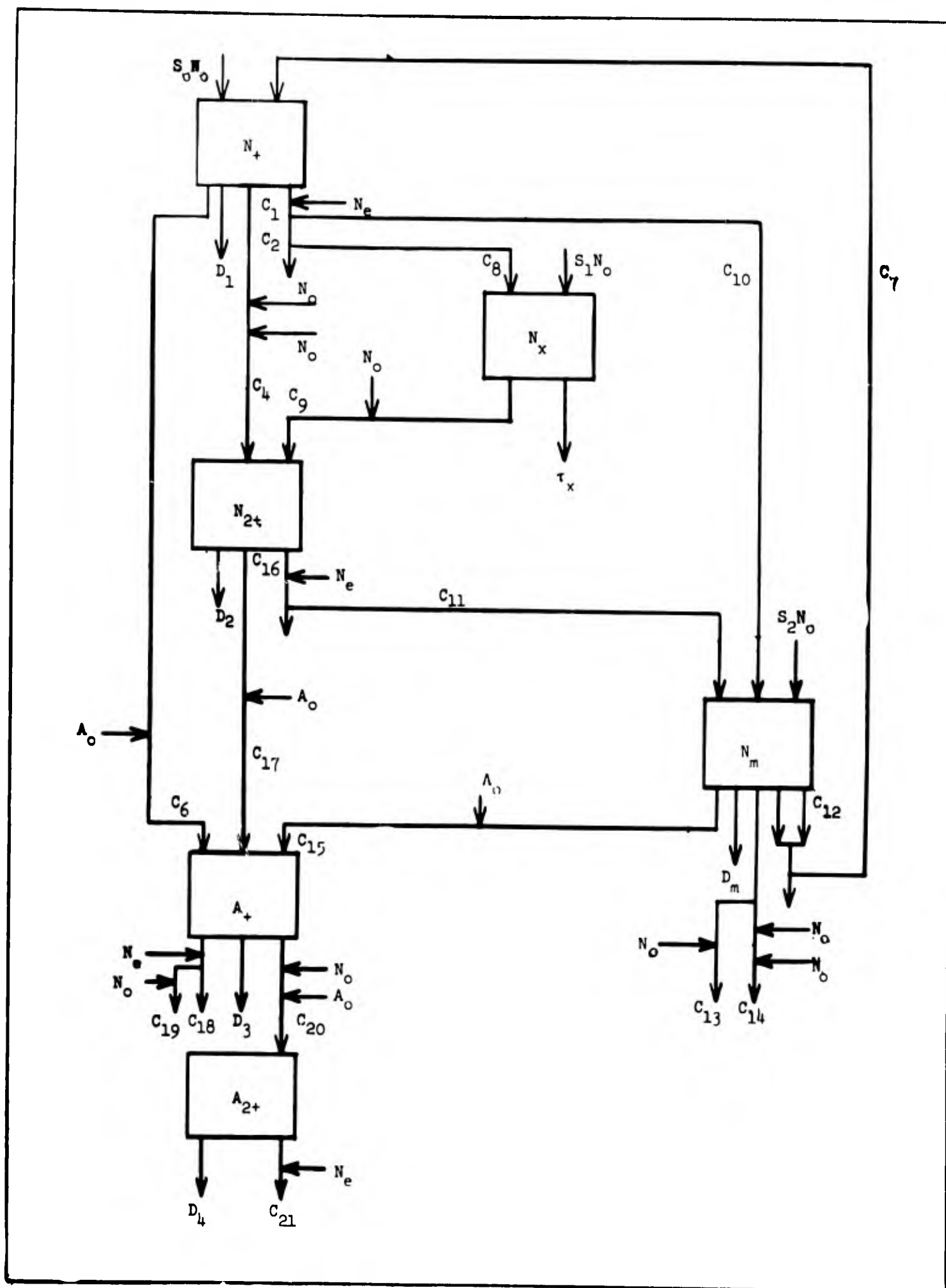| Time Der. From	Direct Flux	Diff.	Recombination	3-Body Mol.Ion Formation	2-Body Ch. Exch.	Meta-Meta Coll.	Radiation	Mol.Ion Formation via N_x	Meta Destruct via N_o	Penning	Eq. No.
$\dfrac{\partial N_+}{\partial t} = S_oN_o$		$-D_1\nabla^2N_+$	$-[C_1+C_2N_o+C_3N_e]N_+N_e$	$-C_4N_+N_o^2$ $-C_5N_+N_oA_o$	$-C_6N_+A_o$						(2)
$\dfrac{\partial N_x}{\partial t} = S_1N_o$			$+C_8[C_1+C_2N_o]N_+N_e$				$-N_x/\tau$	$-C_9N_xN_o$			(3)
$\dfrac{\partial N_m}{\partial t} = S_2N_o$		$-D_m\nabla^2N_m$	$+C_{10}[C_1+C_2N_o]N_+N_e$ $+C_{11}C_{16}N_{2+}N_e$			$+C_7N_m^2$		$+C_9N_xN_o$	$-C_{13}N_oN_m$ $-C_{14}N_o^2N_m$	$-C_{15}N_mA_o$	(4)
$\dfrac{\partial N_{2+}}{\partial t} =$		$-D_2\nabla^2N_{2+}$	$-C_{16}N_{2+}N_e$	$+C_4N_+N_o^2$	$-C_{17}N_{2+}A_o$	$-C_{12}N_m^2$					(5)
$\dfrac{\partial A_+}{\partial t} =$		$-D_3\nabla^2A_+$	$-(C_{18}+C_{19}N_o)N_eA_+$	$-C_{20}A_+A_oN_o$	$+C_6N_+A_o$ $+C_{17}N_{2+}A_o$					$+C_{15}N_mA_o$	(6)
$\dfrac{\partial A_{2+}}{\partial t} =$		$-D_4\nabla^2A_{2+}$	$-C_{21}A_{2+}N_e$	$+C_{20}A_+A_oN_o$							(7)

2

Figure 1 - Reaction diagram corresponding to Eqs. 2 - 7, for production
and loss of ions N_+, N_{2+}, A_+, and A_{2+}.

3

Computer Code

A problem statement was submitted to the GM Computer Technology Department for the simultaneous solution of the seven non-linear algebraic equations. The differential operator, ∇^2, was replaced by $1/\Lambda^2$, where Λ is the diffusion length and the diffusion coefficient, D_i, was replaced by K_i/N_o.

There was no FORTRAN-II subroutine available to operate in the GM Research Laboratories F-system but a new FORTRAN-IV subroutine developed at Purdue was located and this subroutine was operated on the new IBM "IBSYS" system. W. Butterfield of the Computer Technology Department wrote a short control program for this subroutine and the program was successful on the first test problem.

Conversion Coefficients for Rate Processes

The values of the conversion coefficients used in these first parameter studies with the "Reaction Rate Code" are listed in Table 2. Some of these values were obtained from the literature and some were computed. They are discussed in detail in Section D.

The source term coefficient $S_o(N_+)$ was obtained as outlined in Section A using the fission fragment ionization code for neon at 240 torr and at a neutron flux of $\phi = 1 \times 10^{13}$ cm^{-2} sec^{-1} (P = 2 MW). The maximum value of S at the surface of the uranium was used. The source term coefficient for the neon metastable production, $S_2(N_m)$, was obtained from the above value and the similar source rate value from a neon-argon code for the fission fragment ionization of neon: argon (1000:1) at the same pressure and at the same flux.

The complete equation for N_x, the excited states of the majority gas species, is built into the code but the source term S_1 was not readily determined. S_1, and also N_x, was set equal to zero in the present solutions. The justification for ignoring N_x is outlined in Section D.

Parametric Studies with Code

The parametric studies reported here are not complete but rather were meant to check out the code and also the values calculated in Section B. Many of the simplifications made in Section B are also contained here but only because some of the coefficients are presently not known. Only in the case of the production of neon metastables from the recombination of the neon molecular ions $(C_{11}C_{16}N_{2+}N_e)$ was it thought that the addition of a neglected term could appreciably affect the electron density.

A total of 93 runs (solutions to the equations) have been run to date. The results are presented in graphical form in the following sections and the complete solutions to six of the runs are given in Table 3.

TABLE 2

Conversion Coefficients for Ne:A Studies*
(N = Neon   A = Argon)

Source Term Coefficients

$S_o(N_+)$ = 2.6 x 10^{-3} cm^{-3} sec^{-1} (unit density)$^{-1}$

$S_1(N_x)$ = 0

$S_2(N_m)$ = 1.35 x 10^{-3} cm^{-3} sec^{-1} (unit density)$^{-1}$

Reaction Coefficients

C_1 = 0

C_2 = 0

C_3 = 0

C_4 = 8 x 10^{-32} cm^6 sec^{-1}

C_5 = 0

C_6 = 3.9 x 10^{-13} cm^3 sec^{-1}

C_7 = 0

C_8 = 0

C_9 = 0

C_{10} = 0

C_{11} = (Varied) 0.0, 0.5, 1.0

C_{12} = 0

C_{13} = 3.6 x 10^{-15} cm^3 sec^{-1}

C_{14} = 0

C_{15} = 1.8 x 10^{-11} cm^3 sec^{-1}

C_{16} = 2.2 x 10^{-7} cm^3 sec^{-1}

C_{17} = 3.9 x 10^{-13} cm^3 sec^{-1}

C_{18} = 4 x 10^{-12} cm^3 sec^{-1}

C_{19} = 2.4 x 10^{-30} cm^6 sec^{-1}

C_{20} = 2.5 x 10^{-31} cm^6 sec^{-1}

C_{21} = 6.5 x 10^{-7} cm^3 sec^{-1}

Diffusion Coefficients

K_1 = 5.52 x 10^{18} cm^{-1} sec^{-1}

K_m = 5.5 x 10^{18} cm^{-1} sec^{-1}

K_2 = 8.74 x 10^{18} cm^{-1} sec^{-1}

K_3 = 7.2 x 10^{18} cm^{-1} sec^{-1}

K_4 = 6.8 x 10^{18} cm^{-1} sec^{-1}

Geometry Coefficients

Λ = d/π where d = electrode spacing

Λ = 0.1 for most of these studies

Average Lifetime of Excited States

τ_x = 1 x 10^{-6} sec (note that all source terms of N_x = 0)

*A more detailed evaluation of the conversion coefficients is to be found in Section D. Those that were not equal to zero were not known at the time of writing this Section. However the influence of finite values for them has been checked and found to be insignificant in this calculation.

TABLE 3

Selected Code Solutions to Kinetic Equations
(Near Maxima in Curves of N_e vs N_o)

Run No.	N_o x 10^{18}	A_o/N_o	C_{11}	Λ	N_e x 10^{-12}	N_+ x 10^{-10}	N_{2+} x 10^{-10}	N_m x 10^{-12}	A_+ x 10^{-12}	A_{2+} x 10^{-8}
10.1	3.9	1 x 10^{-4}	0.0	0.1	2.918	.8331	1.578	.2483	2.893	5.800
11.3	3.9	1 x 10^{-4}	0.5	0.1	5.393	.8331	.8542	.4873	3.315	5.831
14.4	4.0	1 x 10^{-4}	1.0	0.1	7.664	.8123	.6165	.7266	7.649	6.142
13.2	2.0	1 x 10^{-3}	0.5	0.1	3.192	1.620	.7367	.1216	3.167	15.26
17.7	8.0	1 x 10^{-5}	0.5	0.1	3.154	.4062	2.997	.6994	3.120	2.435
19.9	14.0	1 x 10^{-4}	0.5	.0162	1.849	.2321	8.882	.4795	1.751	71.27

Effect of Pressure

The first parameter study made with the code was the effect of pressure on the electron number density as shown in Fig. 2. The lower curve for C_{11} = 0 represents the conditions studied in Section B and the maximum in the curve that was predicted by Professor Rose is very close, indeed.

Also included are similar curves for C_{11} = 0.5 and C_{11} = 1.0. The curve for C_{11} = 0.5 represents the additional source of neon metastable states equal to 1/2 the neon molecular ion recombination rate. The curve for C_{11} = 1.0 represents the limiting case where all of the neon molecular ion recombination rate goes to produce neon metastable states. As shown by the curves, the presence of this source of neon metastable states would greatly enhance the electron number density. Very little is known about this reaction so that a reasonable value of C_{11} is very difficult to come by. However, with our new understanding of the ion generation rate in neon and neon:argon mixtures and the forthcoming inpile microwave experiments to measure the electron number density directly, it may be possible to infer a value of this quantity since the rest of the important reaction kinetic constants are reasonably well known.

The code solution also yields values of all the other dependent variables N_+, N_{2+}, N_m, N_x, A_+ and A_{2+} and values of these variables are summarized in Table 3 for selected runs.

Effect of the Concentration of the Minor Species, Argon

The second maximum predicted in Section B was that the electron number density would peak at the ratio of argon/neon of A_o/N_o = 1 x 10^{-4}. An exhaustive variation of this variable at various pressures (N_o) was not made but three series of runs of N_e versus N_o were made for A_o/N_o = 1 x 10^{-3}, A_o/N_o = 1 x 10^{-4}, and A_o/N_o = 1 x 10^{-5}. The curves are presented in Fig. 3 for the case of C_{11} = 0.5 and the curve for A_o/N_o = 10^{-4} does indeed peak at the highest electron number density. The peak for the A_o/N_o = 10^{-3} curve has been shifted to 50 Torr while the peak for the A_o/N_o = 10^{-5} curve has been shifted to about 240 Torr.
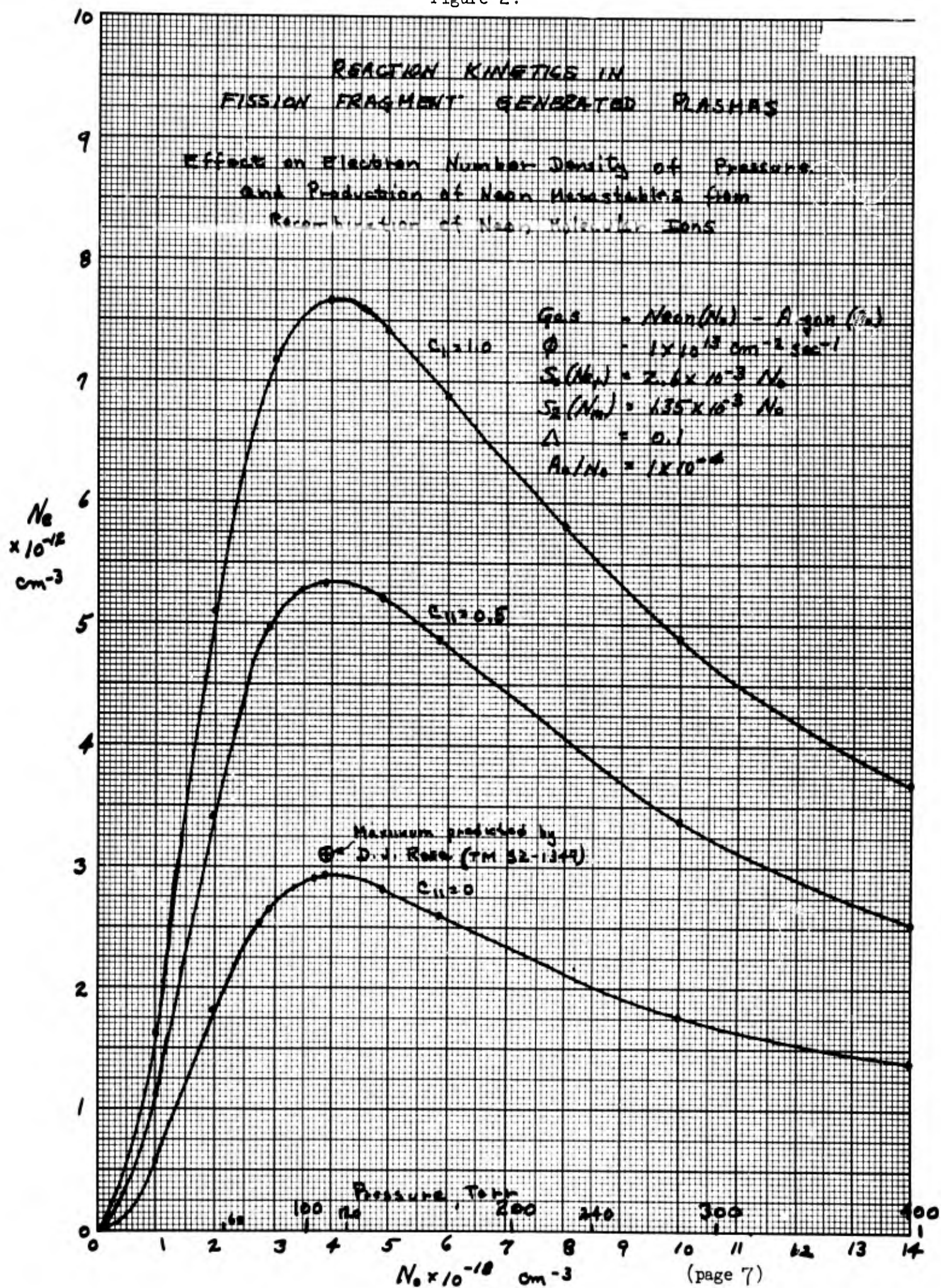
Figure 2.

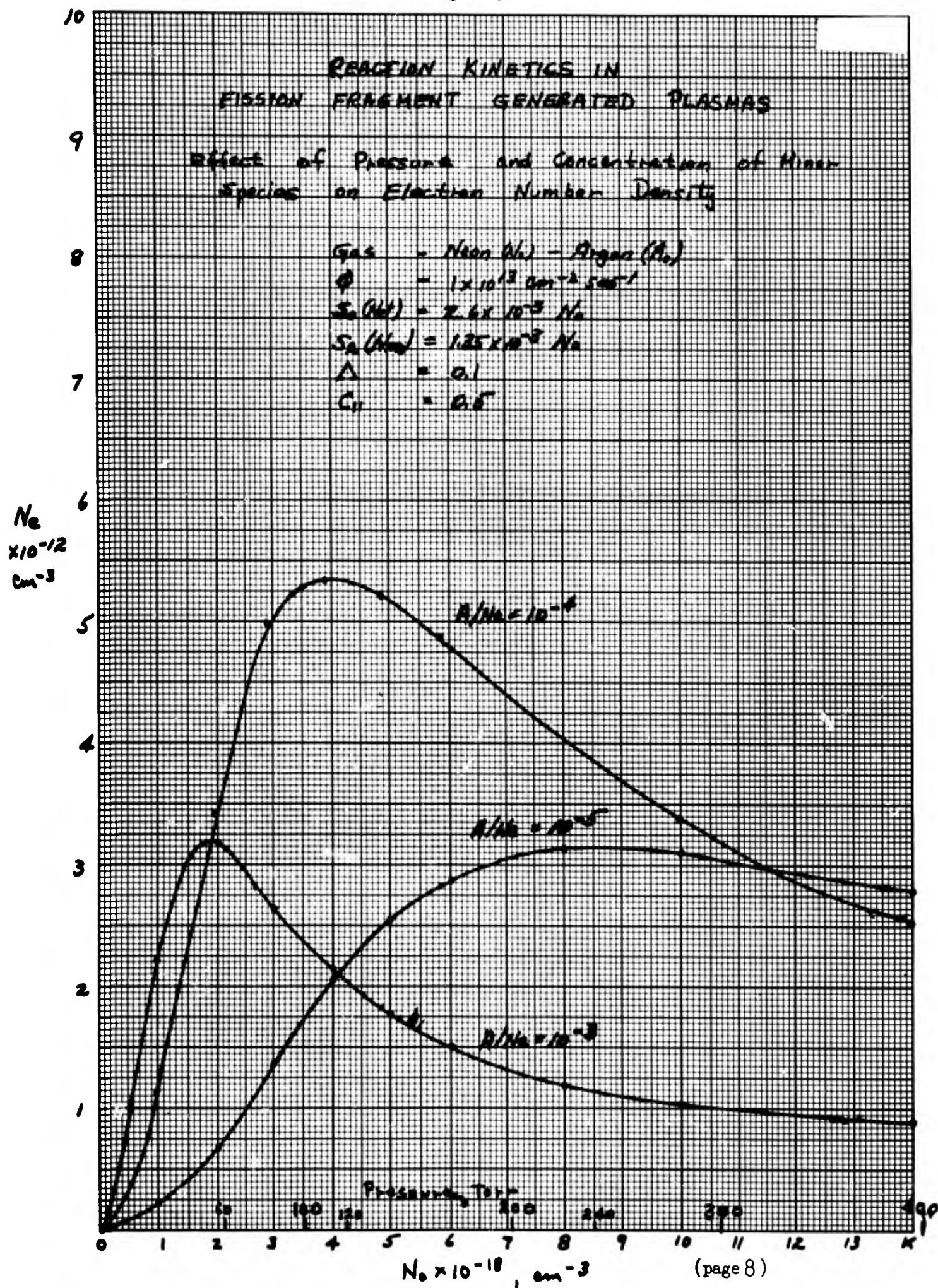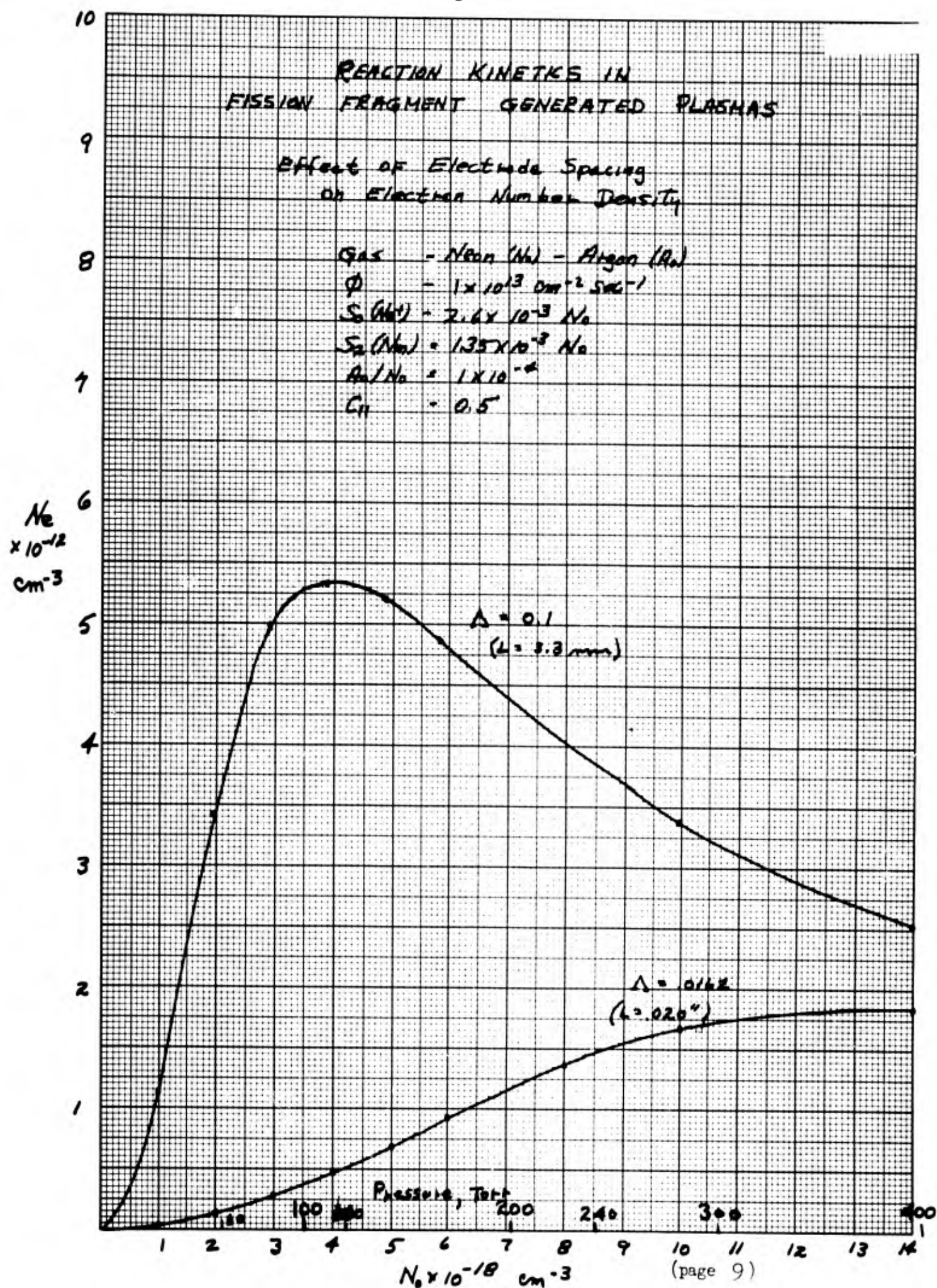REACTION KINETICS IN
FISSION FRAGMENT GENERATED PLASMAS

Effect on Electron Number Density of Pressure
and Production of Neon Metastables from
Recombination of Neon Molecular Ions

(page 7)

Figure 3.

REACTION KINETICS IN
FISSION FRAGMENT GENERATED PLASMAS

Effect of Pressure and Concentration of Minor
Species on Electron Number Density

Gas = Neon (Ne) — Argon (Ar)
ϕ = 1×10^{13} cm^{-2} sec^{-1}
$S_a(Ne^+)$ = 2.6×10^{-3} N_o
$S_a(Ne_2^+)$ = 1.25×10^{-3} N_o
Δ = 0.1
C_{it} = 0.5

$N_e \times 10^{-12}$ cm^{-3}

$A/N_o = 10^{-4}$

$A/N_o = 10^{-5}$

$A/N_o = 10^{-3}$

Pressure, Torr

$N_o \times 10^{-18}$, cm^{-3}

(page 8)

Figure 4.

REACTION KINETICS IN
FISSION FRAGMENT GENERATED PLASMAS

Effect of Electrode Spacing
on Electron Number Density

Gas   - Neon (Ne) - Argon (Ar)
ϕ - 1×10^{13} cm^{-2} sec^{-1}
S_o (Ne) - 2.6×10^{-3} N_o
S_o (Ar) - 135×10^{-3} N_o
A_r/N_o - 1×10^{-4}
C_n - 0.5

$\Lambda = 0.1$
($L = 3.3$ mm)

$\Lambda = 0.042$
($L = .020''$)

$N_e \times 10^{-12}$ cm^{-3}

Pressure, Torr

$N_o \times 10^{-18}$ cm^{-3}

(page 9)

Effect of Electrode Spacing

As pointed out previously the decrease in electron number density with decreasing pressure (at low pressures) is due to the increased diffusion losses of both the ions and metastable states ($D_i = K_i/N_0$). Now the diffusion loss ($D_i N_i/\Lambda^2$) rate also depends strongly on the electrode spacing ($\Lambda = d/\pi$) so that it was decided to also make a preliminary study of this variable particularly since the electron transport problem for an energy converter implies minimizing the plasma resistance and therefore the spacing.

As a first test the spacing was reduced to what is considered a lower bound from construction considerations of .020 in. or Λ = .0162. The curve of N_e vs N_0 for this reduced Λ and C_{11} = 0.5 is shown in Fig. 4 together with the curve for Λ = 0.1 for comparison. As can be seen N_e is greatly reduced and the maximum is shifted from 110 Torr to a value greater than 400 Torr. These data confirm that the optimization on pressure, A_0/N_0, and geometry must also include the effects on plasma resistivity and converter performance.

SECTION D

SECTION D

PRODUCTION, DIFFUSION AND CONVERSION RATES OF IONS, METASTABLE AND EXCITED STATES IN PENNING-TYPE NEON-ARGON PLASMAS

ABSTRACT

A detailed study of the reaction kinetics of a fission fragment generated plasma requires knowledge of about 30 reaction rates if the plasma is created using a Penning-type gas mixture. These reaction rates represent such processes as diffusion, recombination, molecular-ion formation, charge exchange, volume ionization and destruction in the gas of various ionic, excited and metastable states. It is shown that, with few exceptions, these reaction rates are directly known, may be readily extracted from the literature or may be estimated, for the neon-argon mixture. The notable exception for which it has not been found possible to give an estimate, is the production rate of metastable states from the dissociative recombination of a molecular ion and electron. After discussion of all the reaction rates, the data are collected at the end in tabular form suitable for reference.

i

CONTENTS

BLANK PAGE

OBJECT

The purpose of this work was to make a compilation of the fundamental reaction rates between ions, excited states and neutral atoms in a neon-argon plasma.

SUMMARY

Despite the large number of reactions which can occur simultaneously in a neon/argon plasma, sufficient basic data have been compiled for worthwhile computational studies to be made of the reaction kinetics of this system.

I. INTRODUCTION

Dense plasmas are of interest in the field of thermionic energy conversion because such plasmas can be used to neutralize the retarding space charge of the thermionic electrons. The number density in any active plasma is a function of both the ion generation rate and the various ion loss rates, so that in order to achieve maximum number density it is necessary to study in detail the dependence of the ion generation and loss rates on such parameters as gas species, gas density and electrode configuration. Very recently such a study of reaction kinetics in a fission fragment generated plasma was initiated by Professor D. J. Rose [1] and particle density equations were formulated for a Penning-type gas mixture which are applicable to a neon-argon plasma of density $N_e \sim 10^{12}$ electrons cm^{-3}. The purpose of the present work was to make a compilation of the various reaction rate coefficients in neon-argon which were needed as input data for these equations. Table I summarizes the reactions proposed by Professor Rose and will be continually referred to in this report.

II. GENERATION RATE OF ATOMIC IONS
AND EXCITED STATES BY FISSION FRAGMENTS

Since the concentration of neutral neon atoms N_0 in the Penning mixture is much larger than that of the argon atoms A_0, the fission fragments in passing through the gas mainly generate atomic neon ions N_+, metastable excited neon states N_m, and excited neon states N_x, that are not metastable. As a result of excitation transfer and the imprisonment of resonance radiation, some of the N_x states decay into N_m states, but the net effect of such transitions in the steady-state will be to increase the value of the metastable generation rate S_2. The remaining N_x states will either (i) undergo radiative transitions emitting photons which escape from the plasma or (ii) produce N_{2+} molecular ions in two body collisions with N_0 (Hornbeck-Molnar process[2]) provided the N_x state has an energy lying within the range[3] ~ 20.6 ev to E_i ($= 21.6$ ev) where E_i is the first ionization energy for neon. The

1

contribution of process(ii) to the total ion generation rate, however, cannot be large for the following reasons. Studies by Platzman[4] and Utterback and Miller[5] on α-particle and fission-fragment ionization of noble gases indicate that the value of $(S_1 + S_2)/S_0$ is ~ 0.5; i.e. the total production rate of all excited states is about one-half the ion production rate. Furthermore, much of the excitation energy will be distributed among excited states having energy $\lesssim 20.6$ ev and which are thus incapable of yielding molecular ions via the Hornbeck-Molnar process. The production rate of metastable states S_2 arising from fission fragment excitation is therefore taken to be much larger than the production rate S_1 of highly excited states which lead to molecular ion formation, i.e. $S_2 - S_1 \approx S_2$.

The value of S_2 may now be determined from values of S_0 computed for pure neon and for a neon-argon mixture (0.1% Ar) under the same conditions. At a pressure of 240 Torr, $S_0(N_e).N_0 = 2.22 \times 10^{16}$ cm^{-3} sec^{-1} immediately adjacent to the uranium surface for a neutron flux value of $\phi = 0.99 \times 10^{13}$ cm^{-2} sec^{-1}. For the same values of pressure and neutron flux, the total ion generation rate for the neon-argon mixture is $S_0(NeAr).N_0 = 3.13 \times 10^{16}$ cm^{-3} sec^{-1}. Neglecting metastable-metastable collisions, (the density of metastable states is negligible compared with the density of neutral atoms), and considering the sheath above the uranium, where recombination of ions does not occur and cannot thus contribute to metastable production, the conservation equation for metastable states is

$$S_2 N_o = - D_m \nabla^2 N_m + \nu_{eff} N_o N_m + N_m A_o q_i \bar{v}$$

$$\simeq \frac{D_m N_m}{\Lambda^2} + \nu_{eff} N_o N_m + N_m A_o q_i \bar{v}. \tag{1}$$

Replacing ∇^2 by $- 1/\Lambda^2$, the reciprocal squared of the diffusion length, is valid only if diffusion loss dominates. However if the diffusion loss is small compared with the other loss terms, then its exact value is of no consequence in the above equation. ν_{eff} (3.6×10^{-15} cm^3 sec^{-1}) is an effective 2-body destruction frequency for neon metastable states, q_i (2.5×10^{-16} cm^2) is the cross-section for ionization of argon by a neon metastable and $\bar{v}$ (6.9×10^4 cm sec^{-1}) is the average velocity of approach of these two particles; $D_m = 0.65$ cm^2 sec^{-1} for $N_o = 8.5 \times 10^{18}$ cm^{-3}, $\Lambda^2 = 9 \times 10^{-3}$ cm^2 and $A_o = 8.5 \times 10^{15}$ cm^{-3}. All these numerical values are discussed in detail below. Substituting the numerical values in Eq.(1) yields

$$S_2 N_o \simeq 72 N_m + 3.1 \times 10^4 N_m + 1.5 \times 10^5 N_m$$

$$= 1.8 \times 10^5 N_m. \tag{2}$$

The ion generation rate in neon-argon consists of the ion generation rate in pure neon plus the generation rate of argon ions resulting from collisions of neutral argon atoms with neon metastable states, i.e.

$$\Gamma_0(NeAr) \cdot N_o = S_0(Ne) \cdot N_o + N_m A_o q_i \bar{v}$$

$$(3.13 - 2.22) \times 10^{16} = 1.5 \times 10^5 N_m$$

$$\therefore N_m = 6.1 \times 10^{10} \text{ cm}^{-3} \qquad\qquad (3)$$

Using Eqs. (2) and (3), the generation rate of neon metastable states is found to be

$$S_2 = \frac{(1.8 \times 10^5)(6.1 \times 10^{10})}{8.5 \times 10^{18}}$$

$$= 1.3 \times 10^{-3} \text{ sec}^{-1}$$

III. DIFFUSION COEFFICIENTS FOR
METASTABLES, ATOMIC AND MOLECULAR IONS

The ambipolar diffusion coefficients D_a for Ne^+, Ne_2^+, Ar^+ and Ar_2^+ in neon at 300°K are determined from measurements of ion mobility μ_o^+ (at standard condition of 273°K and 760 Torr) using the following relationships:

$$\frac{D^+}{\mu_o^+} = \frac{kT^+}{e} = .026 \text{ ev for } T^+ = 300°K, \text{ and}$$

$$D_a = 2D^+ \text{ for thermal equilibrium } T^+ = T^-.$$

The ambipolar diffusion coefficient at unit atom density, K_a, is defined by $K_a = n_o D_a$ where $n_o (2.69 \times 10^{19} \text{ cm}^{-3})$ is the number density of atoms at 760 Torr and 273°K. Therefore K_a is given by

$$K_a = 2 \times .026 \times 2.69 \times 10^{19} \mu_o^+ = 1.4 \times 10^{18} \mu_o^+ \text{ cm}^{-1} \text{ sec}^{-1}$$

$$\text{(for } \mu_o^+ \text{ in cm}^2 \text{ v}^{-1} \text{ sec}^{-1}) \qquad (4)$$

$\underline{K_{1,a}(Ne^+) \text{ in neon}}$

$$\mu_o(Ne^+) = 4.1 \text{ cm}^2 (v \cdot sec)^{-1} \text{ from the work of Oskam and Mit-}$$
$$\text{telstadt}[6] \text{ and McDaniel}[7].$$

Therefore using Eq. (4), $K_{1,a}$ is given by

$$K_{1,a} = 5.7 \times 10^{18} \text{ cm}^{-1} \text{ sec}^{-1}$$

TABLE 1

Equations for Particle Density Time Derivatives

Time Der.	From Direct Flux	Diff.	Recombination	3-Body Mol.Ion Formation	2-Body Ch. Exch.	Meta-Meta Coll.	Radiation	Mol.Ion Formation via N_x	Meta Destruct via N_o	Penning
$\dfrac{\partial N_+}{\partial t} =$	$S_o N_o$	$D_1\nabla^2 N_+$	$-\left[C_1+C_2N_o+C_3N_e\right]N_+N_e$	$-C_4N_+N_o^2$ $-C_5N_+N_oA_o$	$-C_6N_+A_o$	$+C_7N_m^2$				
$\dfrac{\partial N_x}{\partial t} =$	$S_1 N_o$		$+C_8\left[C_1+C_2N_o\right]N_+N_e$				$-N_x/\tau_x$	$-C_9N_xN_o$		
$\dfrac{\partial N_m}{\partial t} =$	$S_2 N_o$	$D_m\nabla^2 N_m$	$+C_{10}\left[C_1+C_2N_o\right]N_+N_e$ $+C_{11}C_{16}N_{2+}N_e$			$-C_{12}N_m^2$		$+C_9N_xN_o$	$-C_{13}N_oN_m$ $-C_{14}N_o^2N_m$	$-C_{15}N_mA_o$
$\dfrac{\partial N_{2+}}{\partial t} =$		$D_2\nabla^2 N_{2+}$	$-C_{16}N_{2+}N_e$	$+C_4N_+N_o^2$	$-C_{17}N_{2+}A_o$					
$\dfrac{\partial A_+}{\partial t} =$		$D_3\nabla^2 A_+$	$-(C_{18}+C_{19}N_o)N_eA_+$	$-C_{20}A_+A_oN_o$	$+C_6N_+A_o$ $+C_{17}N_{2+}A_o$					
$\dfrac{\partial A_{2+}}{\partial t} =$		$D_4\nabla^2 A_{2+}$	$-C_{21}A_{2+}N_e$	$+C_{20}A_+A_oN_o$						$+C_{15}N_mA_o$

$\underline{K_{2,a}(Ne_2^+) \text{ in neon}}$

$$\mu_0(Ne_2^+) = 6.5 \text{ cm}^2(\text{v} \cdot \text{sec})^{-1} \text{ from Oskam and Mittelstadt}[6]$$
$$\text{and McDaniel}[7]$$

$$\therefore K_{2,a} = 9.1 \times 10^{13} \text{ cm}^{-1} \text{ sec}^{-1}$$

$\underline{K_{3,a}(Ar^+) \text{ in neon}}$

The value of $\mu_0(Ar^+)$ in neon $= 7.4 \text{ cm}^2(\text{v} \cdot \text{sec})^{-1}$ is taken from the data of Chanin and Biondi[8,9] showing mobility as a function of ion mass in neon. Primarily Chanin and Biondi determined the mobility of Hg^+ ions in neon, but the results are in agreement with the extrapolation of mobility versus mass number curves obtained for the alkali ions in the noble gas by Tyndall.[10] These data are considered appropriate for $\mu_0(Ar^+)$ in neon since resonant charge transfer effects (important for an atomic ion diffusing in its parent atomic gas) are absent.

$$\therefore K_{3,a} = 1.0 \times 10^{19} \text{ cm}^{-1} \text{ sec}^{-1}$$

$\underline{K_{4,a}(Ar_2^+) \text{ in neon}}$

$$\mu_0(Ar_2^+) \text{ in neon} = 6.8 \text{ cm}^2(\text{v} \cdot \text{sec})^{-1} \text{ from Chanin and}$$
$$\text{Biondi}[8,9]$$

$$K_{4,a} = 9.5 \times 10^{18} \text{ cm}^{-1} \text{ sec}^{-1}$$

The diffusion coefficient K_m for the neon metastable states $3P_2$ and $3P_0$ at $300°K$ has been determined by Phelps[11] from optical absorption measurements on excited neon atoms following a pulsed discharge. For both states, it was found that

$$K_m = 5.5 \times 10^{18} \text{ cm}^{-1} \text{ sec}^{-1}$$

The characteristic diffusion length Λ for infinite parallel plate geometry and for the lowest diffusion mode[9] is (L/π) where L is the plate separation. For $L = 0.3 \text{ cm}$,

$$\Lambda^2 = 9 \times 10^{-3} \text{ cm}^2$$

IV. ELECTRON-ION RECOMBINATION COEFFICIENTS
FOR NEON AND ARGON ATOMIC AND MOLECULAR IONS

There is a dearth of reliable experimental determinations of atomic ion-electron recombination coefficients[$C_1, C_2, C_3, C_{18}, C_{19}$]. This results from the fact that except for dense plasmas ($N_e \gtrsim 10^{14} \text{ cm}^{-3}$) these processes are normally small in comparison with other loss processes and are consequently difficult to measure. The process of radiative recombination[C_1, C_{18}] has, however, been investigated theoretically in some detail for hydrogenic ions

5

(Bates and Dalgarno[12]) and these data are considered to be of high accuracy. For the atomic hydrogen ion H^+ the total radiative recombination coefficient at 250°K is $4.84 \times 10^{-12} cm^3 sec^{-1}$ and at 500°K is $3.12 \times 10^{-12} cm^3 sec^{-1}$. Approximate values of the total radiative recombination coefficient for more complex ions (He^+, Li^+, C^+, N^+, O^+, Ne^+, N_o^+, K^+) have been obtained at 250°K on the assumption that all excited levels are hydrogenic and using known values of the threshold photoionization cross sections from the ground levels of the atoms concerned. For Ne^+ at 250°K, the radiative recombination is $3.4 \times 10^{-12} cm^3 sec^{-1}$ and for the remainder of the ions listed above, the recombination coefficient ranges from 3.0×10^{-12} to $4.8 \times 10^{-12} cm^3 sec^{-1}$ showing that the values do not differ much from one singly charged ion to another. For Ne^+ at 300°K, it is considered that the value of C_1 is close to $3.2 \times 10^{-12} cm^3 sec^{-1}$ and in the absence of explicit data for Ar^+, C_{18} is taken $\approx 4 \times 10^{-12} cm^3 sec-1$ by analogy with the atomic ions considered above.

$$C_1 = 3.2 \times 10^{-12} cm^3 sec^{-1}$$

$$C_{18} \approx 4 \times 10^{-12} cm^3 sec^{-1}$$

C_2, C_3 and C_{19} represent 3-body atomic ion-electron recombination coefficients, where the third body for C_2 and C_{19} is a neutral neon atom, and for C_3 is an electron. In this radiationless recombination, the function of the third body is to remove the surplus energy released by recombination. For plasma densities $N_e \sim 10^{12} cm^{-3}$ and gas pressures $\gtrsim 30$ Torr, $N_e/N_o \lesssim 10^{-6}$ so that if $C_3 N_e$ is to be $\sim C_2 N_o$, C_3/C_2 must be $\gtrsim 10^6$. It is inconceivable that an electron would be a million times more efficient than a gas atom for the removal of surplus energy, so that under the present conditions $C_3 \ll C_2 N_o/N_e$ and need not be considered further. (The coefficient corresponding to C_3 for A^+ would also lead to a negligible recombination loss in comparison with $C_{19}N_o$ and has therefore been omitted from the equation for A^+, Table I.)

Approximate values of C_2 and C_{19} may be obtained from an extension of the classical theory of Thomson (Massey and Burhop[13]). The general expression for C_2 and C_{19} is

$$C = \frac{(8kT/\pi m)^{1/2}\, 8\, \pi\, r_o^3\, m}{3\, M\, q_e\, n^2} \tag{5}$$

where m is the electron mass, M is the mass of the gas atom, n is the number density of atoms at 1 Torr and 273°K and q_e is the total elastic cross section for electron-atom collisions. Recombination is assumed to occur when electrons and ions approach each other within a distance r_o defined by

$$r_o = \frac{2e^2}{3kT} \tag{6}$$

$$= 3.71 \times 10^{-6} \text{ cm at } T = 300°K.$$

On this simplified view of 3-body recombination, the important consideration is the rate at which electrons can lose energy in collisions with neutral atoms, which is dependent on M and q_e for a given temperature. Since $N_O \gg A_O$, M and q_e are respectively the mass of the neon atom and the neon atom-electron cross section in the calculation for C_2 and also for C_{19} so that $C_2 = C_{19}$. The value of q_e for neon is determined from the experimental values of P_c, the probability of collision of electrons in neon ($q_e = 0.283 \times 10^{16} P_c$) obtained by Gilardini and Brown.[14] At 300°K, $P_c = 1.3(\text{cm.Torr})^{-1}$, so that $q_e = 3.7 \times 10^{-17} \text{ cm}^2$.

$$C_2, C_{19} = \frac{(8 \times 1.38 \times 10^{-16} \times 300/3.14 \times 9.11 \times 10^{-28})^{1/2}}{3 \times (20 \times 1.67 \times 10^{-24}) \times 3.7 \times 10^{-17} \times (3.54 \times 10^{16})^2}$$

$$\times 8 \times 3.14 \times (3.71 \times 10^{-6})^3 \times 9.11 \times 10^{-28}$$

$$C_2, C_{19} = 2.7 \times 10^{-30} \text{ cm}^6 \text{ sec}^{-1}$$

In contrast to the dearth of experimental determinations of atomic ion-electron recombination coefficients, many reliable experimental values are available for molecular ion-electron dissociative recombination (C_{16}, C_{21}). This process can occur rapidly and is often the dominant loss mechanism in plasmas for which $N_O \gtrsim 5 \times 10^{17} \text{ cm}^{-3}$ and $N_e \sim 10^{12} \text{ cm}^{-3}$. The latest published values[15] of C_{16} and C_{21} at 300°K given below are in good agreement with earlier values obtained by Biondi[16] and Biondi and Brown.[17]

$$C_{16} = 2.2 \times 10^{-7} \text{ cm}^3 \text{ sec}^{-1} \quad \text{from Oskam and Mittelstadt}[15]$$

$$C_{21} = 6.7 \times 10^{-7} \text{ cm}^3 \text{ sec}^{-1} \quad \text{from Oskam and Mittelstadt}[15]$$

V. PRODUCTION OF
EXCITED STATES FROM RECOMBINATION PROCESSES

It is energetically possible that the recombination of neon ions and electrons can lead to the production of excited neon states (C_8, C_{10}, C_{11}). Similar coefficients for the production of excited argon states are not considered, since such states cannot usefully contribute by any scheme to the total ion density. Theoretical studies by Bates and Dalgarno[12] on radiative recombination have shown that in the case of H^+ ions, electron capture to the ground state is ~ 10 times more probable than electron capture to a highly excited state. On this basis C_8 for radiative recombination (C_1) is ~ 0.1. There should, in fact, be a different coefficient in Table 1 for the production of excited states from the Thomson 3-body recombination process (C_2). However, since 3 bodies are available for efficient removal of the energy of recombination, the probability of one of the atoms being in an excited state after recombination is expected to be small. Furthermore since there is no published work on the production of excited states by 3-body recombination,

7

and more importantly, since atomic ion-electron recombination is not a significant loss process for neon under the present conditions, the separation of C_8 into two coefficients is not necessary. Similar arguments apply to the production of metastable states C_{10} from atomic ion-electron recombination. Since the energy of recombination has to be shared among the N_x and N_m states, it is expected that ~ 0.1 would be an upper bound for both C_8 and C_{10}, but much significance should not be attached to this value.

$$C_8, \; C_{10} \lesssim 0.1$$

Contrary to the unimportance of C_8 and C_{10}, precise knowledge of C_{11} is highly relevant to the present study because of the large value of C_{16} and the consequent possibility of a significant source of metastable states via $C_{11}C_{16}$ $N_{2+}N_e$. Unfortunately, little is known about the production of excited or metastable states from dissociative recombination, although it is generally accepted that the dissociative recombination of diatomic noble gas ions leads to one of the dissociative atoms being left in an excited state (Biondi and Holstein[18]). Recent work by Biondi et al. on the dissociative recombination mechanism in neon[19] and helium[20] plasmas using microwave, optical spectrometric and interferometric techniques, has indicated that dissociative recombination into high-lying atomic excited states is a likely process. Since the transition probabilities of some of the excited states (above the metastable states) to the ground state is finite, C_{11} is likely to be less than one, but further identification of the high-lying excited states is required for estimations of C_{11}.

$$C_{11} < 1$$

VI. THREE-BODY MOLECULAR ION FORMATION

The coefficient C_4 for the conversion of atomic neon ions into molecular ions in 3-body collisions involving the neon ion and two neon atoms, has been determined by Beaty and Patterson.[21]

$$C_4 \;=\; 5.8 \times 10^{-32} \; cm^6 \; sec^{-1}$$

The coefficient C_5, representing a collision between an atomic neon ion, a neon atom and an argon atom, is not known, but since the argon takes no part in the collision except to satisfy conditions for conservation of momentum, C_5 will be approximately equal to C_4. More precise knowledge of C_5 is not required for the present conditions since $N_o \gg A_o$ and thus $C_4 N_o^2 \gg C_5 N_o A_o$.

$$C_5 \;\approx\; 5 \times 10^{-32} \; cm^6 \; sec^{-1}$$

The production rate of molecular argon ions, C_{20}, from 3-body collisions involving an atomic argon ion, an argon atom and a neon atom has been investigated experimentally by Oskam.[22] The relevant conversion frequency is found to be

$$C_{20} \;=\; 2.5 \times 10^{-31} \; cm^6 \; sec^{-1}$$

VII. TWO-BODY CHARGE EXCHANGE

Two-body charge exchange (C_6, C_{17}) is energetically possible when the potential energy of the incident ion is greater than or equal to the ionization energy of the target atom. Massey and Burhop[13] have indicated that the cross section for charge exchange will be maximum when the collision time $a/\bar{v}$ is approximately equal to the time for electronic transition $h/\Delta E$. The quantity a is of order 10^{-8} cm, the diameter of an atom, $\bar{v}$ is the relative velocity of approach of the two particles, h is Planck's constant and ΔE is the difference in the ionization energies of the unlike colliding particles. For maximum cross section

$$\bar{v}_m \approx \frac{a \Delta E}{h} .\tag{7}$$

For the reaction represented by $C_6 (Ne^+ \longrightarrow Ar^+)$, $\Delta E = 6$ ev; for C_{17} $(Ne_2^+ \longrightarrow Ar^+)$, $\Delta E \sim 5$ ev from the data of Mason and Vanderslice.[3] Using these values, $\bar{v}_m$ becomes respectively $= 10^7$ cm sec^{-1} and $\sim 8 \times 10^6$ cm sec^{-1}. For temperature $T°K$, $\bar{v} = (8kT(M_1 + M_2)/\pi M_1 M_2)^{1/2}$ where M_1 and M_2 represent the mass of particles 1 and 2 involved in the collision. At $300°K$, $\bar{v}$ is given by

$$\bar{v}(Ne, Ar) = \left(\frac{8 \times 1.38 \times 10^{-16} \times 300 \times 60}{3.14 \times 20 \times 40 \times 1.66 \times 10^{-24}} \right)^{1/2} = 6.9 \times 10^4 \text{ cm sec}^{-1}.$$

Similarly $\bar{v}(Ne_2, Ar) = 5.7 \times 10^4$ cm sec^{-1}.

Therefore, since $\bar{v} \ll \bar{v}_m$ for both the atomic and molecular neon ion it is evident that the charge exchange cross sections (q_{cx}) will be small (compared to gas kinetic $q \sim 10^{-16}$ cm^2) for the values of ΔE and low relative velocities considered here. $q_{cx}(Ne \longrightarrow Ar^+)$ at $300°K$ can be approximately estimated by extrapolation of the theoretical data obtained by Hasted[23] for energies ~ 12 to 30 ev, but no data are available for the molecular neon ion. However, despite the difference in value for ΔE for the atomic and molecular ion, the charge exchange cross sections at $300°K$ (far from the maximum cross section) will tend to converge towards zero so that $q_{cx}(Ne \longrightarrow Ar^+)$ is taken to be $\sim q_{cx}(Ne^+ \longrightarrow Ar^+)$. From Hasted[23], the extrapolated value for the probability of charge exchange $(Ne^+ \longrightarrow Ar^+)$ $P_{cx} \approx 0.2$ cm^{-1}. Therefore, since C_6, C_{17} is given by $\bar{v} P_{cx}$ 0.283×10^{-16},

$$C_6, C_{17} \approx 3.9 \times 10^{-13} \text{ cm}^3 \text{ sec}^{-1}$$

VIII. COLLISIONS INVOLVING METASTABLE STATES

The concentration N_m of neon metastable states in the present study is sufficiently low ($\sim 10^{10} - 10^{11}$ cm^{-3}, Section II) that collisions between pairs of metastable states will be very small in comparison with collisions between a metastable state and a neutral atom. Even so, an order-of-magnitude estimate of the coefficients C_7, C_{12} is useful in establishing that the

influence of metastable-metastable collisions is negligibly small. The metastable-metastable ionizing cross section does not appear to have been determined for neon, but the cross section has been estimated by Phelps[24] for the case of helium. Phelps obtains $q_m \approx 10^{-14}$ cm^2, and on the basis that the ionizing cross section for neon metastables is of similar order of magnitude, $C_7 (= q_m \, \bar{v}(Ne,Ne)$ where $\bar{v} = 8 \times 10^4$ cm sec^{-1}) becomes

$$C_7 \approx 8 \times 10^{-10} \text{ cm}^3 \text{ sec}^{-1}$$

In some recent work, Myers[25] has suggested that metastable-metastable ionizing collisions lead to the production of molecular ions and not atomic ions. However, since studies presently being conducted by Biondi,[20] together with earlier work,[26,27] strongly support the conclusion that metastable-metastable ionizing collisions yield atomic ions, the possible production of molecular ions from metastables is not considered here.

All of the collisions between metastable states do not lead to atomic ion production so that $C_{12} > C_7$ although not necessarily by a significant amount. Because of the large "size" of the metastable atom, the cross section for collision between metastable states will be larger than the gas kinetic cross section for collision of neutral states. However, the value of q_m above is already so large that it suggests that almost all of the metastable-metastable collisions lead to ionization. For the present purposes such an estimate is considered sufficient.

$$C_{12} \approx 8 \times 10^{-10} \text{ cm}^3 \text{ sec}^{-1}$$

The predominant destruction processes for neon metastables in the volume of the gas are 2-body collisions (C_{13}) with neon atoms, 3-body collisions (C_{14}) with neon atoms, and 2-body ionizing collisions (C_{15}) with argon atoms (Penning effect). All these processes have been experimentally investigated in some detail. The cross section, q_i for ionization of an argon atom by a neon metastable, has been determined by Biondi[28] as 2.6×10^{-16} cm^2. The product of q_i and $\bar{v}(Ne,A)$ yields C_{15}.

$$C_{15} = 1.8 \times 10^{-11} \text{ cm}^3 \text{ sec}^{-1}.$$

Low pressure microwave studies ($p \leq 2.5$ Torr) by Biondi[28] of the destruction of neon metastables in neon indicated that the predominant volume loss was by 2-body collisions with a destruction cross section $q_d = 8.9 \times 10^{-20}$ cm^2. On this basis $C_{13} = 7.1 \times 10^{-15}$ cm^3 sec^{-1}. However, subsequent more detailed studies were undertaken by Phelps[11] using optical absorption techniques to measure decay rates of excited atoms, and these investigations showed that at higher neon densities ($10^{17}-10^{19}$ atoms cm^{-3}) the volume destruction of metastable states was complex, involving excitation and de-excitation of the $3P_0$ and $3P_2$ metastable states to the nearby $3P_1$ resonant radiating state and also involving 3-body destruction. The 3-body destruction term became increasingly important as expected for $N_0 > 10^{18}$ atom cm^{-3}, and for $N_0 = 10^{19}$ atom cm^{-3} the destruction rate was given by $C_{14} N_0^2 N_m$ where

$C_{14} = 5 \times 10^{-34}$ cm^6 sec^{-1} at 300°K. Experimental values of the decay rate of metastables were obtained for $5 \times 10^{15} \lesssim N_o \lesssim 10^{19}$ atoms cm^{-3} and Phelps was successfully able to fit all the experimental points with a single expression which contained diffusion loss ($K_m/N_o \Lambda^2$ dominant at low pressures) 3-body destruction loss ($C_{14} N_o N_m$ dominant at high pressures) and a term which took into account the excitation and de-excitation transfers which occur between the $3P_o$, $3P_2$ and $3P_1$ states. Use of the latter term requires a knowledge of the ratios of the number densities of both the $3P_o$ and $3P_2$ metastable states to the $3P_1$ state and these data have been given by Phelps for the range of values of N_o investigated.

For the present studies, however, Phelps' full expression may be considerably simplified in the following manner, without significant loss of accuracy. The characteristic diffusion length used by Phelps was given by $\Lambda^2 = 0.050$ cm^2 so that in comparison with the present case ($\Lambda^2 - 0.009$ cm^2, Section III), diffusion loss was much smaller. For values of $\Lambda^2 < 0.01$ cm^2, diffusion loss will dominate for $N_o \lesssim 4 \times 10^{17}$ atom cm^{-3}. For the range $4 \times 10^{17} \lesssim N_o \lesssim 8.5 \times 10^{18}$ atom cm^{-3} ($N_o = 8.5 \times 10^{18}$ is p = 240 Torr) the total volume destruction frequency given by Phelps may be approximated by an effective 2-body destruction cross section $q_{eff} = 4.5 \times 10^{-20}$ cm^2 or $\nu_{eff} = 3.6 \times 10^{-15}$ cm^3 sec^{-1} where $\nu_{eff} N_o = C_{13} N_o + C_{14} N_o^2$. A measure of the degree of approximation is given in Table II.

TABLE II

Comparison of Effective Decay Frequency for
2-Body Metastable Destruction with Phelps' Experimental Values

N_o (atom cm^{-3})	Effective Decay Frequency for 2-body Destructive Collision, $\nu_{eff} N_o$ sec^{-1} with $\nu_{eff} = 3.6 \times 10^{-15}$ cm^3 sec^{-1}	Phelps' Experimental Value of Total Decay Frequency
8.5×10^{18}	3.1×10^4 sec^{-1}	4.0×10^4 sec^{-1}
4×10^{18}	1.4×10^4	1.2×10^4
1×10^{18}	3.6×10^3	2.8×10^3
8×10^{17}	2.9×10^3	2.5×10^3
4×10^{17}	1.4×10^3	1.4×10^3

Evidently, for $\Lambda^2 < 0.01$ cm^2 and $4 \times 10^{17} \lesssim N_o \lesssim 8.5 \times 10^{18}$ atom cm^{-3}, $C_{13} + C_{14} N_o$ may be approximated by ν_{eff} where

$$\nu_{eff} = 3.6 \times 10^{-15} \text{ cm}^3 \text{ sec}^{-1}$$

IX. COLLISIONS INVOLVING HIGHLY-EXCITED STATES

It has been mentioned previously (Section II) that the production of molecular neon ions from highly-excited states N_x (Hornbeck-Molnar process[2]) is

11

not an important process under the present conditions. However, typical values of $(q_m \tau)$, where q_m is the cross section for ion formation from N_x and τ is the mean lifetime of N_x, have been determined by Hornbeck[29] for helium, neon and argon and the value for neon is $\approx 5 \times 10^{-23}$ cm^2 sec. This value of $(q_m \tau)$ yields the ratio of the number of molecular ions formed sec^{-1} to the number of excited atoms decaying sec^{-1} under given conditions since this ratio is

$$\frac{N_x N_o q_m \bar{v}}{N_x/\tau} = N_o \bar{v} q_m \tau \qquad (8)$$

For $N_o = 3.54 \times 10^{18}$ atoms cm^{-3} (p = 100 Torr), $N_o \bar{v} q_m \tau \approx 14$ which indicates that 14 molecular ions will be formed from N_x for each N_x that radiatively decays. Evidently for the situation of copious production of excited states N_x with sufficient energy for the production of Ne_2^+ (within ~ 1 ev of $E_i(Ne) = 21.6$ ev)[3] this process would be a significant source of molecular ion generation.

It is worth noting that if q_m is of large atomic magnitude $\approx 10^{-15}$ cm^2 (since the N_x state is highly excited), then $\tau \approx 5 \times 10^{-8}$ sec which appears reasonable. The coefficient C_9 would then be of order of magnitude 8×10^{-11} cm^3sec^{-1}.

$$\tau \approx 5 \times 10^{-8} \text{ sec}$$

$$C_9 \approx 8 \times 10^{-11} \text{ cm}^3 \text{ sec}^{-1}$$

X. COLLECTION OF DATA

The production, diffusion and conversion coefficients of ions and metastable states discussed in this report are summarized for convenience in Table III. All the data are evaluated for a temperature of 300°K.

TABLE III

Rate Coefficients for Ne/Ar Plasma at 300°K

Process	Symbol	Value
Production Ne^+ by fission fragments	S_o	2.6×10^{-3} sec^{-1}
Diffusion Ne^+ in Ne	$K_{1,a}$	5.7×10^{18} cm^{-1} sec^{-1}
2-body radiative recombination Ne^+	C_1	3.2×10^{-12} cm^3 sec^{-1}
3-body Thomson recombination Ne^+	C_2	2.7×10^{-30} cm^6 sec^{-1}
3-body 2-electron recombination Ne^+	C_3	$\ll C_2 N_o/N_e$ cm^6 sec^{-1}
3-body $Ne^+ \longrightarrow Ne_2^+$ with 2 Ne	C_4	5.8×10^{-32} cm^6 sec^{-1}
3-body $Ne^+ \longrightarrow Ne_2^+$ with Ne,Ar	C_5	$\approx 5 \times 10^{-32}$ cm^6 sec^{-1}
2-body $Ne^+ \longrightarrow Ar^+$	C_6	$\approx 4 \times 10^{-13}$ cm^3 sec^{-1}
Metastable-metastable $Ne^m \longrightarrow Ne^+$	C_7	$\approx 8 \times 10^{-10}$ cm^3 sec^{-1}
Production Ne_x by fission fragments	S_1	$\ll S_2$ sec^{-1}
Production Ne_x by atomic recombination	C_8	$\lesssim 0.1$
Mean lifetime Ne_x	τ	$\approx 5 \times 10^{-8}$ sec
2 body ion formation $Ne_x \longrightarrow Ne_2^+$	C_9	$\approx 8 \times 10^{-11}$ cm^3 sec^{-1}
Production Ne_m by fission fragments	S_2	1.3×10^{-3} sec^{-1}
Diffusion Ne_m in Ne	K_m	5.5×10^{18} cm^{-1} sec^{-1}
Production Ne_m by recombination of Ne^+	C_{10}	$\lesssim 0.1$
Production Ne_m by recombination of Ne_2^+	C_{11}	< 1.0
Metastable-metastable Ne^m destruction	C_{12}	$\approx 8 \times 10^{-10}$ cm^3 sec^{-1}
Destruction Ne_m via Ne	$\nu_{eff} (= C_{13} + C_{14} N_o)*$	3.6×10^{-15} cm^3 sec^{-1}
Penning destruction $Ne_m + Ar \rightarrow Ar^+$	C_{15}	1.8×10^{-11} cm^3 sec^{-1}
Diffusion Ne_2^+ in Ne	$K_{2,a}$	9.1×10^{18} cm^{-1} sec^{-1}
2-body dissociative recombination Ne_2^+	C_{16}	2.2×10^{-7} cm^3 sec^{-1}
2-body $Ne_2^+ \longrightarrow Ar^+$	C_{17}	$\approx 4 \times 10^{-13}$ cm^3 sec^{-1}
Diffusion Ar^+ in Ne	$K_{3,a}$	1.0×10^{19} cm^{-1} sec^{-1}
2-body radiative recombination Ar^+	C_{18}	$\approx 4 \times 10^{-12}$ cm^3 sec^{-1}
3-body Thomson recombination Ar^+	C_{19}	2.7×10^{-30} cm^6 sec^{-1}
3-body $Ar^+ + Ar + Ne \longrightarrow Ar_2^+$	C_{20}	2.5×10^{-31} cm^6 sec^{-1}
Diffusion Ar_2^+ in Ne	$K_{4,a}$	9.5×10^{18} cm^{-1} sec^{-1}
2-body dissociative recombination Ar_2^+	C_{21}	6.7×10^{-7} cm^3 sec^{-1}
Characteristic diffusion length	Λ^2	9×10^{-3} cm^2

*The approximation of $C_{13} + C_{14} N_o$ to ν_{eff} is valid for $\Lambda^2 < 0.01$ cm^2 and $4 \times 10^{17} \lesssim N_o \lesssim 8.5 \times 10^{18}$ atom cm^{-3}.

REFERENCES

1. D. J. Rose, "Reaction kinetics of the fission fragment plasma", Section B of this report.

2. J. A. Hornbeck and J. P. Molnar, Phys. Rev., 84, 621 (1951).

3. E. A. Mason and J. T. Vanderslice, J. Chem. Phys., 30, 599, (1959).

4. R. L. Platzman, Int. J. Appl. Radiation and Isotopes, 10, 116, (1961).

5. N. G. Utterback and G. H. Miller, Phys. Rev., 116, 976, (1959).

6. H. J. Oskam and V. R. Mittelstadt, Phys. Rev., 132, 1435, (1963).

7. E. W. McDaniel, Collision Phenomena in Ionized Gases, (Wiley), (1964).

8. L. M. Chanin and M. A. Biondi, Phys. Rev., 107, 1219, (1957).

9. S. C. Brown, Basic Data of Plasma Physics, (Wiley), (1959).

10. A. M. Tyndall, The Mobility of Positive Ions in Gases, (Cambridge),(1938).

11. A. V. Phelps, Phys. Rev., 114, 1011, (1959).

12. D. R. Bates and A. Dalgarno, Electronic Recombination in Atomic and Molecular Processes, (Edited by D. R. Bates), (Academic), (1962).

13. H. S. W. Massey and E. H. S. Burhop, Electronic and Ionic Impact Phenomena, Oxford, (1962).

14. A. L. Gilardini and S. C. Brown, Phys. Rev., 105, 31, (1957).

15. H. J. Oskam and V. R. Mittelstadt, Phys. Rev., 132, 1445, (1963).

16. M. A. Biondi, Phys. Rev., 129, 1181, (1963).

17. M. A. Biondi and S. C. Brown, Phys. Rev., 76, 1697, (1949).

18. M. A. Biondi and T. Holstein, Phys. Rev., 82, 962, (1951).

19. T. R. Connor and M. A. Biondi, 16th Gaseous Electronics Conf., Pittsburgh, (1963); Bull. Am. Phys. Soc. 9, 184, (1964).

20. W. A. Rogers and M. A. Biondi, Phys. Rev., 134, A1215, (1964).

21. E. C. Beaty and P. Patterson, 6th International Conference on Ionization Phenomena in Gases, Paris, (1963).

22. H. J. Oskam, Philips Res. Rep., 13, 401, (1958).

23. J. B. Hasted, Proc. Roy. Soc., A205, 421, (1951).

REFERENCES (Continued)

24. A. V. Phelps, Communication to M. A. Biondi, Phys. Rev., 88, 660, (1952).

25. H. Myers, Phys. Rev., 130, 1639, (1963).

26. A. V. Phelps and S. C. Brown, Phys. Rev., 86, 102, (1952).

27. A. V. Phelps and J. P. Molnar, Phys. Rev., 89, 1202, (1953).

28. M. A. Biondi, Phys. Rev., 88, 660, (1952).

29. J. A. Hornbeck, in Basic Processes of Gaseous Electronics by L. B. Loeb, (University of California) (1955).

SECTION E

SECTION E

ION GENERATION RATE MEASUREMENTS IN AN ARGON-CESIUM MIXTURE

ABSTRACT

Ion generation rate measurements were made on an argon-cesium gas mixture
using modified versions of the noble gas ionization tube. Data from the first
two tubes were inconclusive due to the difficulty of transporting cesium vapor
in argon (at 240 torr) for the tube configuration used. A study of cesium trans-
port in argon showed that a period of one to two hours is needed to establish
equilibrium and this suggested further modifications to tube design. The third
ion tube, thus modified, operated successfully in the reactor. The data indi-
cated that for Cs/Ar of 10^{-5} at an argon pressure of 240 torr, the I-V data
followed a $(V)^{1/2}$ relationship and indicated that the ion generation rate is
significantly higher than that for Ne-Ar or the pure gases for the same condition.

CONTENTS

1. INTRODUCTION

The results for Ne-Ar (Section C) suggested that some other mixed gas systems might be capable of sustaining high ion densities when ionized by fission fragments. For applications in thermionic converters argon seeded with cesium was considered to be an attractive Penning-type system because of the small electron scattering cross section of argon and the low ionization potential of cesium.

The ion generation rate program was thus oriented towards a study of Ar-Cs plasma generated by fission fragments. For this purpose the noble gas ion tube was modified to be compatible with cesium. Since currents of order ma. or less were expected, the measuring circuit had to be designed to nullify the influence of leakage current across the ceramic insulator.

The results of the first two tubes are described briefly. These suggested that the results were influenced by atom transport effects in the Ar-Cs system. The transport of cesium in argon was subsequently studied in the laboratory and this led to a major modification in the ion tube geometry. The results from the data obtained inpile with this tube are presented in terms of the ion transport and ion generation rate models developed for the noble gas system.

II. CIRCUIT

In the accurate determination of small ($\lesssim 10^{-2}$ amps) ionization currents in diodes filled with cesium vapor, care must be taken to ensure that leakage currents across cesium-covered insulators do not affect the measurements of ionization currents. The leakage current between two electrodes of differing potential can be eliminated by using a split-insulator, one section of which is maintained at the potential of one of the electrodes. Evidently, no leakage path can then exist across this equipotential surface.

The three-electrode ceramic-metal chamber, previously employed for studies of ion source rate in noble gases, was modified to utilize this split-insulator principle for cesium studies. The portion of the center electrode that was interior to the tube was cut away to leave an annular Kovar disc which was level with the two adjacent ceramics (Fig. 1).
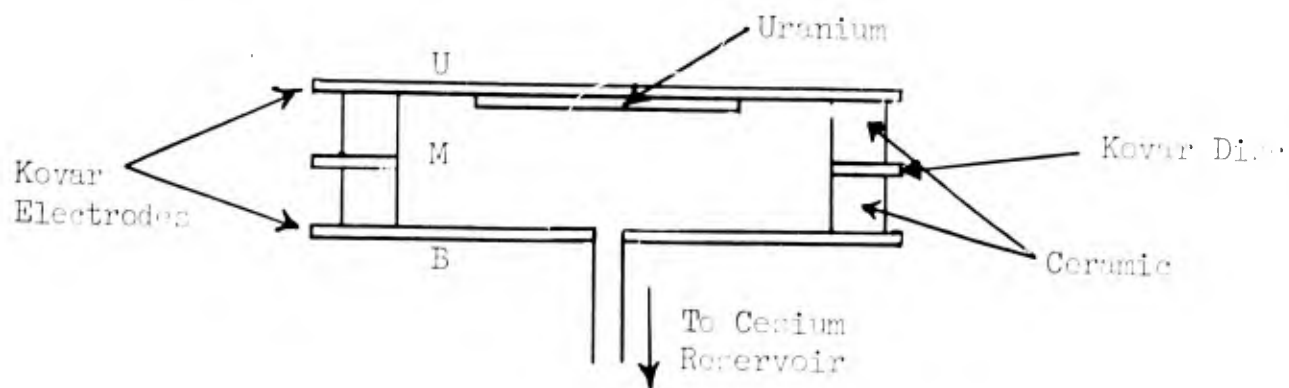
Fig. 1. Ar-Cs ion tube schematic.

If a potential source is applied across UM, and MB is shorted with a lead of negligible resistance, no leakage current can flow between U and B. The distribution of electric field in the diode between U and B will not be significantly altered by the presence of M because the ratio of the gap separation to the electrode diameter is small (~ 0.2).

However, in order to measure the ionization current in the diode a current meter (A_{UB}) must be placed in series with U and B and adjacent to B as shown in Fig. 2.
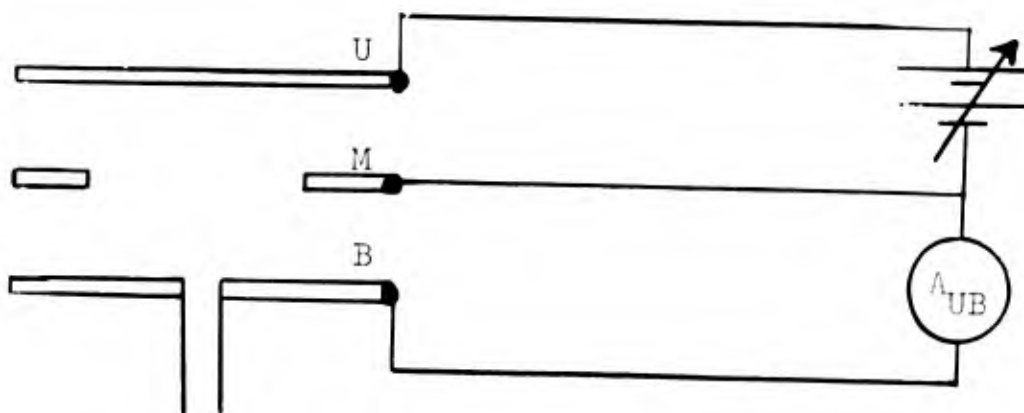
Fig. 2. Circuit that would measure ion current but as well would measure current due to leakage across the ceramic.

Since the passage of ionization current through A_{UB} produces a potential drop, V_{MB}, across M and B (0.1 v for full-scale deflection on a Hexem meter) a feedback loop must be provided in order to maintain this potential drop as close to zero as possible. Since the Hexem is already provided with a potential

3

compensator in the form of a -1 volt full-scale output, this was used in conjunction with a high-impedance divider and a Kintel amplifier (Model 114C) to continuously maintain V_{MB} close to zero. The arrangement is shown in Fig. 3. (The maximum current through the output terminals of the Hexem meter cannot exceed 120 μA so that the Hexem alone cannot be used as a voltage compensator for ionization currents $\gtrsim$ milliamps.)
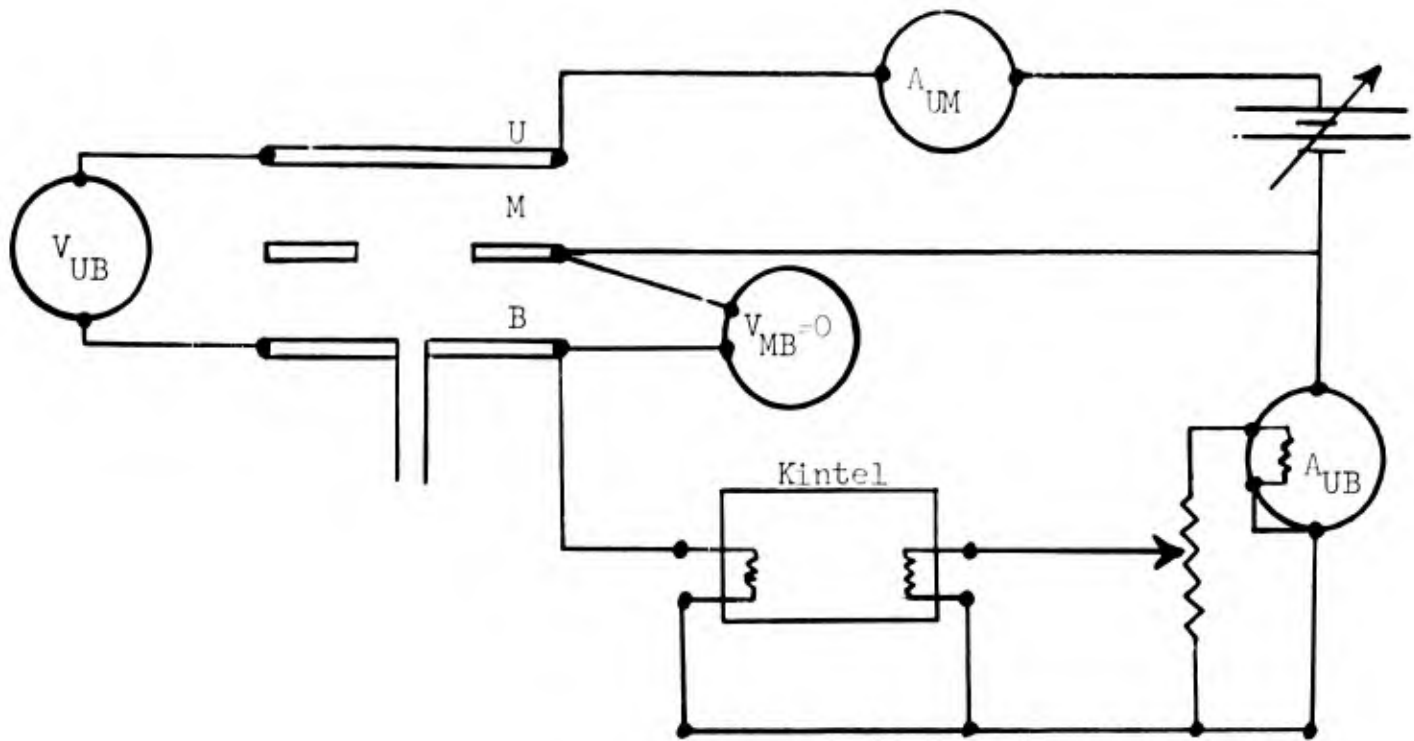
Fig. 3. Circuit used to nullify influence of cesium leakage across ceramic.

The current-voltage characteristic for this cesium diode is then given by A_{UB} vs. V_{UB} when $V_{MB} = 0$.

For the accurate determination of ionization currents $\lesssim$ μA, stringent conditions of voltage balance are often required between M and B. Experimental tests with a cesium-filled ceramic-metal diode indicated that the leakage resistance between M and B (R_{MB}) can be as low as $\sim$ 500 Ω. (Most often, R_{MB} was found to be $\sim$ 1000-2000 Ω for liquid cesium temperatures $\sim$ 300°C.) Now if the largest error that can be tolerated in ionization current I due to a potential drop δV_{MB} is $\sim$ 1%, then

$$\delta V_{MB} \leq 10^{-2} \ R_{MB} \ I$$

$$\text{(for } R_{MB}=500 \ \Omega, I=10^{-6}A)$$

$$= 5 \times 10^{-6} \ \text{volts}.$$

Under these conditions it becomes essential to use separate non-current carrying leads to measure V_{MB}. Evidently for larger values of $R_{MB} \times I$, the conditions of voltage balance become correspondingly less stringent.

III. RESULTS OF ARGON-CESIUM TUBES 1 AND 2

A. Tube Design

The components of the noble gas ion tube(Fig.10,Sec.A)were found to be compatible with cesium up to bath temperatures around 250°C. Operation at higher temperatures - 400°C - presented problems which were a function of materials, e.g. choice of alumina, and particularly of pinch-off tubulation. The latter problem was solved by employing a copper rather than a Kovar pinch-off as previously used.

The basic tube structure was that of Fig.10,Sec.A with the center electrode cut out to allow nulling the leakage current across the alumina insulator rings due to cesium coverage. The interelectrode spacing for this tube was 6.25 mm or about twice that of the earlier noble gas ion tubes because of the removal of the center electrode and the use of the original ceramic rings as insulators.

The tube was mounted in an oil filled four foot support section and inside an electrical heater assembly as seen in Fig. 4. Electrical heat was applied independently to three heaters, top (above the tube), middle and stem (tubulation). Chromel alumel thermocouples were mounted on the uranium, middle and bottom electrodes and two were on the end of the tubulation (stem thermocouples).

B. Argon-Cesium Ion Tube 1

This tube was processed in a manner similar to noble gas tubes up to the backfilling stage. It was backfilled with argon at 240 torr and sealed from the system with the cesium chromate pellets attached. After seal-off the pellets were fired and the cesium was transferred into the tube by applying heat to the pellet vial. The copper tubulation was then pinched off. Due to the presence of the argon, the cesium did not transport too readily and considerable
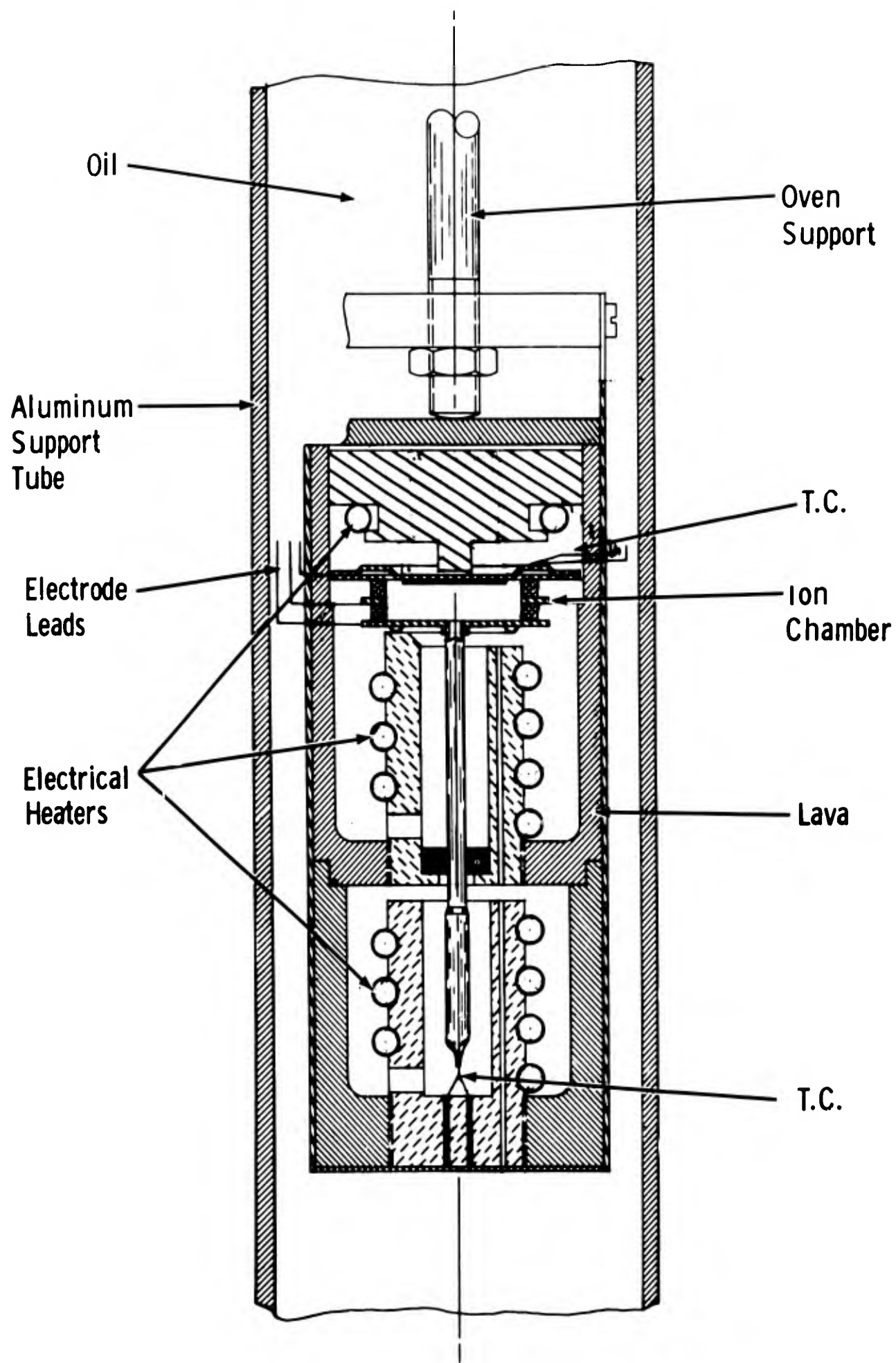
5

Fig. 4. Oven for argon-cesium ion tube, with
tube configuration of tubes 1 and 2.

darkening of the glass vial was observed. There was no perceptible leakage across the ceramics due to cesium coverage. It was concluded that due possibly to difficulty of transport in the argon, the cesium condensed on the tubulation before entering the major tube volume. Presumably cesium could be on the tubulation attached to the sealed-off ceramic tube so that no further tests were felt necessary to establish the presence of cesium. A breakdown test (as a function of bath temperature) was considered but not run due to possible damage to the uranium electrodes. Breakdown of a mockup tube did change as a function of bath temperature indicating that this is a sensitive method for detecting the presence of cesium in noble gases.

Typical data obtained at 2 MW reactor power is shown in Fig. 5.
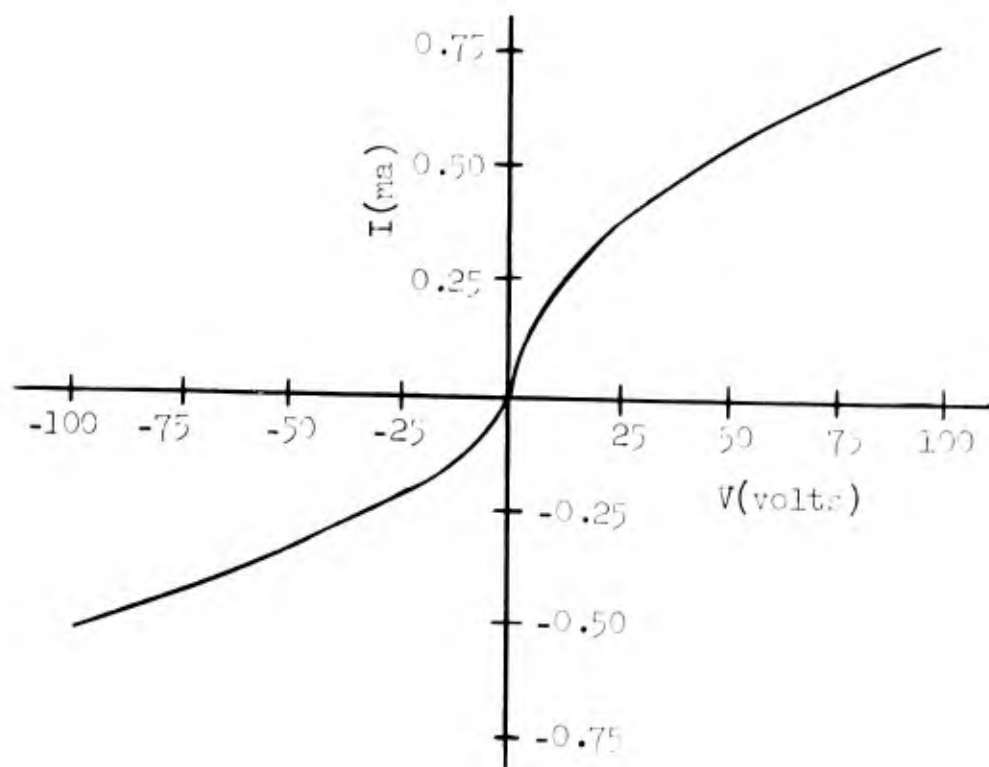
Fig. 5. I-V data for Ar-Cs tube 1 at 2 MW reactor power and $T_{Cs} = 250°C$.

The I-V characteristic appears similar to pure argon data taken earlier, both in shape and in magnitude. The asymmetry in the I-V data is consistent with the fact that more ions are generated near the uranium electrode and subsequently lead to a higher current when that electrode is negative. The cesium stem temperature for these data was 250°C. However, a stem temperature variation from 135°C to 250°C did not influence appreciably the magnitude of the current. These observations suggest that the tube characteristic is that of pure

argon and that the slight influence of cesium bath temperature on tube current
may be due to cesium at much less than its equilibrium vapor pressure.

C. Argon-Cesium Ion Tube 2

To insure the presence of cesium in the next tube it was processed by first
firing the cesium pellets and transporting cesium into the ion tube under vacuum
conditions. Then the argon was backfilled at 240 torr before pinch off. Pres-
ence of cesium was confirmed by a dead short between electrodes occurring when
the cesium was shaken into the ion tube from the tubulation. This tube had a
3 mm electrode gap by the use of thinner ceramic insulator rings.

In order to operate the leakage bucking circuit, a ceramic impedance of
several hundred ohms is needed. Such an impedance was not obtained by thermally
heating the tube with the oven. In addition, several amps at low voltage were
passed through the cesium coating in order to burn it off. Laboratory tests of
this indicated an impedance of hundreds of ohms could be maintained this way
and the tube was then put in the reactor.

The operation of this tube was significantly different from Tube 1. I-V
data could only be obtained at a position 19 in. out from the fully inserted
position of the support tube. At this position the neutron flux is approxi-
mately that obtained for 100 kw reactor power with the tube fully inserted.
Immediately after inserting the tube fully, the leakage resistance of the ion
tube dropped from 60 ohms to 1 ohm or less. Moving the tube 19 in. out
allowed the 60 ohms impedance to be restored by 'burning' the cesium film off
the ceramic.

The current magnitude for Tube 2 was in the same range as that for Tube 1
for equivalent neutron flux. The characteristic followed a $V^{1/2}$ dependence
out to 20 volts but beyond that the current exhibited an increase which may be
indicative of electronic ionization. Cesium bath temperature did not influence
the current magnitude.

These observations suggest that excess cesium was present in the tube which
could not be condensed at the stem cold spot due to the poor transport proper-
ties of cesium in argon. Possibly the following may be occurring. At burn-off
from the ceramic, the cesium condenses onto the electrodes of the diode. Upon
entering a high radiation field, the cesium is boiled off the electrodes by
fission fragments and recondensed onto the ceramic. With a sufficiently

8

low radiation field, the evaporation rate of cesium from the ceramic can be maintained greater than the condensation rate. Therefore it appears that data for argon with cesium at some equilibrium vapor pressure were not obtained.

The data from argon-cesium ion tubes 1 and 2 indicated that it is difficult to maintain cesium at an equilibrium vapor pressure in 240 torr argon in a high radiation field. The mean free path of neutral cesium in argon under these conditions is 2×10^{-6} cm so that diffusion times will be long. Transport studies of cesium transport in argon was thus undertaken.

IV. DIFFUSION RATE OF CESIUM VAPOR IN ARGON

A. Apparatus and Procedure

The apparatus used for the study of the diffusion of cesium in argon is shown schematically in Fig. 6. Two molybdenum electrodes were contained in a glass chamber filled with argon which was connected to a liquid cesium reservoir by a glass tube. The temperature of the chamber and the reservoir section could be independently controlled by means of separate furnaces (indicated in Fig. 6 by dotted lines). On heating the liquid cesium to a constant temperature T_c in the range 473 to 573°K the diffusion and consequent build-up of cesium vapor in the chamber ($T_g \sim 573$°K) continuously changed the value of the sparking potential, V_s, and the leakage resistance, R_L, between the electrodes. (R_L resulted from deposition of cesium on the glass between the electrodes.) When V_s and R_L became constant (at the same time) the pressure of cesium in the chamber was considered to be constant and at the value of the vapor pressure of the liquid cesium at that particular temperature.

Tests on the transport of cesium in vacuum, and in argon at different pressures ($25 \lesssim p \lesssim 240$ torr), indicated that for constant T_g, R_L was dependent only on p_c the pressure of cesium in the chamber; i.e. R_L was not a function of the argon pressure (as was V_s). With this knowledge of R_L as a function of p_c, the following procedure could be adopted for transporting cesium from the reservoir to the chamber. If the required cesium pressure for an Ar-Cs mixture with Cs/Ar of 10^{-3} was P_c with a corresponding bath temperature θ_c ($\theta_c \lesssim 523$°K for $p(Ar) \lesssim 240$ torr), then the liquid cesium was heated to ~ 573°K and maintained at this value until R_L reached a value corresponding to P_c. The liquid cesium
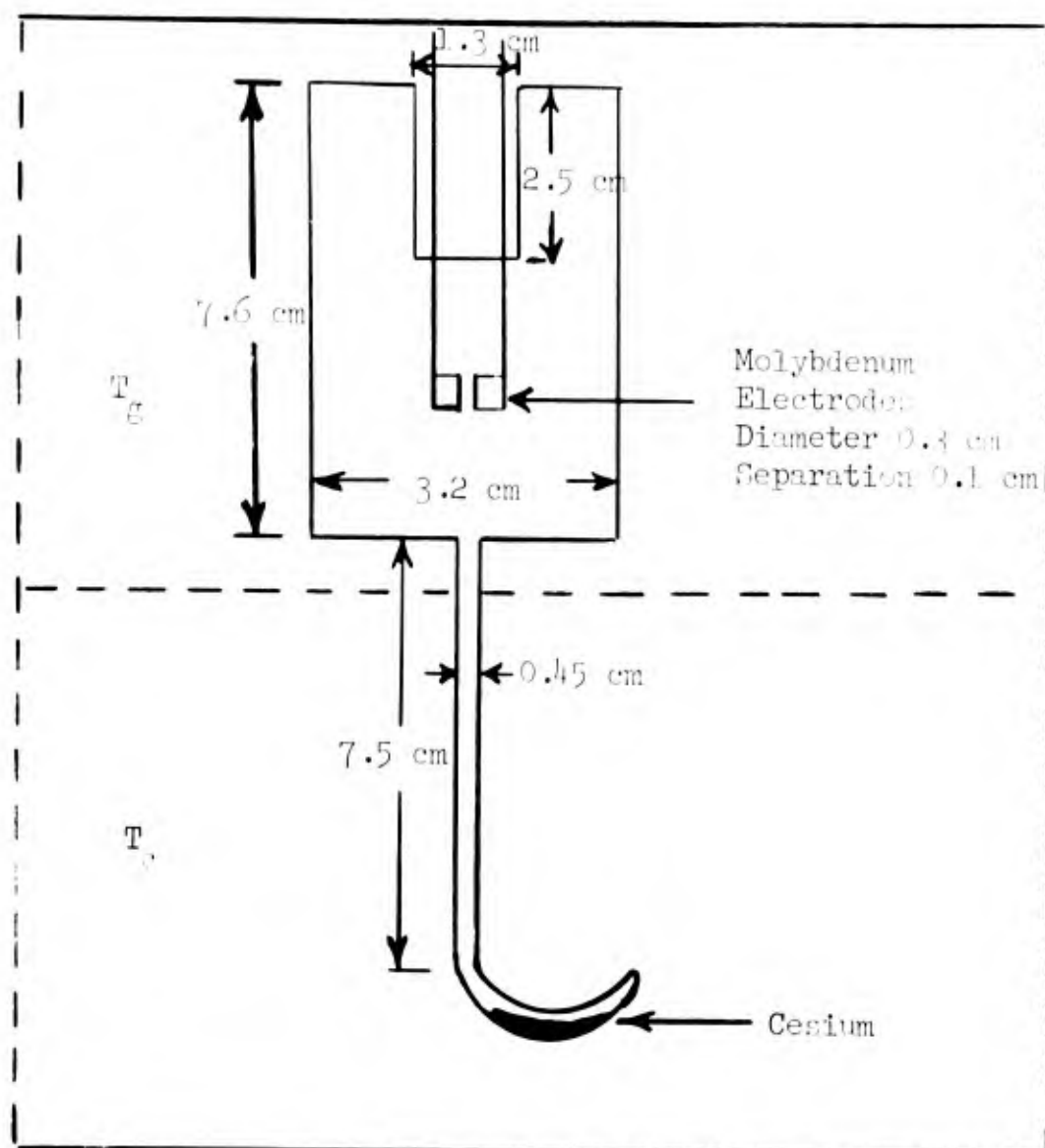
9

Fig. 6. Schematic arrangement for studies of diffusion of cesium vapor in argon.

temperature was then quickly lowered to the value Θ_c. In this manner the diffusion rate of cesium was significantly increased over that which would have been obtained by maintaining the lower bath temperature of Θ_c.

B. Theory

An accurate calculation of the diffusion coefficient D for the diffusion of one gas (or vapor) into another gas is a complicated problem[1] which must take into account the nature of the elastic collisions between dissimilar atoms and also atoms of the same kind. However, a simplified expression for D can be obtained if the concentration n_a of one gas is always much greater than the concentration n_c of the other gas, and if the momentum loss cross section $Q_d(a,c)$ for collision of an atom of each kind is independent of relative velocity. Under these conditions,

low radiation field, the evaporation rate of cesium from the ceramic can be maintained greater than the condensation rate. Therefore it appears that data for argon with cesium at some equilibrium vapor pressure were not obtained.

The data from argon-cesium ion tubes 1 and 2 indicated that it is difficult to maintain cesium at an equilibrium vapor pressure in 240 torr argon in a high radiation field. The mean free path of neutral cesium in argon under these conditions is 2×10^{-6} cm so that diffusion times will be long. Transport studies of cesium transport in argon was thus undertaken.

IV. DIFFUSION RATE OF CESIUM VAPOR IN ARGON

A. Apparatus and Procedure

The apparatus used for the study of the diffusion of cesium in argon is shown schematically in Fig. 6. Two molybdenum electrodes were contained in a glass chamber filled with argon which was connected to a liquid cesium reservoir by a glass tube. The temperature of the chamber and the reservoir section could be independently controlled by means of separate furnaces (indicated in Fig. 6 by dotted lines). On heating the liquid cesium to a constant temperature T_c in the range 473 to 573°K the diffusion and consequent build-up of cesium vapor in the chamber $(T_g \sim 573°K)$ continuously changed the value of the sparking potential, V_s, and the leakage resistance, R_L, between the electrodes. (R_L resulted from deposition of cesium on the glass between the electrodes.) When V_s and R_L became constant (at the same time) the pressure of cesium in the chamber was considered to be constant and at the value of the vapor pressure of the liquid cesium at that particular temperature.

Tests on the transport of cesium in vacuum, and in argon at different pressures $(25 \lesssim p \lesssim 240$ torr), indicated that for constant T_g, R_L was dependent only on p_c the pressure of cesium in the chamber; i.e. R_L was not a function of the argon pressure (as was V_s). With this knowledge of R_L as a function of p_c, the following procedure could be adopted for transporting cesium from the reservoir to the chamber. If the required cesium pressure for an Ar-Cs mixture with Cs/Ar of 10^{-3} was P_c with a corresponding bath temperature θ_c $(\theta_c \lesssim 523°K$ for $p(Ar) \lesssim 240$ torr), then the liquid cesium was heated to $\sim 573°K$ and maintained at this value until R_L reached a value corresponding to P_c. The liquid cesium
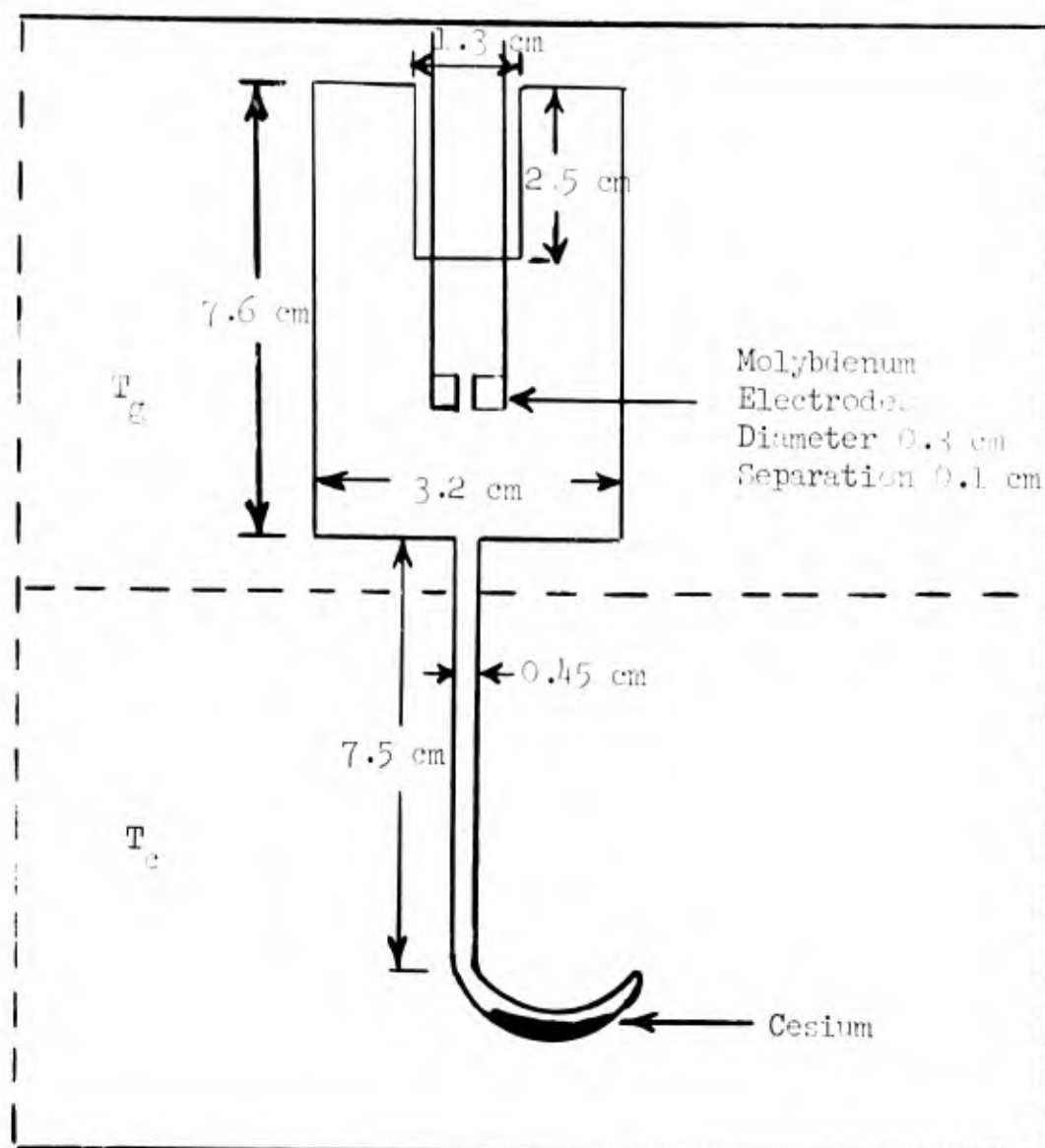
9

Fig. 6. Schematic arrangement for studies of diffusion of cesium vapor in argon.

temperature was then quickly lowered to the value Θ_c. In this manner the dif-
fusion rate of cesium was significantly increased over that which would have
been obtained by maintaining the lower bath temperature of Θ_c.

B. Theory

An accurate calculation of the diffusion coefficient D for the diffusion
of one gas (or vapor) into another gas is a complicated problem[1] which must
take into account the nature of the elastic collisions between dissimilar atoms
and also atoms of the same kind. However, a simplified expression for D can be
obtained if the concentration n_a of one gas is always much greater than the con-
centration n_c of the other gas, and if the momentum loss cross section $Q_d(a,c)$
for collision of an atom of each kind is independent of relative velocity. Under
these conditions,

10

$$D = \frac{3}{8} \left(\frac{\pi \, k \, T(m_a + m_c)}{2 \, m_a m_c} \right)^{1/2} \frac{1}{n_a Q_d} \qquad (n_a >> n_c)$$

$$\simeq \frac{\bar{u}}{3 \, n_a \, Q_d} \, , \quad \text{where} \ \bar{u} = \left(\frac{8 \, k \, T(m_a + m_c)}{\pi \, m_a m_c} \right)^{1/2} . \qquad (1)$$

The suffixes a,c, now refer to argon and cesium, respectively, and $\bar{u}$ is the average relative velocity for collisions of argon and cesium atoms.

In the steady state the current density j_c of cesium atoms due to diffusion is

$$j_c = - \text{grad} \, (n_c D) . \qquad (2)$$

It is assumed that the time taken to obtain a uniform flow rate of cesium through the 0.45 cm diameter tube (Fig. 6) is small compared with the time required to obtain sufficient cesium in the chamber. Since the temperature of the chamber is similar to the temperature of the cesium bath during the time for diffusion (see above procedure) $\bar{u}$ is independent of position. Therefore for diffusion along the axis of the tube,

$$J_c = - \frac{1}{3} \frac{\bar{u} \, \sigma}{n_a Q_d} \frac{dn_c}{dz} \qquad (3)$$

where J_c is the current of cesium atoms per second passing through the cross sectional area σ of the tube. For $\frac{dn_c}{dt} = 0$, the concentration gradient $\frac{dn_c}{dz}$ is independent of z and

$$n_c(z) = n_c(0) + z \, \frac{dn_c}{dz} .$$

Since $n_c(L) << n_c(0)$ always (L is the length of the tube),

$$\frac{dn_c}{dz} \simeq - \frac{n_c(0)}{L} , \qquad (4)$$

n_c at z = 0 is given by the value of n_c at $T_c = 573°K$.

Let F be the fraction of the inside surface area A of the chamber that is covered with cesium when the cesium pressure in the chamber has reached an equilibrium value. $F(T_c)$ is independent of p_a. If V is the volume of the chamber, then the total number of cesium atoms that have to be transported from the reservoir is

$$\left(\frac{T_c}{T_g}\right) n_c(T_c) \quad V + \quad \frac{4 \cdot F \cdot A}{\pi \, d^2} \tag{5}$$

where d is the atomic diameter of the cesium atom.

Under these simplified conditions, the time t to reach equilibrium is

$$t \approx \frac{\left(\dfrac{T_c}{T_g}\right) \dfrac{n_c(T_c)V + 4 \cdot F(T_c) \cdot A}{\pi \, d^2}}{\dfrac{1}{3} \dfrac{\sigma}{n_a \, Q_d} \left[\dfrac{8kT_g(m_c + m_a)}{\pi \, m_c \, m_a}\right]^{1/2} \dfrac{n_c(573)}{L}} \; . \tag{6}$$

Diffusion times in the chamber are considered to be only small corrections to t.

C. Results

The following constants are used for evaluating t as a function of T_c and n_a for the particular experimental arrangements shown in Fig. 6.

k	=	1.38×10^{-16} erg $(°K)^{-1}$
m_a	=	6.68×10^{-23} g
m_c	=	2.22×10^{-22} g
T_g	=	$573°K$
$\left[\dfrac{8 \, k \, T_g(m_c + m_a)}{\pi \, m_c \, m_a}\right]^{1/2}$	=	6.25×10^4 cm sec^{-1}
V	=	44 cm^3
A	=	102 cm^2
σ	=	0.16 cm^2
Q_d (Massey and Burhop[2])	=	5.72×10^{-14} cm^2
d	=	5.34×10^{-8} cm
$n_c(573)$	=	2.8×10^{16} atoms cm^{-3}
L	=	7.5 cm

Substitution in Eq. (6) yields

$$t(\text{sec}) \approx N_a \left[.035 \; T_c \; N_c(T_c) + 2.09 \; F(T_c)\right] \tag{6a}$$

where N_a, N_c represent the number of argon, cesium atoms cm^{-3} in units of 10^{16}. No data have been found for the fractional coverage of glass by cesium as a function of temperature but data are available for the fractional coverage of tungsten as a function of temperature[3] for T ∼ 420 to 2000°K. These data were used to provide a measure of $F(T_c)$ for substitution in Eq.(6a). However, for much of the present study, the first term in Eq.(6a) is significantly larger than the second term (provided $F(T_c)$ for glass is of the same order of magnitude as $F(T_c)$ for tungsten) so that the value of $F(T_c)$ in this approximate calculation is unlikely to critically affect the value of t. Computations of t were made for the particular conditions under which the experimental values of t were measured, and both the experimental and calculated values of t, in hours, are shown in Table 1.

TABLE I

T_c °K	$N_c(T_c)$ (atoms cm^{-3} x 10^{16})	$F(T_c)$ (fractional coverage)	N_a (atoms cm^{-3} x 10^{16})	p_a (torr at 573°K)	t(exp) (Hours)	t(calc.) (Hours)
546	1.50	0.73	42.2	25	0.9	0.35
550	1.65	0.74	42.2	25	1.2	0.39
544	1.40	0.73	84.3	50	1.5	0.66
559	2.12	0.75	169	100	2.5	2.0
481	0.21	0.67	169	100	0.5	0.22
503	0.43	0.69	406	240	1.9	1.0
516	0.65	0.70	406	240	2.0	1.5

The agreement between the experimental and calculated values of t is considered to be satisfactory in view of the approximations made in the calculation and also because of the uncertainty in the experimental values of t due to the difficulty of accurately and quickly changing temperature. In most of the examples shown in Table I the ratio of cesium-argon ($N_c T_c/573 \; N_a$) is less than 10^{-3}. If this ratio is increased to the desired value by decreasing $N_c T_c$, then the value of t is correspondingly decreased.

13

It appears, therefore, that the present calculations can yield useful values of the times required to obtain an equilibrium cesium pressure in an ionization chamber due to diffusion of cesium vapor from a cesium reservoir, and that such times should be $\lesssim$ 2 hours (with the apparatus considered here) for a mixture of argon-cesium with Cs/Ar of 10^{-3} for argon pressures $\gtrsim$ 240 torr.

V. RESULTS OF ARGON-CESIUM TUBE 3

A. Tube Design

The cesium transport studies indicated that a relatively large diameter tubulation was required between the cesium reservoir and the ion chamber shown in Fig. 4. In order to ensure that the increased opening to the ion chamber (1/4 in. o.d. copper tubing) did not interfere with the measurements of the diode characteristic, a Kovar electrode was supported in the manner shown in Fig. 7 so that ion collection on a planar Kovar electrode could still be made. The spacing for this ion tube was set at 5 mm. By separating the ceramic rings with the Kovar ring shown in Fig. 7 sufficient area was provided so that cesium could be transported readily from the cesium reservoir to the volume between the uranium and Kovar electrodes.

The circuitry and heater were similar to those discussed in Sections II and III. However, for this tube considerable data were obtained without the need to use the nulling circuit since the leakage currents across the ceramics were much less than the measured ion currents.

B. Experimental Data

This ion tube operated satisfactorily in the reactor and the data obtained were reproducible once the cesium vapor equilibrium condition was reached. In order to determine the influence of the rather large area of the middle electrode, data were taken with the middle electrode connected to the uranium electrode and then to the Kovar electrode. These data indicated that when ion current is collected on a single electrode, either uranium or Kovar, the current is well behaved. That is, the current magnitude was as might be expected and under most conditions the current followed a $V^{1/2}$ relationship. There was a significant displacement of the zero current from the origin of the voltage scale however (0.5 volts with Kovar negative and uranium positive) which is not
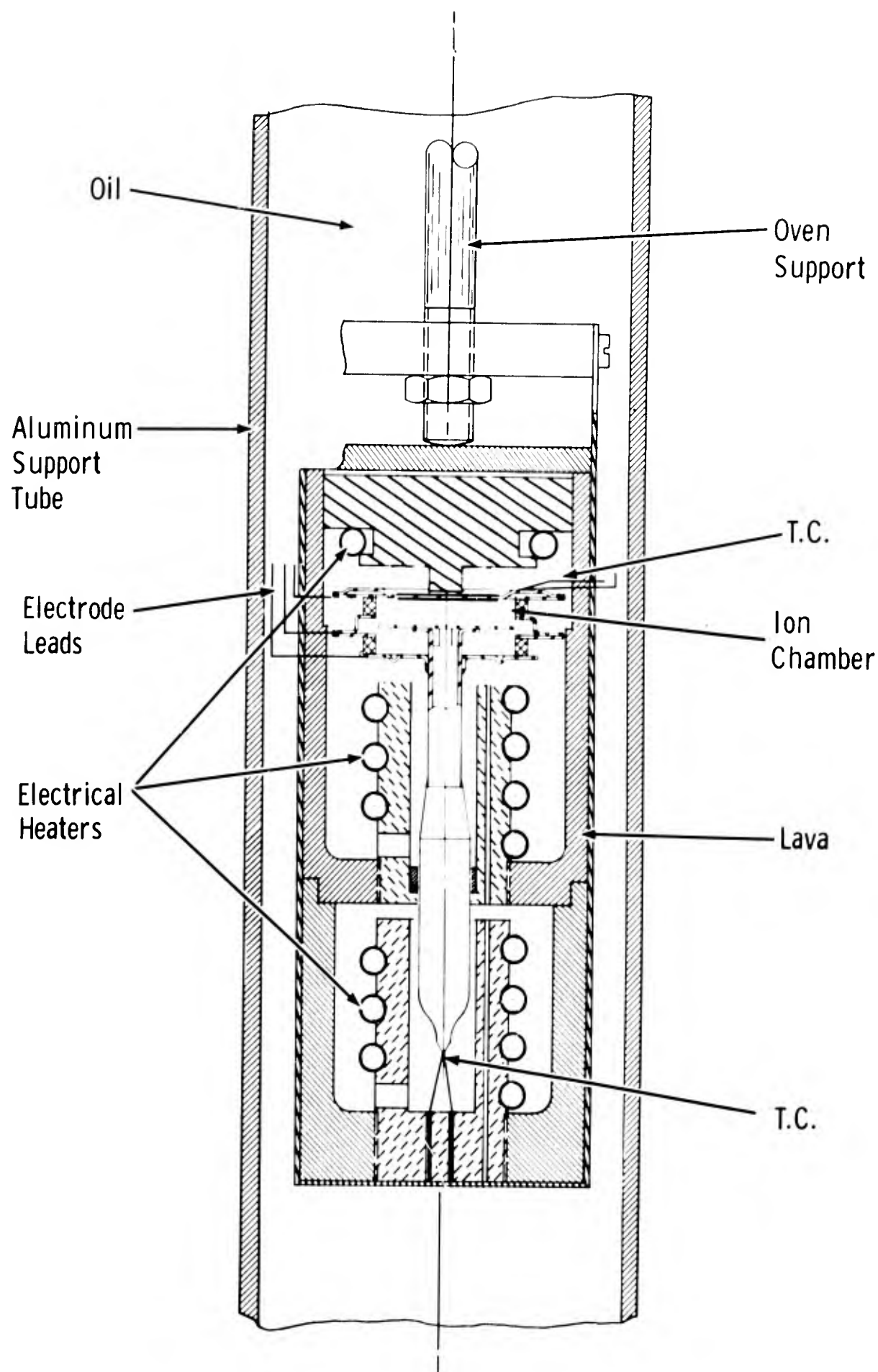
Fig. 7. Oven with ion tube configuration of tube 3.

completely understood. (The noble gas data always went through zero volts.) This may be associated with some small thermionic current which appeared to influence the ion current only when the tube was fully inserted into the core at 2 MW power level. In this case the I-V characteristic was very asymmetric— the uranium negative side of the characteristic showing 100 times more current than the other. Plotted on a logarithmic scale the characteristic is shown in Fig. 8.
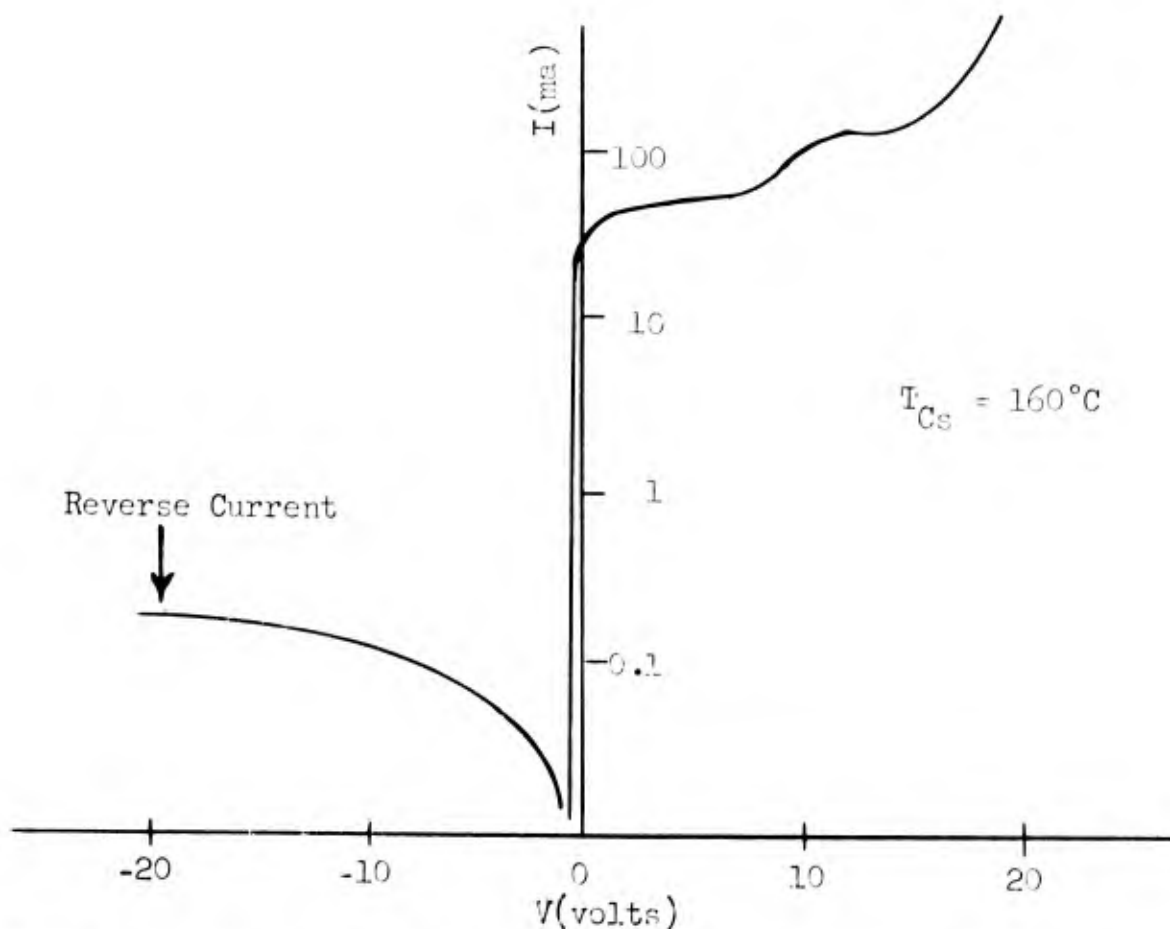
Fig. 8. I-V data for Ar-Cs Tube 3 fully inserted at 2 MW reactor power.

In order to make an estimate of surface conditions that could give rise to such electron currents, the following assumptions were made.

1. The slope of the retarding field curve could be used to obtain the uranium temperature;

2. The first current saturation at 25 ma corresponds to saturated emission, and

3. The knee of the curve gives the difference in work function between the uranium and Kovar surfaces.

From the slope, T_u=850°K which for a current of 25 ma corresponds to a surface of work function 1.7 ev. This implies that the cesium coating on the uranium

can provide such a low work function and also that a large temperature gradient exists between the point where the temperature was measured (the edge of the disc) to the uranium surface inside the tube. Such a possibility is not unreasonable. Now the collector work function (Kovar) can be determined from the absolute magnitude of the retarded current at a particular voltage; this gave a value of 1.8 ev — a number which appears to be reasonable for cesium on Kovar. The knee of the curve is roughly at 0.1 volts which corresponds well to the difference of the computed work functions for uranium and Kovar. Thus it appears that cesium coverage of the electrodes, along with a temperature higher than that expected on the uranium surface, can explain the current asymmetry attributed to thermionic emission from uranium.

In order to avoid this electron emission effect, the tube was operated at 10 inches above the core where the uranium was at a much lower temperature. The analysis of this well behaved data follows.

C. Fit of Theory to Experimental Data

Unlike the case for the neon-argon mixture a theoretical current-voltage curve could not be computed for the argon-cesium mixtures since $\bar{W}$, the energy to create an ion pair, has not been reported in the literature for this gas mixture. Instead a typical inpile experimental run was selected and a one parameter fit was made to the data by adjusting W in the code solution. The fit is shown in Fig. 9.

The inpile run selected for comparison was made with the reactor at 2 MW power but the ionization tube was withdrawn 10 inches from the midplane of the core. The cesium bath temperature was 150°C which for an argon pressure of 240 torr gave a cesium to argon ratio of $Cs/Ar = 2.8 \times 10^{-5}$. For this position the thermal neutron flux had been measured as 6.5×10^{12} cm^{-2} sec^{-1} with gold foil counting techniques. The experimental curve (Fig. 9) is similar in shape to the neon-argon I-V curves; that is the current follows a $V^{1/2}$ dependence on voltage out to about ± 25 volts and then the current increases rapidly with voltage again presumably due to electron impact ionization in the sheath. The code curve was adjusted to fit the experimental data in the negative quadrant (-25 volts $\leq$ V $\leq$ 0 volts), where the positive ion sheath is adjacent to the Kovar electrode. The fission fragment ranges for argon were used and the diode spacing was 0.504 cm. As in the case for the noble gas code runs (Section A) the
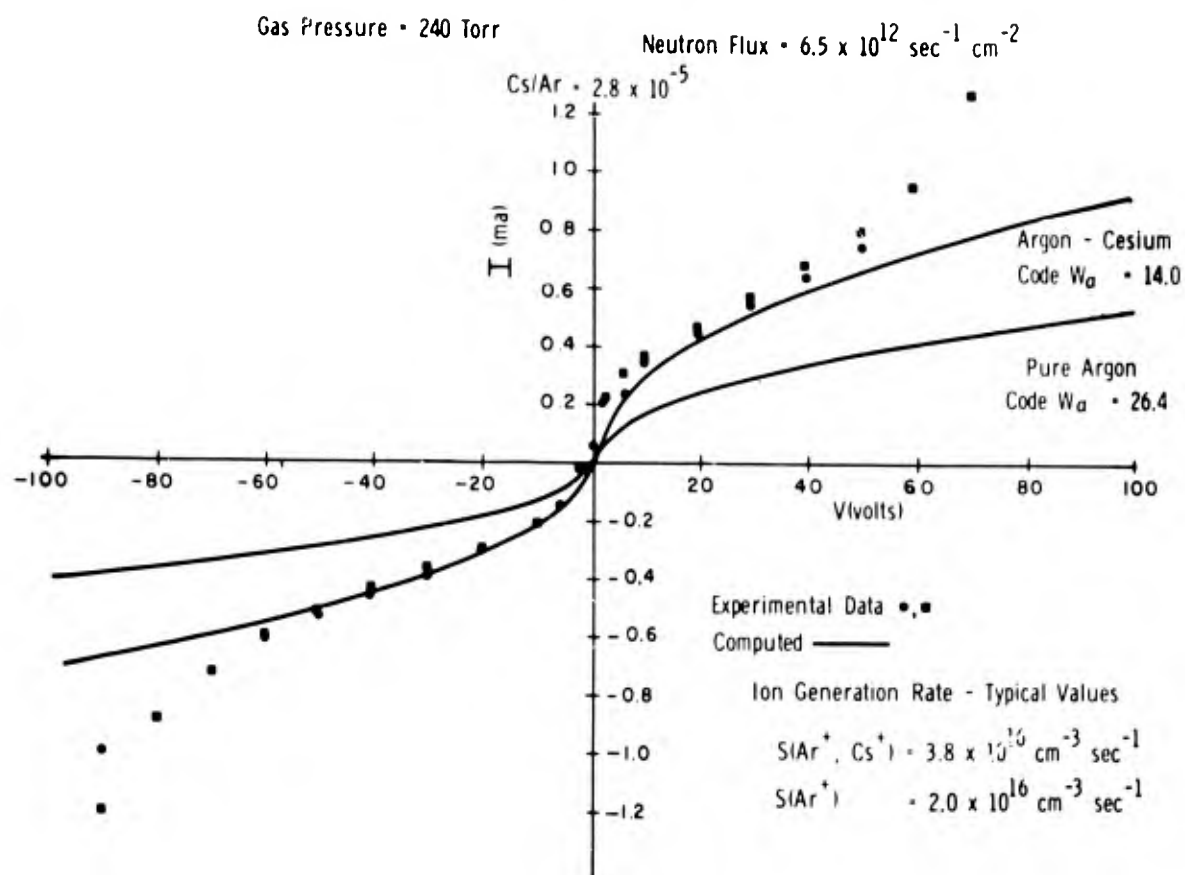
Fig. 9. I-V data for argon-cesium tube 3 compared to theory using W_α as an adjustable parameter.

ion collection area for V ⟨ 0 was taken as the total Kovar electrode area $(\pi\rho_2^2)$ while for V ⟩ 0 the ion collection area was taken as just the uranium area $(\pi\rho_1^2)$. The code curve gave the fit shown with a value of W_α=14.0 ev/ion pair or $\bar{W}_1$=14.84 and $\bar{W}_2$=15.54 ev/ion pair. Also shown for comparison is the theoretical curve for pure argon $(W_\alpha$=26.4 ev/ion pair$)$ for these same conditions.

It is seen that the current for Ar-Cs is greater than that for Ar alone which suggests a higher ion generation rate in this mixed gas system. This may arise from the additional ionization of cesium from the argon metastable states. On the other hand, Cs^+ ions may diffuse from the bulk of the plasma into the sheath(as discussed in Section A for the Ne-Ar data) and thereby give a current higher than that due to the total ions generated rate within the sheath. More detailed investigations are under way to resolve these unknowns.

REFERENCES

1. S. Chapman, Proc. Roy. Soc., A93, 1, 1917.

2. H.S.W. Massey and E.H.S. Burhop, Electronic and Ionic Impact Phenomena, 1951, (Oxford:Clarendon Press).

3. J. B. Taylor and Irving Langmuir, Phys. Rev. 44, 423, 1933.

18

SECTION F

BLANK PAGE

SECTION F

SECONDARY ELECTRON YIELD FROM FISSION FRAGMENTS*

ABSTRACT

The secondary electron yield from fission fragments has been measured directly using an ultra high vacuum diode containing uranium which was operated in a nuclear reactor. The current measured in this diode consisted of contributions from the positively charged fission fragments, secondary electron emission induced by fission fragments and photoelectrons generated by gamma radiation. The secondary electron yield, Δ, was determined from the secondary electron current and the computed fission fragment emission rate. For a thick ($\geqslant$ one range) uranium-nickel (5.7 wt % nickel) alloy the value of Δ is 207 $\pm$ 10.

Secondary Electron Yield

Measurements have been reported[1] on the secondary electron yield accompanying the emission of fission fragments from uranium dioxide films of thickness 0.1 to 3 microns. The average range for the light and heavy fragments in uranium dioxide is 10.6 and 8.2 microns, respectively. The electron yield decreased with increasing film thickness from about 570 to 300 electrons per fragment. This note discusses secondary electron yield for a film of a uranium metal alloy that was several times the fission fragment range in thickness and therefore equivalent to a yield for a film of one range thickness.

The secondary yield was measured with an ultra high vacuum (10^{-8} torr) ceramic-metal tube which consisted of three Kovar electrodes, each of 2.5 cm diameter, forming two diodes. This tube was developed primarily for inpile studies on the ionization of noble gases by fission fragments.[2] The uranium was brazed to one electrode in the form of a uranium-nickel alloy (5.7 wt % nickel) which was 15.5 microns thick and 1.9 cm in diameter. The interelectrode spacing in the diode containing uranium was 0.30 cm whereas the spacing in the diode without uranium was 0.33 cm.

The conventional current I measured in the uranium diode can consist of:

(1) Positively charged fission fragments, (I_f^+);

(2) Secondary electrons emitted from the uranium by fission fragments leaving the uranium electrode (I_1^-);

(3) Secondary electrons emitted from the Kovar by fission fragments arriving at the Kovar electrode (I_2^-);

(4) Electrons generated by gamma collisions (photo and Compton effects) within the tube walls, (I_γ^-); and

(5) Tertiary electrons generated by impact of electrons in processes 2, 3, 4.

The diode that did not contain uranium (gamma chamber) was used to study the magnitude of processes (4) and (5) at a gamma flux of 1.7×10^7 Rad hr^{-1}. Figure 1 shows the current-voltage characteristic obtained with this diode where the inserts represent the particle flows at large negative and positive voltages. The current is small, and the lack of saturation at high voltage indicates a broad electron energy distribution characteristic of gamma-produced electrons. The photoelectrons which are not completely retarded by a high retarding voltage are indicated in Fig. 1 by the dashed curves. The small inflection in the current near zero voltage suggests the presence of a few tertiary electrons (process 5) and the asymmetry in the curve suggests a difference in photoemission from the two surfaces. However, the purpose of using the gamma chamber was to estimate the gamma-induced contribution to the current measured with the uranium diode, and as indicated below, this gamma contribution is not significant.

Figure 2 shows the results for the diode chamber containing uranium. It may be seen that currents measured with this chamber at a neutron flux of 5.3×10^{12} sec^{-1} cm^{-2} are about two orders of magnitude larger than the currents measured simultaneously in the gamma chamber (Fig. 1). The gamma induced current will therefore be a small correction in the uranium chamber. At large positive potential (Fig. 2), we see that $I_1^- = I + I_f^+ - I_\gamma^-$. The secondary electron yield Δ per fission fragment for the uranium is given by I_1^-/eN_t, where N_t is the fission fragment particle emission rate. The current at large negative potential could be used to determine secondary electron yield per fission fragment for Kovar; however, for that case a correction would have to be made for the energy and angular distribution of the fission fragments that bombard that electrode. Note that tertiary electrons are always suppressed at large potentials.

2

In addition the saturation characteristic of Fig. 2 indicates that the secondary electrons generated by fission fragments have an energy distribution lying almost entirely below 20 ev; thus tertiaries will be few in any event.

The current I_f^+ from fission fragments is computed from

$$I_f^+ = A\phi \; \Sigma_f \; e(Z_1 R_1 + Z_2 R_2)/8 \tag{1}$$

where A, ϕ, Σ_f represent respectively the uranium area, the neutron flux, and the macroscopic fission cross section; $eZ_{1,2}$ and $R_{1,2}$ are the initial charge and range of each fragment. We obtain $I_f^+ = 1.7 \times 10^{-7}$ amp for the data of Fig. 2, about 5% of the measured saturation current.

The fission fragment emission rate was computed from $N_t = A\phi \; \Sigma_f (R_1 + R_2)/4$ which is derived in the Appendix along with Eq. 1. The value of current obtained at 50 volts is used to calculate the secondary electron emission coefficient. Table 1 lists the values computed for two different flux levels.

TABLE 1. Secondary Electron Yield per Fission Fragment, Δ
(Electrons/Fission Fragment)

Neutron Flux $(\sec^{-1} cm^{-2})$	Uranium Electrode, Δ
5.3×10^{11}	212 ± 10
5.3×10^{12}	202 ± 10

Anno[1] has indicated an extrapolated value for Δ about 100 for a one range film of UO_2. His measurements extended from 0.7% to 28% of the fission fragment range in UO_2.

There is considerable similarity in the energy distributions of electrons emitted from the uranium and Kovar surfaces, because the current-voltage characteristic is symmetric about the current at zero voltage. It can be readily checked that space charge effects are negligible for the experimental conditions reported here.

APPENDIX

The fission fragment emission rate N is computed assuming the fragments are generated uniformly and are emitted isotropically at the point of generation. The fragments born within an increment dy at a depth y below the uranium surface, and moving at an angle θ with respect to the normal, will

3

contribute to the emission when $\theta \leq \theta_{max} = \cos^{-1}(y/R)$ and $y \leq R$ (one range thickness).

$$\therefore N = A \phi \Sigma_f \int_0^R \int_0^{\theta_{max}} (1/2) \sin \theta \, d\theta \, dy \qquad (2)$$

This yields $N = A \phi \Sigma_f R/4$. Since two groups of fragments are generated per fission, the total fission fragment emission rate is $N_t = A \phi \Sigma_f (R_1 + R_2)/4$.

The fission fragment current I^+ from the uranium surface is obtained by including in Eq. (2) an expression which takes into account the linear loss of fragment charge with distance.[3] The electronic charge on a fragment escaping from the uranium surface at angle θ from depth y is $Z(1 - y/R \cos \theta)$ where Z is the initial electronic charge of the fragment. Thus,

$$I^+ = A \phi \Sigma_f e Z \int_0^R \int_0^{\theta_{max}} (1 - y/R \cos \theta)(1/2) \sin \theta \, d\theta \, dy, \qquad (3)$$

which yields $I^+ = A \phi \Sigma_f e Z R/8$. For the two groups of fragments, the total fission fragment current I_f^+ is that given in Eq. (1) of the text.

ACKNOWLEDGMENT

We gratefully acknowledge the helpful suggestions of Professor David J. Rose during these investigations.

REFERENCES

1. J. N. Anno, J. Appl. Phys. 33, 1678 (1962).
2. C. B. Leffert, D. B. Rees, and F. E. Jamerson, J. Appl. Phys., to be published. (See Section A.)
3. H. A. Bethe and J. Ashkin, Experimental Nuclear Physics, edited by E. Segrè (John Wiley and Sons, Inc., New York, 1953), Vol. 1, pp. 228-230.
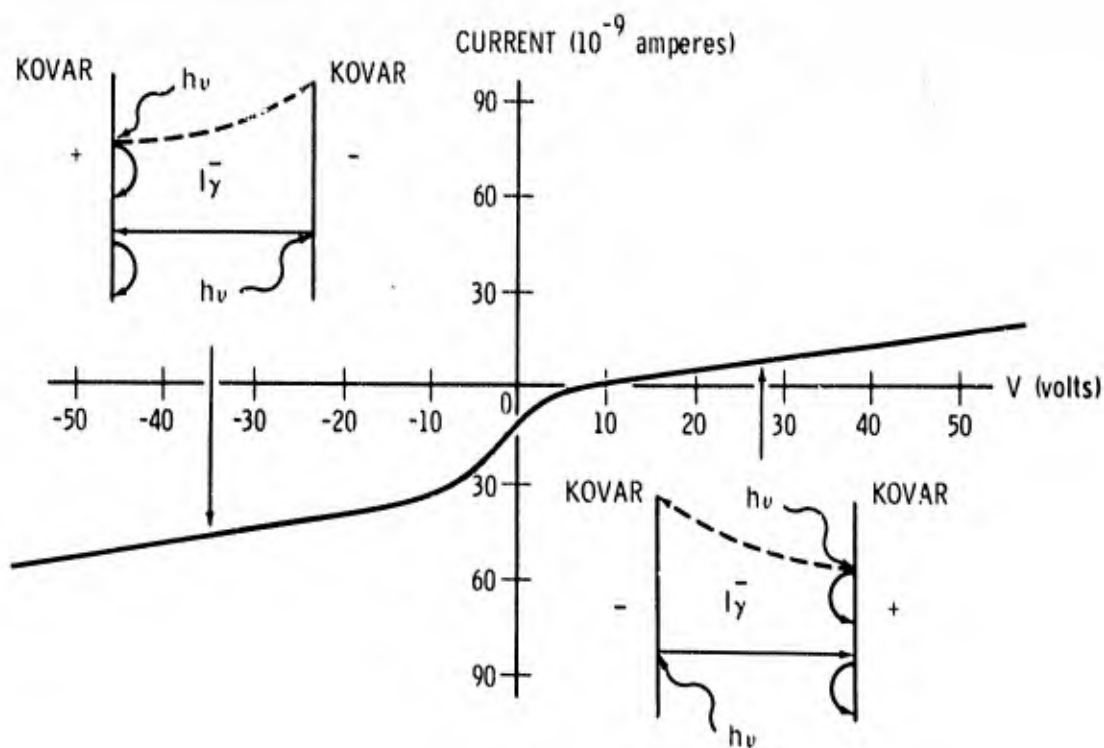
Fig. 1. Experimental current-voltage characteristic for the gamma chamber. The inserts show the electron flows for large negative and positive potentials.
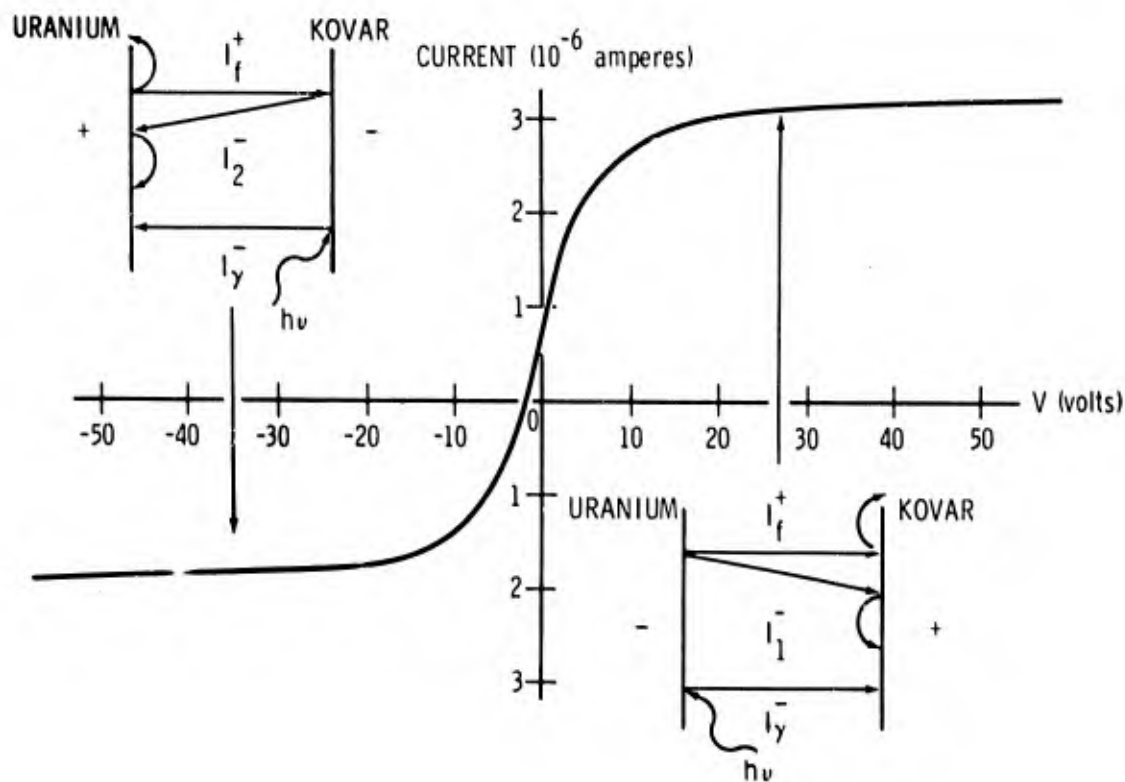
Fig. 2. Experimental current-voltage characteristic for the uranium chamber. The inserts show the particle flows for large negative and positive potentials.

PUBLICATIONS

1. F. E. Jamerson, "Noble Gas Plasmas and Emitter Materials for
    Nuclear Thermionic Converters", Proceedings of Symposium on High
    Temperature Conversion — Heat to Electricity, University of Arizona,
    TID - 7687, February 19 - 21, 1964.

2. C. B. Leffert, D. B. Rees, and F. E. Jamerson, "Fission Fragment
    Ionization of Mixed Gases", Proceedings of the IEEE Thermionic
    Converter Specialists Conference at Cleveland, Ohio, October 26 -
    28, 1964.

DISTRIBUTION

No. Copies

Office of Naval Research
Power Branch (Code 429)
Department of the Navy
Washington, D. C.   20360

4

ONR Branch Office
Chicago, Illinois
    Attn. M. A. Chaszeyka

1

U. S. Naval Research Laboratory
Technical Information Division
Washington, D. C.   20390

6

Commanding Officer
Office of Naval Research Branch Office
Box 39 Navy No. 100 Fleet Post Office
New York, New York

1

Director of Special Projects (SP-001)
Department of the Navy
Washington, D. C.   20360

3

Chief, Bureau of Ships
Department of the Navy
Washington, D. C.   20360
    Attn: Code 342B
           Code 1500 Mr. L. Schlanger
           Code 456B, Mr. V. Gardner
           Code 210L
           Code 660 Dr. J. B. Frihauf

2
1
1
2
1

Bureau of Naval Weapons
Department of the Navy
Washington, D. C.   20360
    Attn: Library

1

Defense Documentation Center for
  Scientific and Technical Information
Cameron Station, Building 5
5010 Duke Street
Alexandria, Virginia   22314

20

Commandant, U. S. Marine Corps
Code CSY-3
Headquarters, Marine Corps
Washington, D. C.   20380

1

National Aeronautics and Space Administration
1520 H Street, N.W.
Washington, D. C.   20546
    Attn: James J. Lynch
           W. Scott

1
1

National Aeronautics and Space Administration
Lewis Research Center
21000 Brookpark Road
Cleveland 35, Ohio
    Attn: H. Shwartz   1
               Roland Breitwieser   1
               Bernard Lubarsky   1
               Wm. LeGray   1
               R. P. Migra   1

Jet Propulsion Laboratory   1
California Institute of Technology
4800 Oak Grove Drive
Pasadena, California
    Attn: P. Rouklove

U. S. Atomic Energy Commission
Division of Reactor Development
Washington, D. C.   20545
    Attn: SNAP Reactor Branch   1
               Direct Conversion Branch   1
               Army Reactor, Water Systems Branch   1
               Isotopic Power Branch   1

U. S. Atomic Energy Commission   1
San Francisco Operation Office
2111 Bancroft Way
Berkeley 4, California
    Attn: Reactor Division

Los Alamos Scientific Laboratory   1
P. O. Box 1664
Los Alamos, New Mexico
    Attn: Dr. George M. Grover

Aeronautical Systems Division   1
ASRMFP-2
Wright Patterson Air Force Base
Ohio

Air Force Cambridge Research Center   1
(CRZAP)
L. G. Hanscom Field
Bedford, Massachusetts

U. S. Army Signal R and D Laboratory   1
Fort Monmouth, New Jersey
    Attn: Dr. Emil Kittl

State University of New York   1
College at Fredonia
Physics Department
Fredonia, New York   14063
    Attn: Dr. John J. Connelly, Jr.

General Motors Corporation   1
Allison Division
Indianapolis 6, Indiana
    Attn: D. L. Dresser

Research Laboratories Library   1
General Motors Corporation
General Motors Technical Center
P. O. Box 388
Warren, Michigan
    Attn: Dr. F. Jamerson

Atomics International   1
P. O. Box 309
Canoga Park, California
    Attn: Dr. R. C. Allen

General Atomics   1
P. O. Box 608
San Diego 12, California
    Attn: Dr. W. Pidd

Ford Instrument Company   1
3110 Thomson Avenue
Long Island City, New York
    Attn: T. Jarvis

Illinois Institute of Technology Research Institute   1
10 West 35th Street
Chicago 15, Illinois
    Attn: Dr. D. W. Levinson

RCA Laboratories   1
David Sarnoff Research Center
Princeton, New Jersey
    Attn: Dr. Paul Rappaport

The Martin Corporation   1
Baltimore 3, Maryland
    Attn: Dr. W. J. Levedahl

Thermo Electron Engineering Corporation   1
85 First Avenue
Waltham 54, Massachusetts
    Attn: Dr. George Hatsopoulos

The Marquardt Corporation   1
ASTRO Division
16555 Saticoy Street
Van Nuys, California
    Attn: C. Kaplan

Texas Instruments, Incorporated   1
P. O. Box 5474
Dallas 22, Texas
    Attn: Dr. R. A. Chapman

Radio Corporation of America   1
Electron Tube Division
Lancaster, Pennsylvania
    Attn: F. G. Block

General Electric Research Laboratory   1
Schenectady, New York
    Attn: Dr. V. C. Wilson

Babcock and Wilcox Company   1
1201 Kemper Street
Lynchburg, Virginia

Knolls Atomic Power Laboratory   1
Schenectady, New York
    Attn: Dr. R. Ehrlick

Institute for Defense Analysis   1
1666 Connecticut Avenue, N. W.
Washington, D. C.
    Attn: Mr. Robert Hamilton

Thomson Ramo Wooldridge, Incorporated   1
7209 Platt Avenue
Cleveland 4, Ohio
    Attn: Wm. J. Leovic

General Electric Company   1
Valley Forge Space Technology Center
P. O. Box 8555
Philadelphia 1, Pennsylvania
    Attn: R. M. Cohen

General Electric Company   1
P. O. Box 846
Atomic Product Division
Vallecitos Laboratory
Pleasenton, California
    Attn: C. H. Seaton

General Electric Company   1
Power Tube Division
1 River Road
Schenectady 5, New York
    Attn: Mr. D. L. Schaefer

Power Information Center   1
University of Pennsylvania
Moore School Building
200 South 33rd Street
Philadelphia 4, Pennsylvania

General Motors Research Laboratories
12 Mile and Mound Roads, Warren, Michigan

INVESTIGATIONS ON THE DIRECT CONVERSION OF NUCLEAR
FISSION ENERGY TO ELECTRICAL ENERGY IN A PLASMA
DIODE, by C. B. Leffert, D. B. Rees and F.E.Jamerson

113 pp. incl. figs.

Annual Technical Summary Report, November 1, 1953
to October 31, 1954 (Report No. 5)

Contract Nonr-3109(00)

The ionization of pure, mixed and cesium-seeded
noble gas systems by fission fragments has been inves-
tigated using ceramic-metal tubes operated in a high
neutron flux region of a nuclear reactor. An analysis
of the production and transport of ions and electrons
in the tube has shown that when the charge loss in the
plasma is predominantly by volume recombination of
molecular ion and electron, the tube current is pro-
portional to (voltage)1/2. Experimental current-
voltage data in neon, argon, xenon and a neon-argon
mixture with Ar/He of 10-3 for gas pressures of 240
and 400 torr and a neutron flux ~ 10^13 cm^-2sec^-1

1. Direct energy conversion
2. Thermionics
3. Gaseous electronics
4. Plasma physics
I. C. B. Leffert
II. D. B. Rees
III. F. E. Jamerson
IV. General Motors Corporation
Research Laboratories
V. Nonr-3109(00)

UNCLASSIFIED